博士論文

論文題目　Experimental and Numerical Investigation of Thermal Stratification by Direct Contact Condensation of Steam in Pressure Suppression Pool
（圧力抑制室における直接接触凝縮に起因する温度成層化現象に関する研究）

氏　　名　　宋　大憲

Experimental and Numerical Investigation of Thermal Stratification by Direct Contact Condensation of Steam in Pressure Suppression Pool

（圧力抑制室における直接接触凝縮に起因する
温度成層化現象に関する研究）

宋 大憲

Human and Engineered Environmental Studies
Graduate School of Frontier Sciences
The University of Tokyo

February 2014

ACKNOWLEDGEMENTS

First and foremost I would like to express deepest gratitude to my supervisor Prof. Koji Okamoto. It has been an honor to be his Ph.D. student. He has taught me, both consciously and unconsciously, how a research should be based physically. I appreciate all his contributions of time, ideas, and funding to make my Ph.D. experience productive and stimulating. I am also thankful for the excellent example he has provided as a successful engineer and professor. His wide activity and various interests in research and society has been motivational for me even since I was in master course in Korea.

I am honorable to study at the Visualization Laboratory, Department of Human and Engineered Environmental Studies, Graduate School of Frontier Sciences of the University of Tokyo in Japan. I would like to express my deep gratitude to all those people who give me the supports and contributions to this thesis. I would like to thank Asst. Prof. Nejdet Erkan and Dr. Byeongnam Jo especially. Asst. Prof. Erkan gave me good advices and research inspiration and helped me to proceed my experiments. My Ph. D would have not finished without him. Dr. Jo shared his experience and good discussion, and taught me various technical points in research.

I would also like to thank Prof. Kyung Chun Kim of Pusan National University for introducing me to Prof. Okamoto and his good advises when I start studying in Japan.

I would like to give thanks to all my friends in Japan and Korea. They helped me to enjoy the life in Japan and have wonderful times and exciting experiences. I could get back on my feet from my tough period by their favor as well.

Lastly, I would like to thank my family for all their love and encouragement. For my parents who raised me with a love of study and supported me in all my pursuits. For my brother and his wife who have deep trust and concern. For my nephew who makes me smile. Thank you.

TABLE OF CONTENTS

LIST OF FIGURES

LIST OF TABLES

NOMENCLATURE

α	thermal diffusivity	[m^2/s]
β	thermal expansion	[1/K]
δ	bubble amplitude	[mm]
f	bubble frequency	[Hz]
h	heat transfer coefficient	[W/m^2K]
h_{fg}	latent heat	[kJ/kg]
H	height of SP water	[m]
H_m	height of mixing area	[m]
j_m	steam mass flux	[kg/m^2s]
k_s	thermal conductivity of Stainless steel	[W/m·K]
k_a	thermal conductivity of air	[W/m·K]
L	distance between steam injection pipe tip and SP bottom	[m]
m	mass	[kg]
m_m	mass of mixing area	[kg]
$\dot{m}$	steam mass flow rate	[kg/s]
v	kinetic viscosity	[m^2/s]
$\dot{p}$	momentum rate	[$kg·m/s^2$]
q	heat input	[W]
T_f	film temperature	[K]
T_{st}	steam temperature	[K]
T_{sat}	saturation temperature	[K]
ΔT_{sub}	subcooling	[K]
U_{ex}	experimental overall heat transfer coefficient	[W/m^2K]
U_{th}	theoretical overall heat transfer coefficient	[W/m^2K]

C_{DCC}	Constant for numerical simulation of DCC
Gr_L	Grashof number
MI	Mixing Interface number
Nu_L	Nusselt number
Pr	Prandtl number
Pr	Prandtl number
$PSCR$	Pressure Suppression Capacity Ratio
Ra_L	Rayleigh number

Ri	Richardson number
Ri_{DCC}	Richardson number for Direct Contact Condensation

CHAPTER 1 INTRODUCTION AND OBJECTIVES

1.1 Introduction

Fukushima-Daiichi accident is one of the design based accidents with extreme natural event, an exceptional strong earthquake accompanied by a colossal tsunami. Long duration station black out (SBO) happened by damaged AC elect*ric* power and got flooded emergency diesel engines. Although the reactors were cooled by Reactor Core Isolation Cooling System (RCIC) after reactor isolation in unit 2 and 3, RCIC malfunctioned by unconfirmed reasons, the reactor vessel water level decreased, fuel rods were damaged, and those situations leaded to severe accidents such as hydrogen explosion and radioactive matter release. With RCIC malfunction, the pressure in suppression pool (SP) increased higher than expected. In this research, the reason of abnormal pressure increase in SP is investigated in the viewpoint of thermal stratification phenomenon.

Thermal stratification is horizontal layers of differing temperature at different depths by different densities. When it happens inside SP, it would reduce pressure suppression capacity of the SP. There are two areas; mixing area and non-mixing area. Those are classified by temperature-changed area and unchanged area. The coolant of non-mixing area is not used for cooling of the system. There is mixing interface between mixing and non-mixing area. The mixing interface would decide the pressure suppression capacity of one SP.

There are various studies about thermal stratification and mixing phenomenon by Direct Contact Condensation (DCC) in water pool experimentally and analytically. However, there is no research to try to find the relationship between thermal stratification and DCC considering DCC regimes and momentum. To estimate the cooling capacity of SP, CFD code for thermal stratification should be developed and validated, and analytical methods should be investigated.

This research is to find out the effects of thermal stratification to SP and the mechanisms and to develop tools to detect thermal stratification. To investigate the mechanism of thermal stratification, downsized 2D SP model was designed and time resolved temperature and pressure data were acquired with thermocouples and pressure transducers. The steam bubble frequency and amplitude were obtained from the visualization by high-speed camera. The mixing area decided from natural convection by buoyancy force of condensate was studied and

quantified by PIV (Particle Image Velocimetry). Numerical simulation was carried out with ANSYS CFX 14.0 in single phase and validated with experimental data. The thermal stratification criteria was obtained by non-dimensional studies.

1.2 Fukushima-Daiichi Accident and Thermal Stratification

1.2.1 Fukushima-Daiichi Accident

The Fukushima accidents are the most recent significant accidents of light water reactors (LWRs). It occurred on March 11, 2011. Firstly, earthquake occurred being measured 9.0 on the Richter scale. It involved the movement of part of the tectonic plate and generated a colossal tsunami killing around 26,000 people. After earthquake, the plants shut down automatically and there was no visible structural damage. However, the AC electric power lines were damaged and the plant lost its off-site power supply. Tsunami followed one hour after the earthquake and damaged almost all the electric power supplies including the diesel generators which were operating and supplying power to the plant after the earthquake. This made long duration station black out (SBO) accidents.

Without power, all instrumentation and safety systems were not operable. The electricity from batteries was used for illumination and some essential safety-related valves and pumps for 4 to 8 hours. Reactor was cooled by isolation condenser (IC) and reactor core isolation cooling System (RCIC) but those became malfunctioned. The reactor vessels which lost heat sink lost coolant and the fuel rods damaged. The reactor vessel pressure increased abnormally and it damaged reactor vessel. Zirconium and other metallic materials were oxidized with water on the hot temperature. It produced hydrogen gas and hydrogen explosion occurred inside containments [1, 2].

1.2.2 Fukushima-Daiichi Unit 2 and 3 Accident Overview

Following is the Fukushima-Daiichi Unit 2 accident overview. At 14:47 on March 11, 2011, reactor scram signal transmitted due to earthquake. Reactor automatically shut down and MSIV

(Main Steam Isolation Valve) was closed because off-site power source was lost by earthquake. RCIC was manually started up and automatically shut down due to water level increas. Tsunami arrived at 15:27 and 15:35 and RCIC was manually started up. Station black-out (SBO) happened and it is determined to be an event corresponding to Article 10 of the Nuclear Disaster Act (SBO). SBO causes loss of functions for removing residual heat from CV(Containment Vessel) and it is determined to be an event corresponding to Article 15 of the Nuclear Disaster Act (the loss of ECCS injection sources). RCIC malfunctioned and reactor water level dropped. Operation commenced to depressurize the RV (Rector Vessel) using SRV (Safety Relief Valve) and seawater injection commenced using fire engine. However, the pressure of RV increased and CV pressure increased. Finally, a large explosive sound and vibration occurred.

Unit 3 accident is quite similar to the one of unit 2 except that at unit 3 HPCI (high pressure coolant injection system) was used for around 2 hours after RCIC shut down.

1.2.3 Pressure Suppression Pool and RCIC

Pressure suppression systems in BWRs are utilized to control the pressure and temperature of containment in accident or abnormal operating conditions in which reactor pressure is needed to be relieved in a short time. There are interconnecting vent networks, having additional downcomer vents as pressure relieve system, between the drywell and the wetwell, SP. This pressure relieve system operates with directing the steam produced in pressure vessel of the reactor into SP through a vent line whose open-end submerged into the water. Steam condenses with direct contact condensation mechanism in the SP.

Fukushima Daiichi units 1, 2, 3, 4 and 5 are the type of BWR 3 and 4 designed by General Electric Co. Those reactors have Mark I containment which consists of a drywell housing the reactor pressure vessel (RPV) and associated equipment, and a toroidal-shaped SP as shown in Fig.1.1. Safety relieve valves (SRVs) and RCIC system connect RPV and SP. In units 2 and 3, downcomer vent lines from SRV and one RCIC vent line are submerged into water in SP. When RPV pressure increase, the SRVs open and steam is relieved to SP and when reactor is isolated from main steam isolation line, RCIC system works to condensate the steam from RPV inside SP and injects water into RPV.

Fukushima nuclear power plant unit 2 and 3 (BWR 4) have RCIC, which injects water into RPV during isolation event, as safety system. After reactor isolation, it sends reactor steam to RCIC turbine, which drives the pump to inject water into RPV. Condensed steam from RCIC turbine is discharged to SP. The injected water to RPV is from condensate storage tank (CST) primarily but when the SP water level gets high, the water source switches to SP.

However, only one RCIC steam discharge pipe is connected to the SP. Steam from RPV condenses and relieves heat in localized area. Localized heat injection in very large SP cannot generate large advection force to mix the water inside SP. Thermal stratification may happen and be the potential problem for the failure of SP.

1.2.4 The Effects by Thermal Stratification

Although thermal stratification is usefully used in some sensible heat storage systems, it could cause heat sink malfunction due to the extra increase of temperature and pressure. The interface between mixing and non-mixing area is decided by the heat source geometrical position and the amount of momentum and it decides the cooling capacity of the cooling system. Not only the cooling capacity decreases by thermal stratification, but also the pressure suppression capacity decreases. The reason is that the temperature of the gaseous area increases and the pressure increases since the temperature of the top area of the liquid increases by thermal stratification. If thermal stratification happens inside a cooling system or a pressure suppression system, the capability to cool down the system and suppress the pressure would be significantly lower.

Since thermal stratification is highly sensitive to momentum and geometry, it is difficult to investigate theoretically. Because the momentum is from condensation interface, the momentum according to the DCC regime should be studied. The variation of cooling capacity and pressure suppression capacity by thermal stratification should be investigated. The effects by thermal stratification should be quantified and applied to the design of nuclear power plant and the simulation of severe accidents.

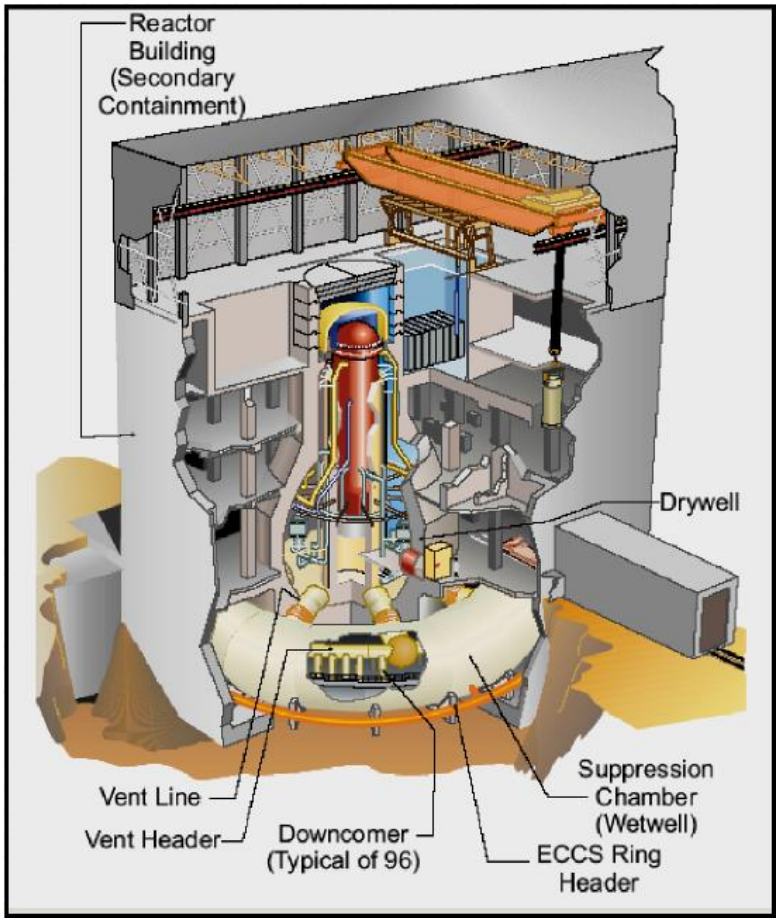

Fig.1.1 The schematic of Mark I containment (BWR3&BWR4),
Sourced by U.S.NRC

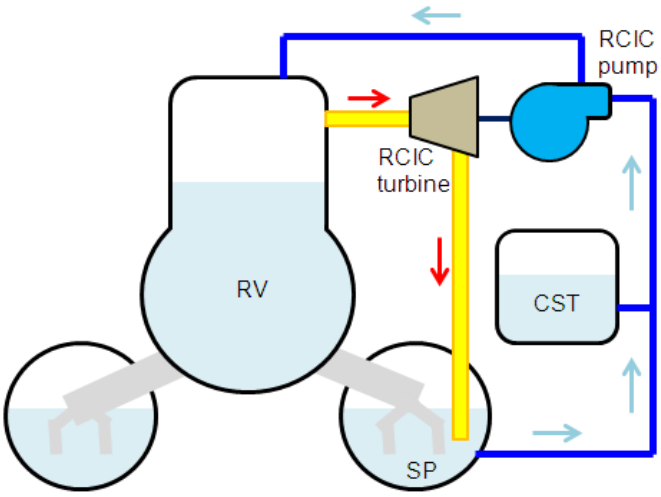

Fig.1.2 The schematic of RCIC system

1.3 Former and Related Researches

1.3.1 Direct Contact Condensation

The phenomena of Direct Contact Condensation (DCC) are well known by various experimental and theoretical studies. It is easy way to suppress the pressure of the two-phase flow systems but the phenomenon is not simple.

1.3.1.1 Direct Contact Condensation Regime Map

It is important in thermal stratification formation which regime of DCC is represented since the different regime demonstrates different momentum near interface and hot water layer.

Chan et al. (1982) shows a regime map for DCC with the two coordinates of steam mass flux, which characterizes the driving mechanism, and pool temperature at atmospheric condition, which characterizes the condensation rate, as shown in Fig.1.3 [3]. The steam injection pipe diameter is 51 mm and pool pressure is atmospheric. These regimes were divided by the location of steam region and the location which steam bubbles detach from the source. The oscillating frequency was added to the regime map.

Condensation would happen until there is still subcooling, which is the temperature difference between saturation temperature and surrounding water temperature. As shown in Fig.1.3, when subcooling is getting smaller than critical point, condensation does not happen and the steam bubble escapes. It means the SP loses its pressure suppression capacity.

When the steam jet is at sonic speed, it has a stable cone shape. However, at subsonic, the steam jet gets unstable and this unstable oscillatory cone jet persists until the steam mass flux is less than 50 kg/m2s. As the steam mass flux gets lower, the steam region shows oscillatory bubble. At even lower mass flux, the bubbles show chugging motion and finally oscillatory interface. When the pool temperature is low, and therefore the subcooling is large, the steam region normally exists below the pipe exit with the shape of a cone or a bubble but when the subcooling is small, the steam region tends to encapsulate the pipe exit. Fig.1.4 shows the steam region according to the DCC regime.

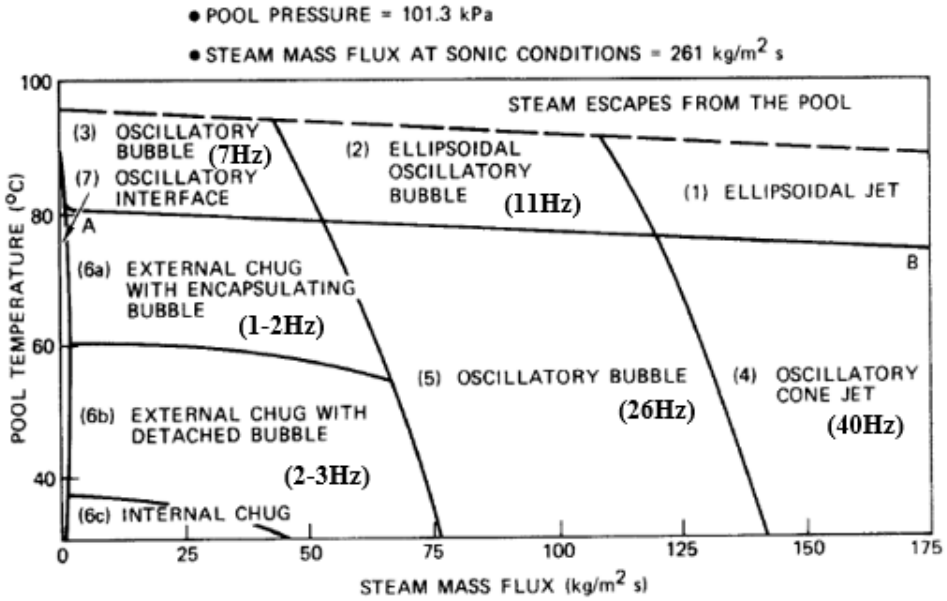

Fig.1.3 Condensation regime map [3]

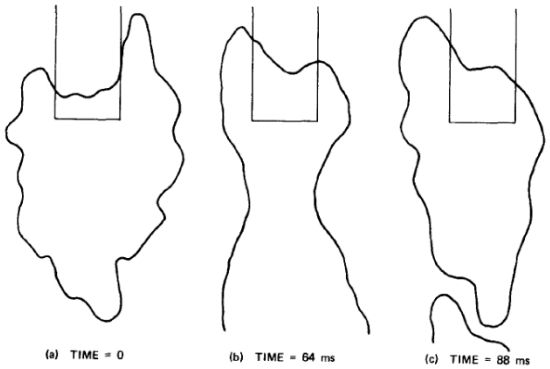

(a) Ellipsoidal oscillatory bubble, regime 2

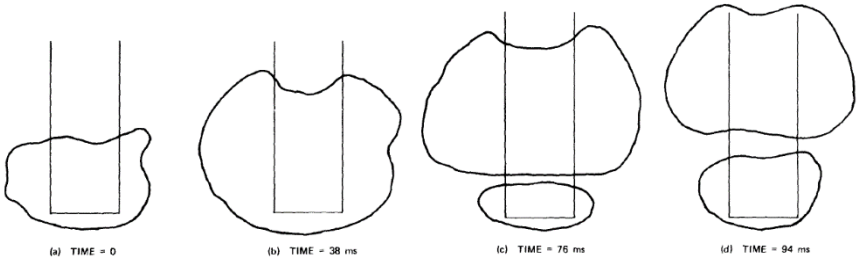

(b) Oscillatory bubble, regime 3

(Continued)

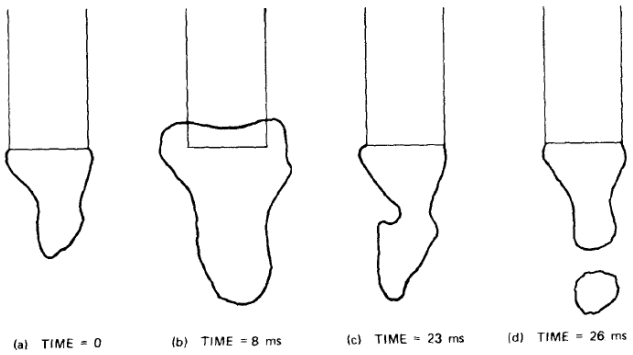

(c) Oscillatory cone jet, regime 4

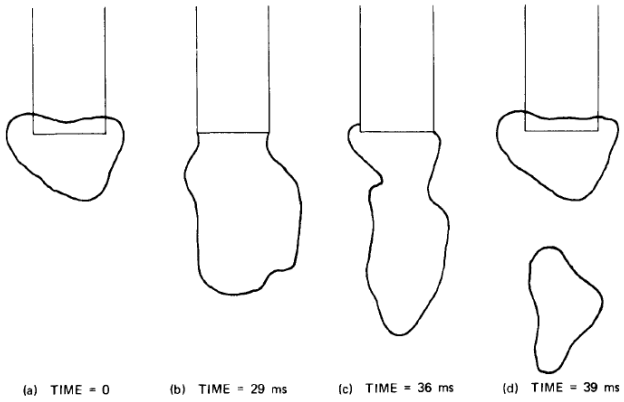

(d) Oscillatory bubble, regime 5

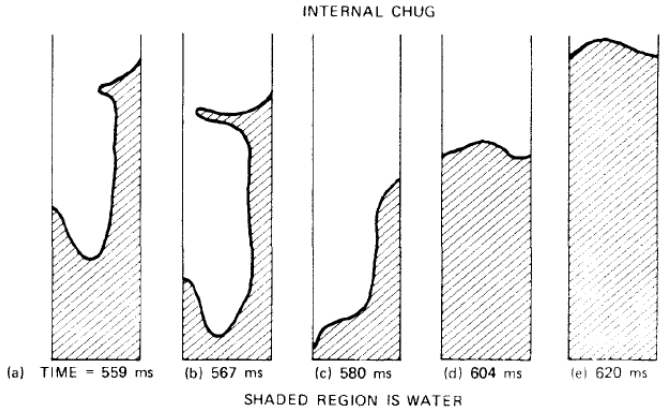

(e) Internal chug, regime 6c

(Continued)

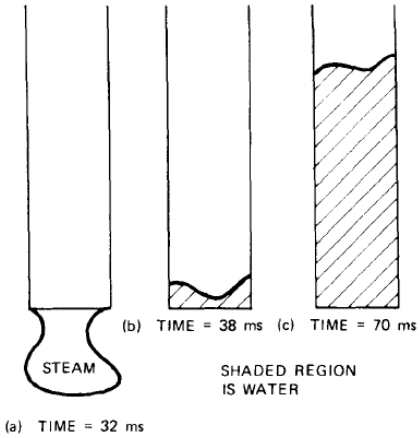

(f) External chug with detached bubble, regime 6b

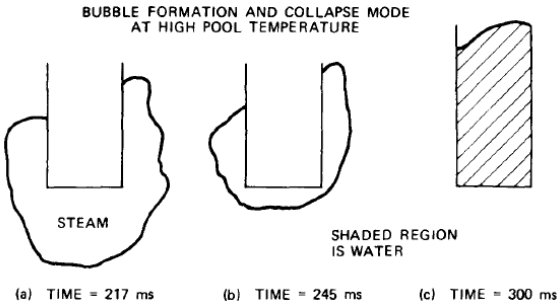

(g) External chug with encapsulating bubble, regime 6a

Fig.1.4 Steam region according to DCC regime [3]

Aya et al. (1987) classified oscillation phenomena by direct condensation into four regimes for steam mass flux regions of less than 40 kg/m2s: (1) internal chugging (including large chuggine), (2) small chugging, (3) condensation oscillation, and (4) bubbling [4]. They focused on theoretical discussions on the boundaries between regimes based on the mechanism of each oscillation regime. Fig.1.5 shows typical pressure oscillation in vent tube at each regime and fig.1.6 is the regime map by the authors. From fig.1.5 and fig.1.6, it is assumed that the regions whose subcooling is larger than 20K (chugging and condensation oscillation regime) have much more momentum than the regions whose subcooling is smaller than 20K (bubbling regime).

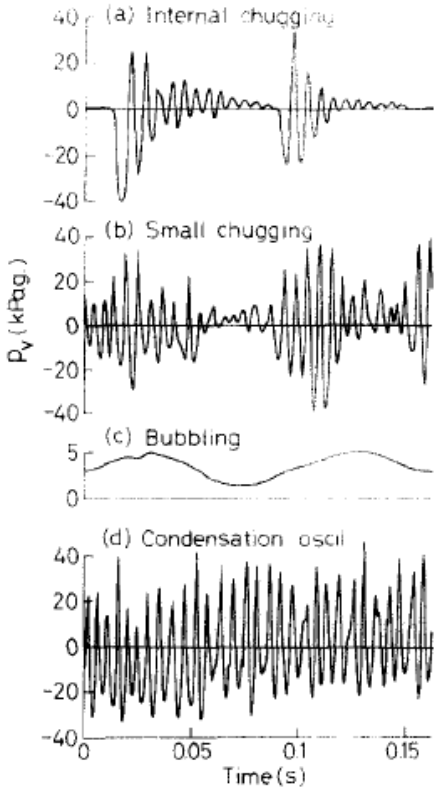

Fig.1.5 Typical pressure oscillation in vent tube at each regime [4]

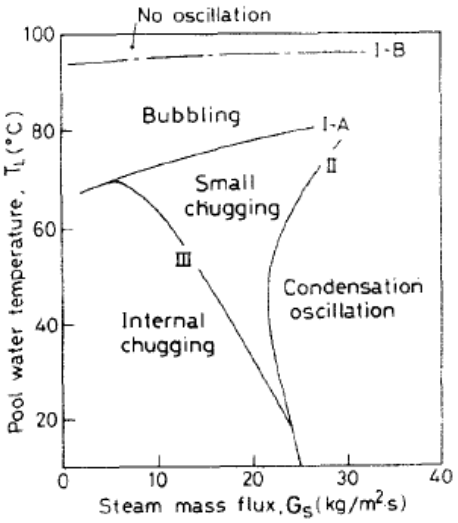

Fig.1.6 Condensation regime map [4]

The mass conservation and momentum equations were linearized as the equation (1-1). The characteristic equation of third-order linear differential equation is expressed as the equation (1-2). For the boundary of bubbling high-frequency oscillation, the equation (1-3) was proposed using spherical bubble model and the equation (1-4) was introduced using cylindrical bubble model. For the boundary of bubbling low-frequency oscillation, the equation (1-5) was proposed. The equation (1-6) represents the boundary between chugging and condensation oscillation. The boundary of internal chugging and small chugging is represented as equation (1-8). Fig.1.7 shows the comparison of all analytical boundaries with regime map.

$$\frac{d^3(\delta r)}{dt^3} + \mathrm{A}\frac{d^2(\delta r)}{dt^2} + B\frac{d(\delta r)}{dt} + C(\delta r) = 0, \tag{1-1}$$

where

$$\mathrm{A} = \frac{h}{L} \cdot \frac{4\pi r_o^2}{V_0 + \frac{4}{3}\pi r_0^3}\left(\frac{\partial T_s}{\partial \rho_d}\right),$$

$$\mathrm{B} = \frac{\rho_s}{\rho_L} \cdot \frac{4\pi r_o}{V_0 + \frac{4}{3}\pi r_0^3}\left(\frac{\partial p}{\partial \rho_s}\right),$$

$$\mathrm{C} = \frac{8\pi h \Delta T}{L\rho_L\left(V_0 + \frac{4}{3}\pi r_0^3\right)}\left(\frac{\partial p}{\partial \rho_s}\right)$$

$$s^3 + As^2 + Bs + C = 0 \tag{1-2}$$

$$\Delta T_T = \frac{3}{2}\rho_s\left(\frac{\partial T_s}{\partial \rho_d}\right) \tag{1-3}$$

$$\Delta T_T = \rho_s\left(1 + \frac{d_V}{4z_0}\right)\left(\frac{\partial T_s}{\partial \rho_d}\right) \tag{1-4}$$

$$\Delta T_T = \frac{2\pi r_0^3 \rho_s}{V_D}\left(\frac{\partial T_s}{\partial \rho_d}\right) \tag{1-5}$$

$$\Delta T_T^{2/3} = K\left(\frac{\rho_s}{G_s}\right)^{1.3}, \tag{1-6}$$

where

$$\mathrm{K} = N_H/1.54\xi\{\quad\}^{1/3}$$

$$\Delta T_T = bG_s, \tag{1-7}$$

where b = 3.4 m^2sK/kg

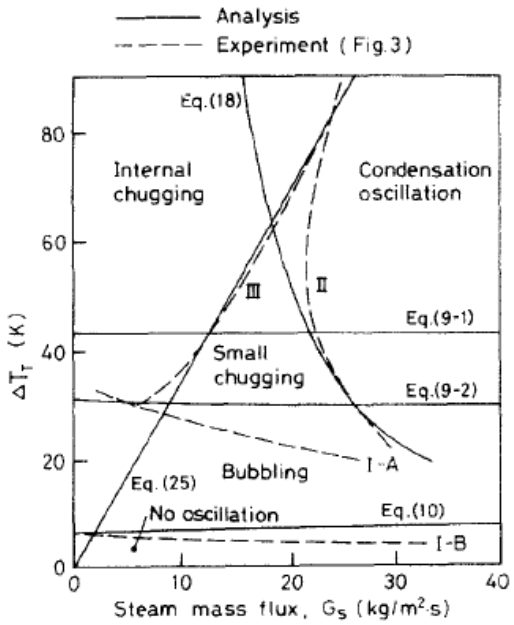

Fig.1.7 Comparison of all analytical boundaries with regime map [4]

Liang et al. (1994) classified DCC regimes by five regimes with the coordinates with steam mass flux and the pool temperature: (1) chugging, (2) low frequency bubbling with detached bubbles, (3) high frequency bubbling with detached bubbles, (4) oscillatory steam jets, and (5) stable steam jets, as shown in fig.1.5 [5]. If the condensation rate is larger than the steam supply rate, the condensation interface is drawn back into the injection pipe and chugging is initiated. They proposed transition criterion for chugging-bubbling transition developed from the transient conduction model as equation (1-8) and for bubbling-jetting transition from the two-layer turbulent eddy transfer model as equation (1-9), where ρ_f is density of liquid and ρ_s is density of vapor. Based on the information that when the steam is mixed with non-condensable gas such as air, the intensity of chugging is greatly reduced, they proposed a transient conduction-diffusion model as equation (1-10), where k_w is water conductivity, k_d^a is diffusion-equilibrium thermal conductivity of air, D_{sa} is mass diffusion coefficient of steam through a medium of air, α_w is water thermal diffusivity and x_n is content of non-condensable gas.

$$-0.06\, Re_f^{s0.5} Pr^{0.5} Ja^{-1} \leq 1.0 \tag{1-8}$$

$$0.035\left(\frac{\rho_f}{\rho_s}\right)^{1/4} Re_f^{s1/4} Pr^{1/2} N\, Bo^{2/3} Ja^{-0.7} \geq 1.0 \quad (1\text{-}9)$$

$$0.06\left(1+\frac{k_w}{k_d^a}\frac{Ja}{2}\frac{\rho_s}{\rho_a}\sqrt{\frac{D_{sa}}{\alpha_w}}x_n\right)^{0.5} \times Re_f^{s0.5} Pr^{0.5} Ja^{-1} \leq 1.0 \quad (1\text{-}10)$$

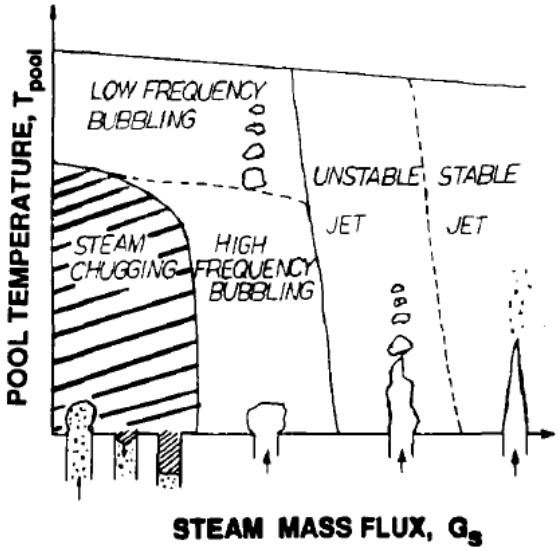

Fig.1.8 Condensation regime map [5]

Petrovic de With et al. (2007) introduced the tree dimensional regime map with the three coordinates of steam mass flux, water subcooling and injector diameter [6]. DCC is explained by three main regimes; (1) chugging regime (2) jetting regime (3) bubbling regime and four regions; (1) steam plum (2) interface (3) hot water layer (4) surrounding water. Fig.1.9 demonstrates the regions of DCC. The first region is steam plum which consists of pure steam and the plume outer surface is the interface, where DCC starts to occur. Hot water layer, which contains steam bubble, surrounds the interface in surrounding water. The hot water layer is a two-phase layer near the interface with a temperature near saturation. The condensate from the interface mixes with hot water layer with large activity of turbulent motion. The turbulence is generated from the momentum induced from condensation and affects critically the shape of interface and the condensation rate. Based on a large number of independent studies published, 3D map was introduced as shown in fig.1.10.

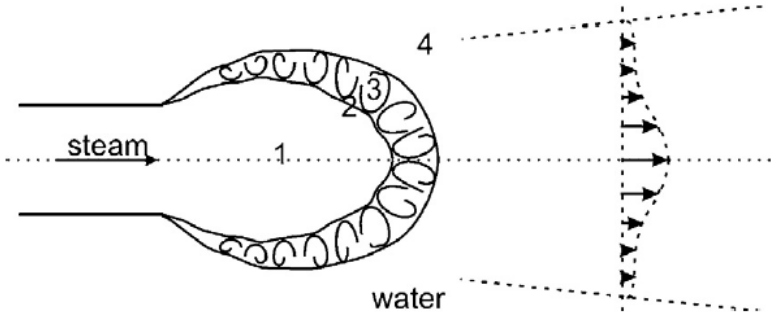

Fig.1.9 The schematic of DCC regions [6]

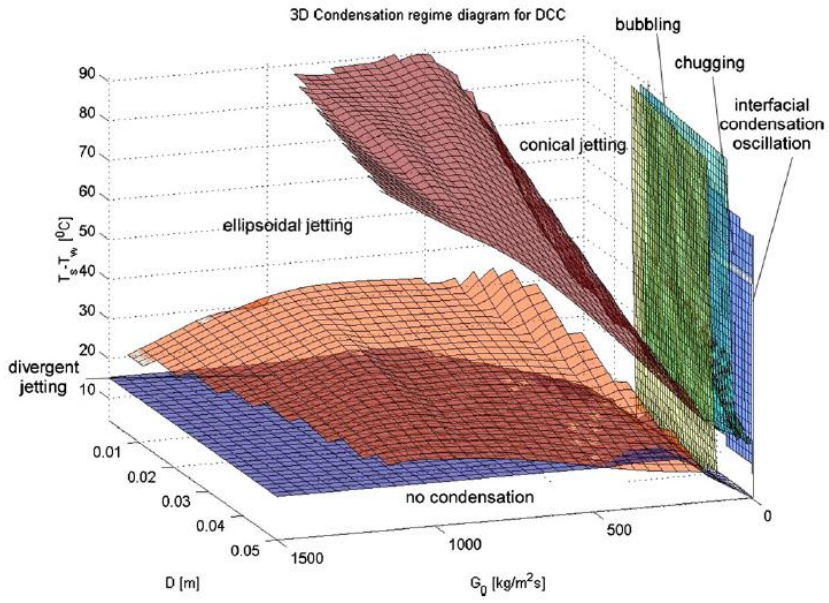

Fig.1.10 3D condensation regime map [6]

To apply to the simulation of thermal stratification, more information about steam bubble motion such as downward bubble amplitude and the frequency should be known. The momentum from condensation interface would be affected by the amplitude and the frequency. The amplitude and the frequency would be the function of mass flow rate, subcooling and etc.

1.3.1.2 Evaluation of the shape and the length of steam plume

Kerney et al. (1972) introduced an equation to predict the steam plume length with an error of 11.7 % with an extensive range of experimental variables as shown in equation (1-11) [7]. The experiments were carried out at atmospheric pressure with pool temperatures in the range 301-358K, injector exit diameter in the range 0.40-11.2 mm, mass flux in the range 332-2050

kg/m^{2}s. It belongs to the divergent jetting regime and ellipsoidal jetting regime. This equation is regarded to be suitable for chocked injector flow at values of dimensionless driving potential no less than 0.028. Fig.1.11 shows the schematic of the condensing jet model.

$$\mathrm{XB} = 0.7166\mathrm{B}^{0.1689}\left(\frac{G_0}{G_m}\right)^{0.6446} \tag{1-11}$$

where

$$\mathrm{B} = C_p(T_s - T_\infty)/h_{fg}$$

$$G_m = 275\ kg/m^2s$$

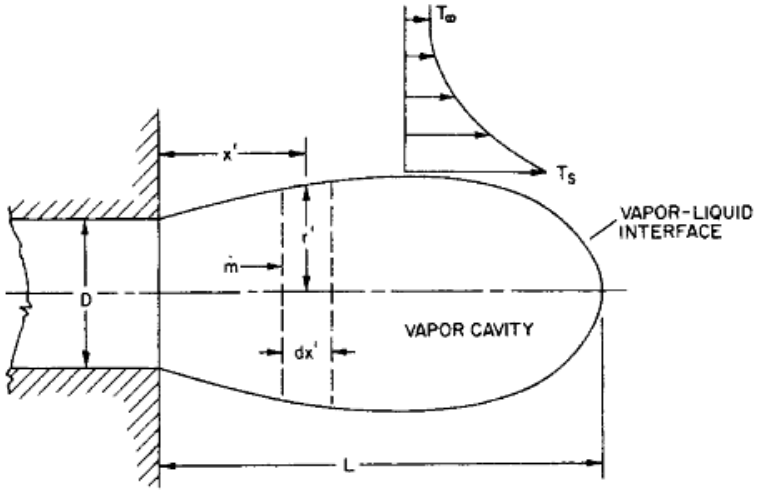

Fig.1.11 Schematic of the condensing model [7]

H. Nariai et al. developed linear frequency analysis and large amplitude oscillation analysis for condensation oscillation and plug oscillation, and for chugging and ON-OFF oscillation respectively [8-10]. Fig.1.12 shows the analysis model for large chugging. Equation (1-12), (1-13) and (1-14) represent the water level, frequency and the amplitude equation for chugging regime.

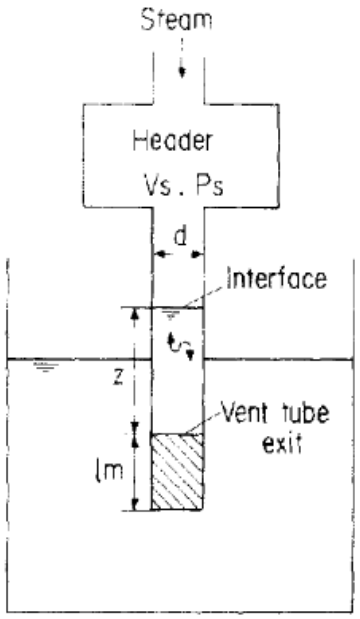

Fig.1.12 Analysis model of large chugging [10]

$$z(t) = C \sin \omega_C t - \frac{D}{\omega_C^2} t \quad (1\text{-}12)$$

$$\omega_C^2 = \frac{g}{\bar{z}+l_m}\left(1 + \frac{\pi \kappa P_{s0} d^2}{4\rho_L g V_s}\right) \quad (1\text{-}13)$$

$$D = \frac{\pi \kappa G_0 P_{s0} d^2}{4\rho_L \rho_{s0} (\bar{z}+l_m) V_s} \quad (1\text{-}14)$$

Chun et al. (1996) investigated steam plume and the heat transfer coefficient experimentally at the mass flux higher than 200 kg/m^{2}s [12]. They obtained the correlations for dimensionless steam plume lengths and average steam-water DCC heat transfer coefficient as shown in equation (1-15) and (1-16). From this research, it is known that the subcooling is not important for the average heat transfer coefficient and the average heat transfer coefficient increases significantly as the nozzle diameter is reduced. The major controlling parameter in the DCC energy transport is the steam mass flow rate. Fig.1.13 represents the steam plume shape distribution map and fig.1.14 shows the steam plume shapes observed with horizontal nozzles; (a) conical shape, (b) ellipsoidal shape and (c) divergent shape.

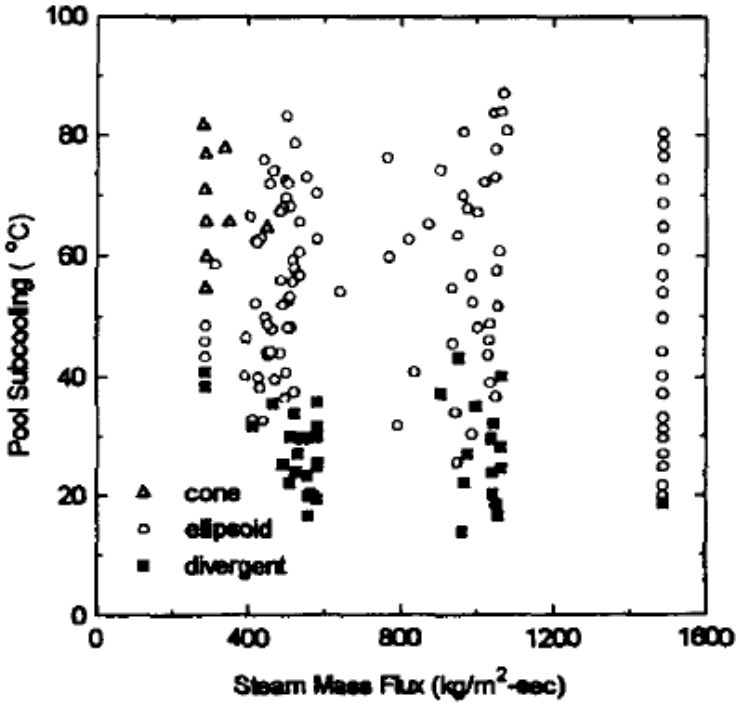

Fig.1.13 Steam plume shape distribution map [12]

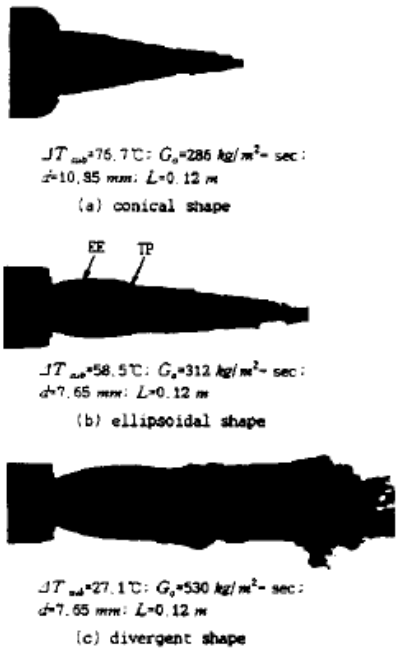

Fig.1.14 Steam plume shape [12]

$$\frac{l}{d} = 0.5923\mathrm{B}^{-0.66}\left(\frac{G_0}{G_m}\right)^{0.3444} \quad (1\text{-}15)$$

$$h = 0.8012\, C_p G_m\, \mathrm{B}^{-0.6247}\left(\frac{l}{d}\right)^{-1.0079}\left(\frac{G_0}{G_m}\right)^{0.7185} \quad (1\text{-}16)$$

Petrovic (2005) proposed a mathematical model to predict condensation interface [13]. The characteristics of the steam plume is decided by subcooling, steam flow rate, shape of the pool, position, and direction of the steam pipe. The proposed model was employed to predict steam plume length for four different axially symmetrical steam plume shapes. In order to validate the computational predictions, experimental data by Chun et al. (1996) were used [9]. This model could be expressed as an integral equation with 4 different plume shapes as equation (1-17). It is represented that the spherical model shows better agreement with experimental data for the lowest heat transfer coefficient and the conical model for the highest one.

$$\int_{\dot{m}}^{0} d\dot{m} = -\frac{h_i}{h_{fg}}\Delta T 2\pi \int_0^l f(x)\sqrt{1 + f'^2(x)}\, dx \quad (1\text{-}17)$$

- Conical $\mathrm{f(x)} = -\left(\frac{\mathrm{R}}{\mathrm{l}}\right)\mathrm{x} + \mathrm{R}$
- Parabolic $\mathrm{f(x)} = \mathrm{R}\sqrt{l - x/l}$
- Ellipsoidal $\mathrm{f(x)} = \mathrm{R}\sqrt{l - x^2/l^2}$
- Spherical $\mathrm{f(x)} = \sqrt{(1-a)^2 - (x-a)^2}$

A. de With (2009) presented two-dimensional steam plume length diagram for DCC referring to the correlations of other researchers [14]. Fig.1.15 shows correlation information of other researchers and fig.1.16 demonstrates the two-dimensional steam plume length diagram.

Authors	Correlation L/D	Error (%)	Validity
Kerney et al. (1972)	$0.2588B^{-1}(G_0/G_m)^{0.5}$ $0.3583B^{-0.8311}(G_0/G_m)^{0.6446}$	13.6 11.7	$D = 0.00495$ m $G_0 \in (338, 1240)$ kg/(m^2 s) $B \in (0.0028, 0.135)$
Weimer et al. (1973)	$17.75B^{-1}(G_0/G_m)^{0.5}(\rho_s/\rho_\infty)^{0.5}$ $10.285B^{-0.801}(G_0/G_m)^{0.713}(\rho_s/\rho_\infty)^{0.384}$	21.9 13.0	$D = 0.00317$ m $G_0 \in (321, 1136)$ kg/(m^2 s) $B \in (0.0025, 0.063)$ $\rho_\infty/\rho_s \in (3980, 27700)$
Chun et al. (1996)	$0.5923B^{-0.66}(G_0/G_m)^{0.3444}$		$D = 0.00135$ m $G_0 = 1488$ kg/(m^2 s) $B \in (0.035, 0.15)$
Kim et al. (2001)	$0.503B^{-0.70127}(G_0/G_m)^{0.47688}$		$D = 0.005$ m $G_0 = 1188$ kg/(m^2 s) $B \in (0.037, 0.12)$

Fig.1.15 Different correlations of dimensionless steam plume length published [14]

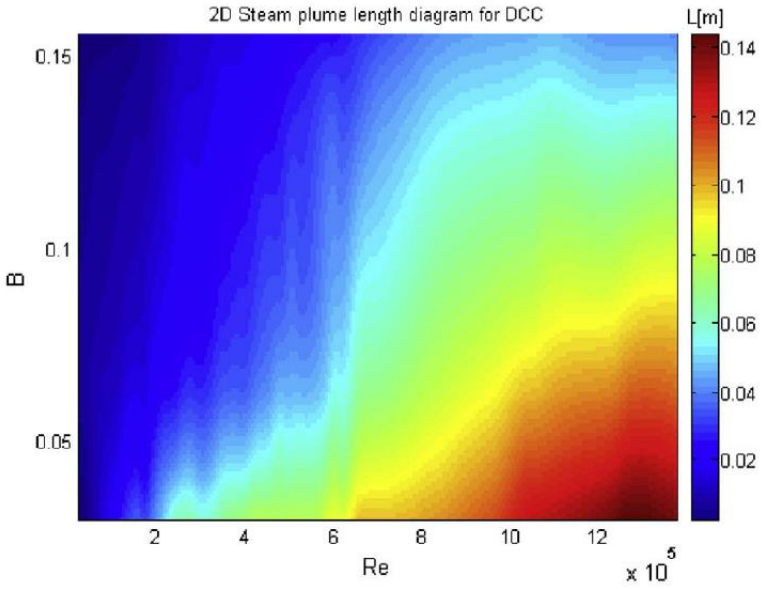

Fig.1.16 Two-dimensional steam plume length diagram [14]

These researches are at the high mass flux ranges but there are no research carried out paying attention to other regimes at lower mass flux ranges since the unstable characteristics like chugging motion make it difficult to define condensation interface theoretically. The behavior of condensation interface at lower mass flux should be studied to understand thermal stratification related to DCC.

There are various studies related to DCC about chugging motion, non-condensable gas effects, steam plume behaviors [15-17, 40].

1.3.1.3 Heat transfer coefficient in DCC

Aya et al. (1991) examined the heat-transfer coefficient in direct-contact condensation between cold water and steam using past experimental data and analyses [18]. Fig.1.17 shows the summary of heat-transfer coefficient in direct contact condensation they mentioned in the paper. They assumed that the representative parameters which influence the heat transfer coefficient are steam mass flux, distance and subcooling. They studied several categories of DCC; steam condensation in pool water, cold water injection into steam flow, water injection into steam space. For steam condensation in pool water, they proposed regime map as shown in fig.1.18;chugging, condensation oscillation and bubbling. They compared the experimental data with Young's correlation as equation (1-18) for chugging regime and Fukuda's correlation as equation (1-19) for condensation oscillation regime.

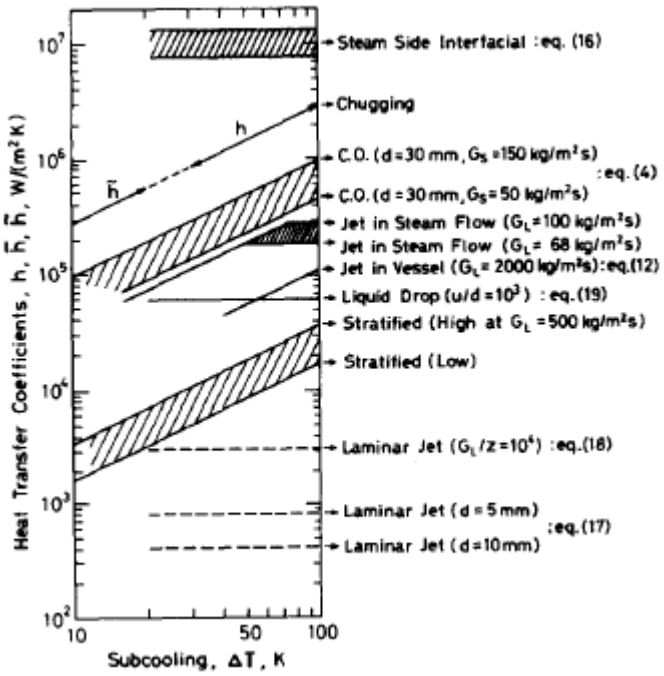

Fig.1.17 Summary of heat-transfer coefficient in direct contact condensation [18]

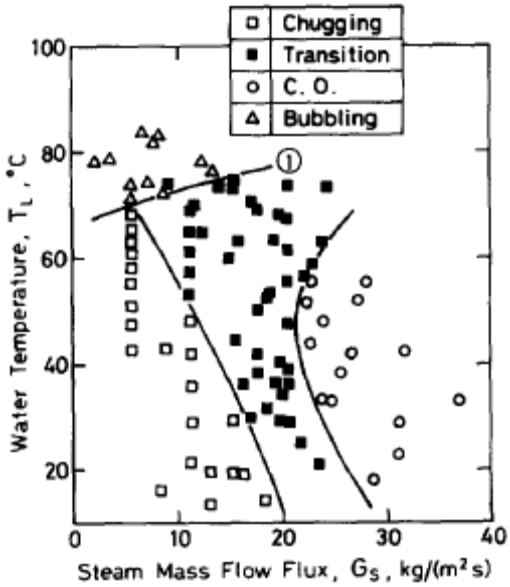

Fig.1.18 Regime map for steam condensation in pool water [18]

$$\mathrm{h} = 6.5\rho_L c_{PL} u_s^{0.6} \left(\frac{\nu_L}{d}\right)^{0.4} \tag{1-18}$$

$$\bar{h} = 43.78 \frac{\lambda_L}{d} \left(\frac{d G_s}{\rho_L \nu_L}\right)^{0.9} \frac{c_{PL}\Delta T}{L} \tag{1-19}$$

Murata et al. (1992) investigated heat transfer coefficient by DCC at a steam subcooled water interface in a horizontal channel by using three types of models; the modified k-ε model, surface renewal model and heat conduction model [19]. They compared the results with the experimental data of Lim et al. and Murata et al. The modified k-ε model, which simulates the near-interface variation of the turbulence quantities, represented the better agreement with the experimental results than wall k-ε model. The surface renewal model, which assumes that the molecular diffusion is renewed by the surface renewal eddies with the surface renewal rate as shown fig.1.19, without wave effect showed a value close to the modified k-ε model and the Lim's correlation for smooth interfaces. When the wave effect is added to the surface renewal model, the results with interfacial waves were predicted.

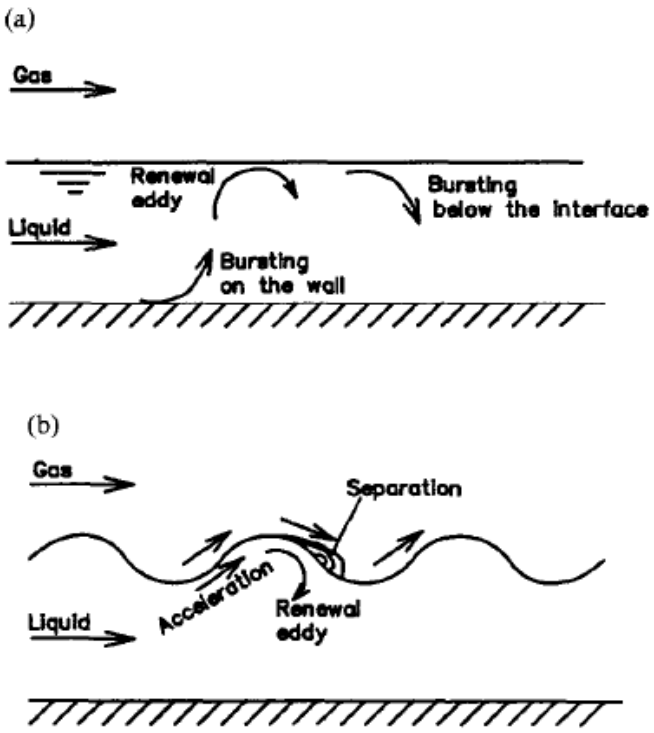

Fig.1.19 Conceptual sketch of the surface renewal model [19]:
(a) for a smooth interface (b) for a wavy interface

Murase et al. (1993) examined experimentally the evaporation and condensation behavior under a noncondensable gas presence with an external water wall type containment vessel as shown in fig.1.20 [20]. The system pressure was regarded as the sum of the noncondensable gas pressure and saturated steam pressure in the wetwell. The evaporation heat transfer coefficient and the condensation heat transfer coefficient were represented as following equations. They are calculated with the mass ratio of steam and air on the heat transfer surface; SP water surface for evaporation and PCV inner surface of gaseous area for condensation. Since the local noncondensable gas pressure was much lower on the evaporating pool surface than on the condensing liquid surface, the evaporation heat transfer coefficients were one order higher than the condensation heat transfer coefficients.

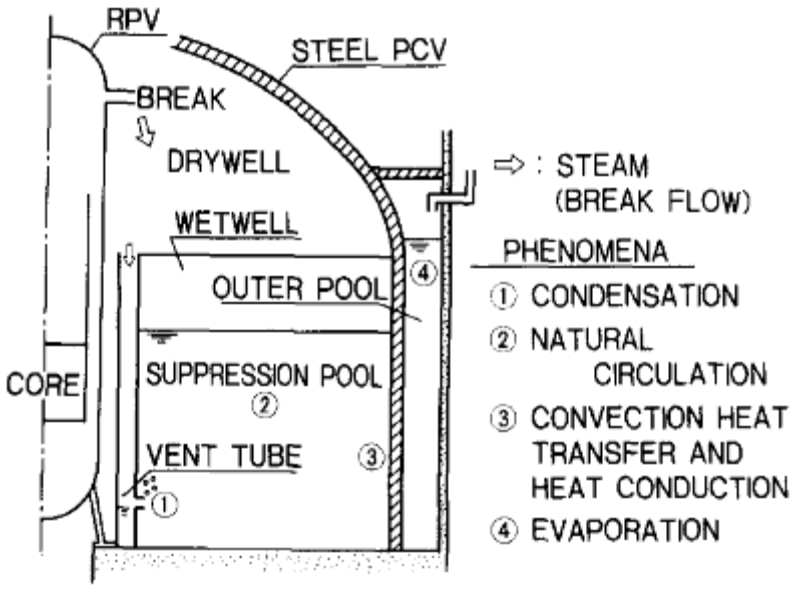

Fig.1.20 Concept of external water wall type primary containment vessel [20]

$$h_e = 3.2(M_{st}/M_a)^{0.65}\ [kW/m^2K], \qquad 0.033 < (M_{st}/M_a) < 0.47 \tag{1-20}$$

$$h_e = 5.2(M_{st}/M_a)^{1.3}\ [kW/m^2K], \qquad 0.47 < (M_{st}/M_a) < 1.2 \tag{1-21}$$

$$h_c = 0.47(M_{st}/M_a)\ [kW/m^2K], \qquad q_c L_c \leq 40kW/m \tag{1-22}$$

Fujii et al. (1996) investigated evaporation and condensation heat transfer with logarithmic mean concentration, which is calculated with steam concentration and air concentration of bulk and heat transfer surface as shown in fig.1.21 [21]. The evaporation and condensation HTCs are expressed as following equations.

$$h_e = 1.43(\bar{C}_s/\bar{C}_a) \qquad [kW/m^2K] \qquad [0.5 \leq \bar{C}_s/\bar{C}_a \leq 100] \tag{1-23}$$

$$h_c = 0.48(\bar{C}_s/\bar{C}_a)^{0.85} \qquad [kW/m^2K] \qquad [0.05 \leq \bar{C}_s/\bar{C}_a \leq 50] \tag{1-24}$$

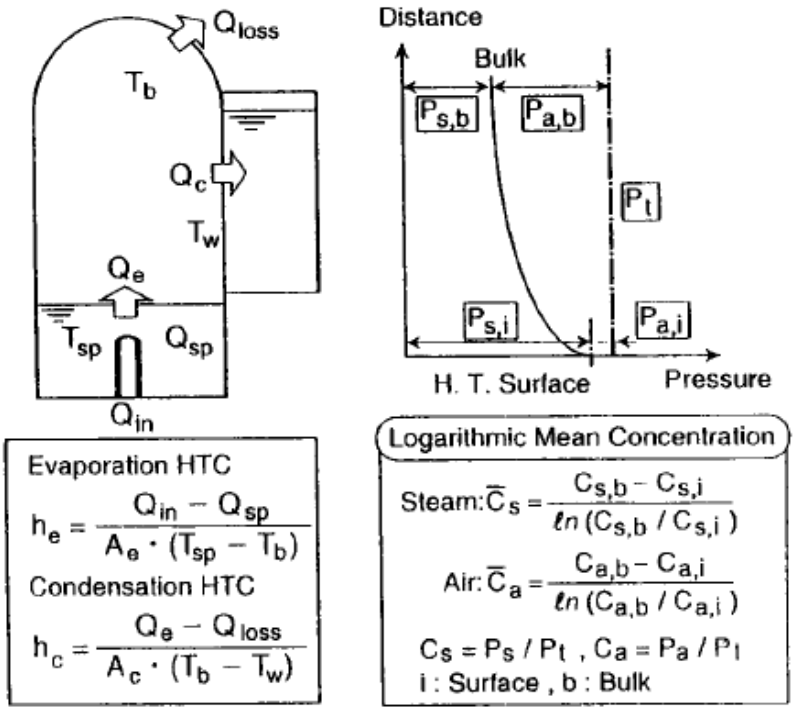

Fig.1.21 Evaluation of HTC [21]

1.3.2 Thermal stratification and SP mixing by DCC

1.3.2.1 Experiments and the validation of the analytical model

The researches regarding to thermal stratification and pool mixing by direct contact condensation were carried out experimentally and analytically by several groups. There are several studies about thermal stratification and mixing phenomenon by Direct Contact Condensation (DCC) in water pool experimentally and analytically [22-38]. S. G. Bankoff (1980) reviewed the studies of steam condensation with subcooled water with turbulent gas absorption models, corrections of condensing mass transfer, stratified horizontal condensing flows, steam bubble collapse and pressure suppression pool studies [22]. R. E. Gambler et al. (2001) investigated pressure suppression pool mixing and thermal stratification with several hot water jets and validated a system simulation code, TRACG, with experimental data [23]. E. Krepper et al. (2002) carried out natural convection experiment in large pools with heating pipes and compared to simulation results by CFX-4 [24]. L. Cheng et al. (2006) found that the pool

mixing is strongly influenced by the noncondensable gas flow rate with PUMA facility [25]. Y. J. Choo et al. (2010) studied turbulent jet and mixing pattern induced by a steam injection into a pool by PIV technique [26]. T. L. Norman et al. (2010) conducted the experiments of steam and steam-air mixture injection in a subcooled pool and found that thermal stratification occurs under certain air flow rates, steam flow rates and pool temperature [27]. A system analysis code, TRACE, was compared to their experimental data [28]. H. S. Kang et al. (2008) and Y. Moon et al. (2009) simulated thermal mixing in a subcooled water tank with CFX using steam condensation region model [29, 30 and 31].

One large group is working on the validation of thermal stratification and mixing simulation using the experimental data from POOLEX test facility in Lappeenranta University of Technology [32-38]. It is named as POOLEX project. Fig.1.22 shows the schematic of POOLEX facility. They mention that the steam injection affects thermal stratification and mixing by two main mechanisms as shown in fig.1.23; 1) Localized heat source in the pool due to steam condensation and 2) Localized momentum source induced by steam injection. They call such models as EHS (Effective Heat Source) and EMS (Effective Momentum Source) approaches. For EHS, wall heat flux was used and volumetric momentum source was used for EMS. GOTHIC, BMIX++ and NEPTUNE CFD were used as numerical codes to be validated.

They considered two regimes when steam is injected into SP. The first regime is characterized by a considerable amount of non-condensed steam that flows out of the steam injection pipe. The second regime is a result of relatively small flow rate of steam and only a hot condensate with low momentum flows out. The heat flux through the pipe wall surface is uniformly distributed and the heat flux is calculated as equation (1-18).

$$H_{eff} = \frac{1}{\Delta T}\int_{t}^{t+\Delta T} H(t)\, dt \qquad (1\text{-}18)$$

The corresponding velocity induced at far field by oscillation can be calculated by $U_0 = \sqrt{2}fL$, where f is the oscillating frequency and L is the amplitude of oscillation. Momentum is calculated as equation (1-19).

$$M = \frac{\pi}{4}\rho U_0^2 d^2 \qquad (1\text{-}19)$$

To calculate the frequency and the amplitude, the Nariai's equations were used [8]. However, since they applied uniform heat flux on the pipe surface, it is difficult to involve the mechanism of oscillating condensation interface especially in chugging motion.

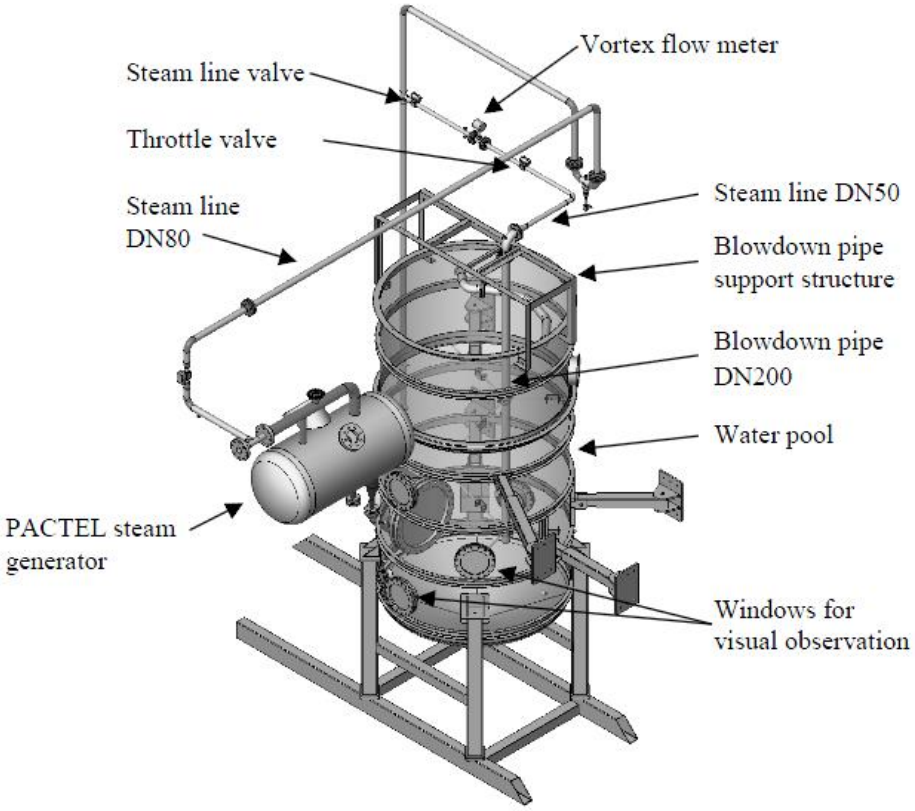

Fig.1.22 Schematic of POOLEX test facility [36]

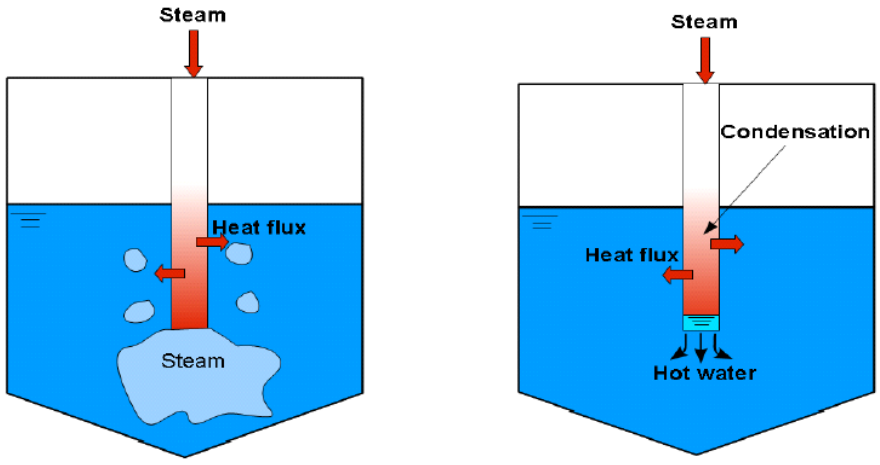

a) large flow rate of steam b) small flow rate of steam

Fig.1.23 Two regimes of steam injection into SP [37]

There are more researches about thermal stratification and SP mixing by DCC [39, 40].

1.4 Objectives

The hydromechanical mechanism of thermal stratification and the relationship between the stratification and pressure increase in SP are not known yet to the best knowledge of the author. However, the characteristic of the thermal stratification is highly affected by the DCC regimes and the generation and the collapse of thermal stratification are not easily defined. Since the pressure in SP is affected by the generation of thermal stratification sensitively, it is very important to investigate the phenomenon carefully and serve the information to the simulation of SP behavior and design of SP.

The objective of this research is to understand unexpected pressure increase of SP in Fukushima accident and give useful information to LWRs designers for nuclear safety. This research is carried out to understand thermal stratification in SP experimentally and analytically and to predict the thermal stratification by single phase CFD code. Because of complicated phenomena depending on DCC regimes and the difficulties of accurate momentum calculation from two phase simulation, single phase model is selected and additional heat and momentum models are researched. For single phase numerical simulation, the heat and momentum models are introduced in condensation interface and gas/liquid surface and validated.

CHAPTER 2 THERMAL STRATIFICATION IN PRESSURE SUPPRESSION POOL

2.1 Research targets

According to the objectives, there are three research targets as shown in fig.2.1; 2D SP model, downsized torus SP model and real sized torus SP model. Firstly, the hydromechanical mechanism of thermal stratification is investigated by 2D SP experimental model and the analytical model would be introduced. Second, the downsized torus analytical model would be introduced and validated with experimental data. Third, the analytical model would be introduced to simulate the real sized torus SP.

2.1.1 2D Suppression Pool Model

Two dimensional suppression pool model was designed to study the mechanism of thermal stratification. On the front of the SP, there is large glass window for visualization and optical measurement such as PIV (Particle Image Velocimetry) and flow visualization. There are side windows on the left and right side of SP for laser illumination. One steam injection pipe is submerged to the water inside SP. The analytical models were generated and validated with experimental results.

2.1.2 Downsized Torus Suppression Pool Model

20:1 downsized torus model was designed and equipped in Tokai campus of the University of Tokyo. Analytical model was made and validated with the experimental data.

2.1.3 Real Sized Torus Suppression Pool Model

It is very difficult and dangerous to do the DCC experiment on the real scale. Only analytical model was made and compared with the Fukushima accident.

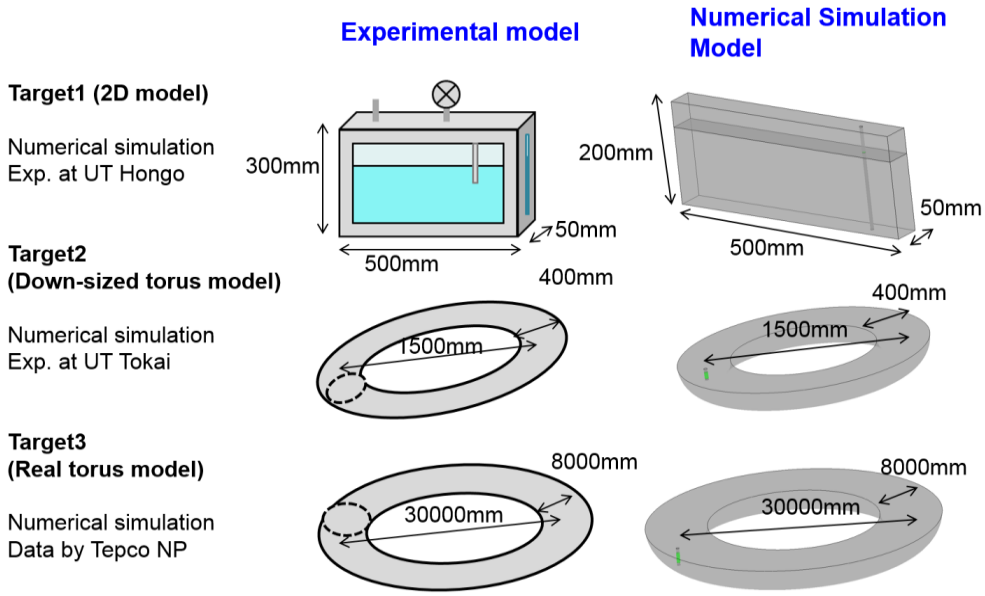

Fig.2.1 Research targets

2.2 Critical factors for thermal stratification

Thermal stratification is formation of horizontal liquid layers with a change in the temperature at different depths in the storage, and is due to the change in water's density with temperature. If the force in the direction of gravity from heat source is not stronger than buoyancy force induced by the water density difference, only the water over the position of the heat source is heated by natural convection. Especially, the top area of the liquid has much higher temperature than other area. Since the gas pressure is influenced by the temperature of the liquid top area, the pressure of the pool increases abnormally. This will lead to reduction of pool's pressure suppression capacity.

In case of lower steam flow rates into SP, thermal stratification may occur due to the weak momentum of condensate which cannot generate large advection in SP in certain conditions. Undesired accumulation of hot condensate plume at elevated locations of the pool due to its lower density may degrade condensation and heat absorption capability of SP. Hot water-gas interface in SP can cause pressure increase in wetwell that may augment the risk of containment damage.

2.2.1 Direct Contact Condensation

In various industrial two-phase flow systems such as condensers, boilers and nuclear coolant systems, the injection of vapor into same substance subcooled liquid is a common event. When the vapor condenses on the interface between the vapor and the liquid, it is called as direct contact condensation (DCC). It is used as a method to depressurize gaseous systems quickly using the large difference of specific volume. For example, the specific volume of saturated steam at atmospheric pressure is 1.679 m^3/kg and the one of saturated water is 1.044×10^3 m^3/kg.

By various investigators, the DCC behavior was divided into several regimes according to the subcooled temperature and steam mass flux as shown in Fig.2.2 [3]. As steam mass flux increases, the shape of the bubble and interface changes from oscillatory interface, chugging bubble, oscillatory bubble and jet. As subcooling temperature decreases, the bubble tends to be longer like ellipsoidal shape and finally escape from the pool. The chugging and oscillation of bubble are known to be due to the condensation capacity changes by the interface surface area changes. The interface surface area is changed by the unstable pressure variations.

The size of the injection pipe is included as an additional parameter for condensation regime [4]. Petrovic de With et al. (2007) introduced the tree dimensional regime map with steam mass flux, water subcooling, and injector diameter. DCC is explained by three main regimes; (1) chugging regime (2) jetting regime (3) bubbling regime and four regions; (1) steam plum (2) interface (3) hot water layer (4) surrounding water.

It is important in thermal stratification formation which regime of DCC is represented since the different regime demonstrates different momentum near interface and hot water layer.

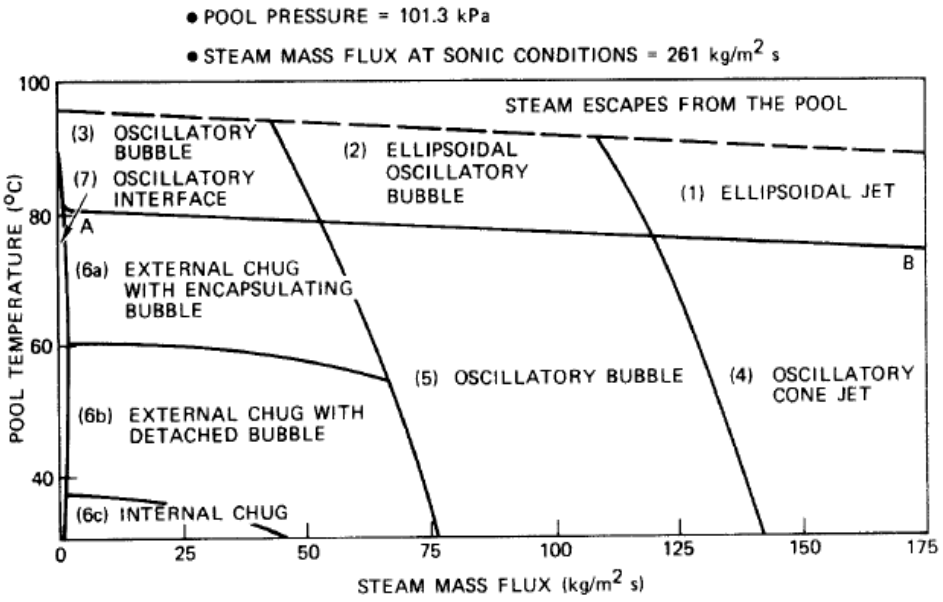

Fig.2.2 The condensation regime map [3]

2.2.2 Buoyancy and Inertia

The balance between buoyancy and inertia decides whether the flow becomes forced jet or plume around the condensation interface. This means whether the hot water layer has initial momentum or not. Forced jet would mix the water inside SP and disturb thermal stratification up to the area in which buoyancy is more dominant than inertia. If plume is directly shown after DCC, well-established thermal stratification would happen. Richardson number represents the transition between forced jet and plume, which is the nondimensional number deciding whether the convection is forced or natural.

$$\mathrm{Ri} = \frac{\mathrm{Gr}}{\mathrm{Re}^2} = \left(\frac{\rho_a - \rho_{jet}}{\rho_a}\right)\frac{gD_0}{{u_0}^2} \qquad (3\text{-}1)$$

2.2.3 Natural Convection

Buoyancy acts as a driving force inside SP. As the density difference between condensate and ambient fluid is larger, the buoyancy is getting larger. Upward motion due to buoyancy is

represented as natural convection. The upward motion causes one large circulation in mixing area. This natural convection performs a role for serving the ambient fluid to condensation region. This natural convection would decide the mixing interface.

2.2.4 Momentum

Momentum from the DCC region does an important role for deciding the mixing interface. It means that when momentum is higher, the mixing interface would be lower, the mixing area would be larger, and the characteristic of the thermal stratification would be changed because the fluctuating condensate from DCC would come down into the mixing interface and make larger natural circulation. Large momentum would change the shape of natural circulation as well.

2.2.5. Pressure Balance in Pressure Suppression Pool

2.2.5.1 Partial Pressure Calculation

The pressure of SP is decided by the gas pressure. The gas pressure is decided by the gas temperature and the gas temperature is decided by the temperature of the top of the liquid. When the SP is well mixed, the temperature of the liquid top would be similar to the volume-averaged temperature. However, when thermal stratification occurs, the temperature of liquid top would be different from it and the pressure would be increased faster than expected.

2.2.5.2 Effect of Non-condensable gas

Non-condensable gas would interrupt the DCC and the non-condensable bubble would enhance upward flow. Lee et al. studied the effect of non-condensable gas on DCC of steam and air mixture and found that the average heat transfer coefficients decrease significantly when air mass fraction increase [22]. Large amount of non-condensable gas would make the flow highly complicated. It makes the SP pressure increase as well.

CHAPTER 3 DOWNSIZED 2D SUPPRESSION POOL MODEL

3.1 Experiment

3.1.1 Experimental Setup and Methods

3.1.1.1 Experimental Device

To investigate the mechanism of the thermal stratification, a rectangular downsized suppression pool model was designed and installed as shown in Fig.3.1. The SP is connected to a steam generator by a steam pipe line. This system is covered by heat isolation material and the main steam line is covered by line heaters for steam not to be condensed inside the pipe before the steam injection exit. Steam is controlled by a valve and the steam generation is controlled by a voltage regulator.

For temperature measurement, T-type thermocouples were installed inside SP and steam injection pipe. For pressure measurement, pressure transducer (Sensez, HLVC-100KP-02) were installed inside SP. For velocity measurement by PIV, a high-speed camera (PHOTRON, Fastcam APS RS) and 532 nm continuous laser (Sintec Optronics, ST-I-N-532) were equipped.

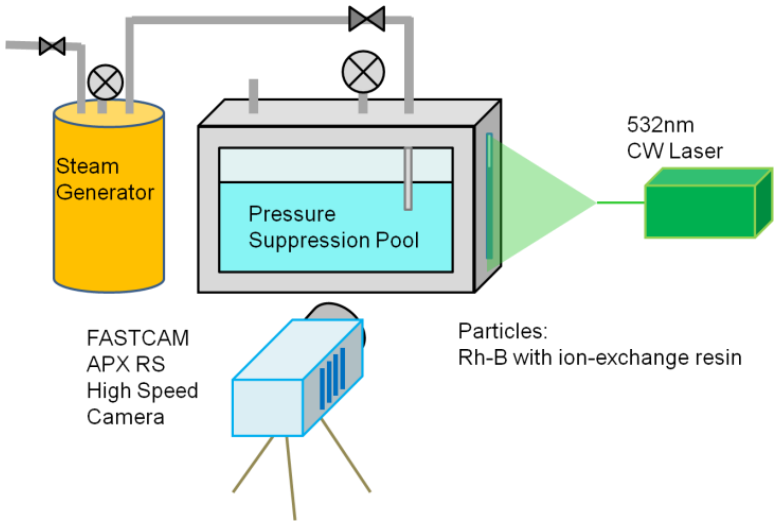

Fig.3.1 The schematic of 2D downsized SP system

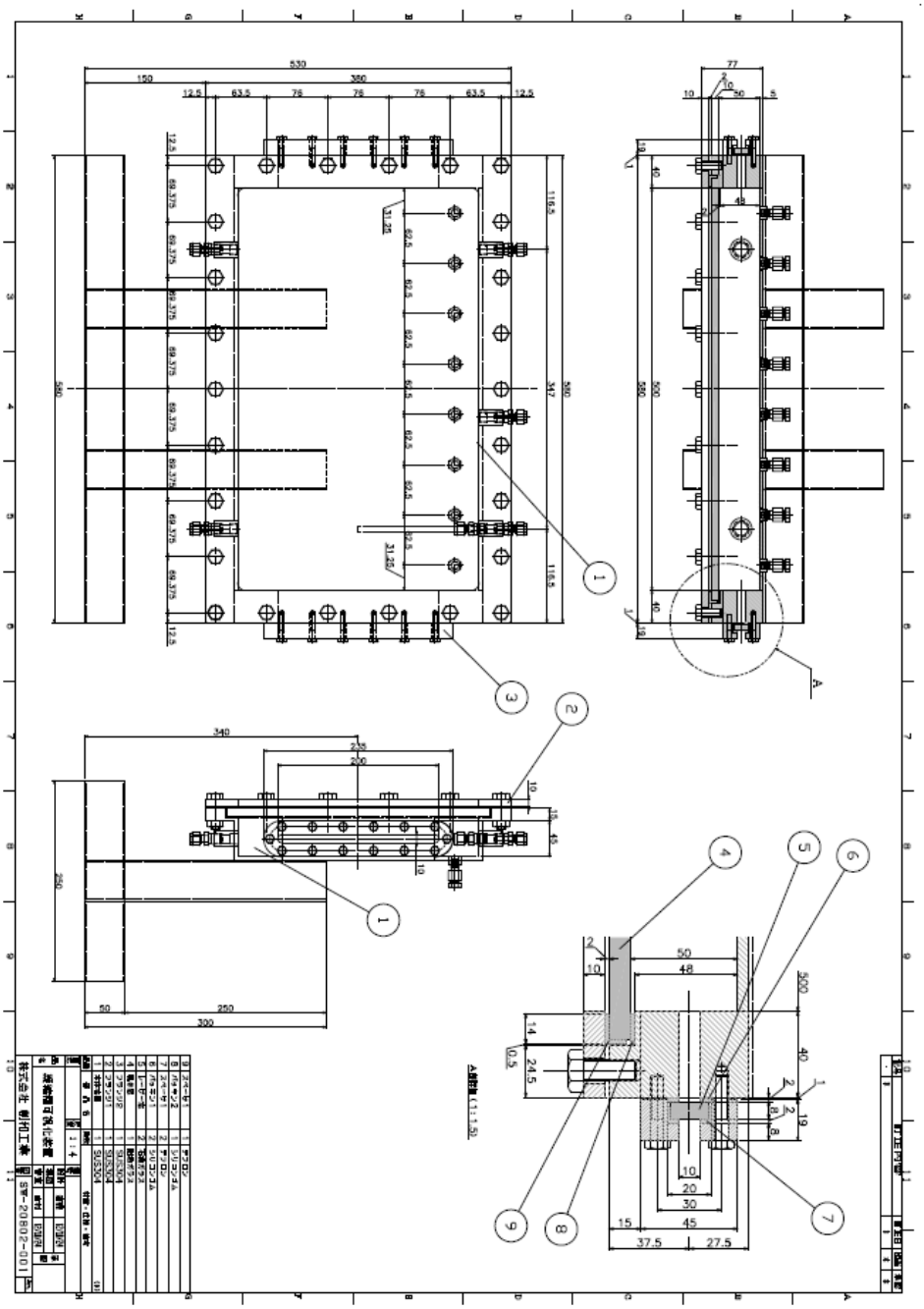

Fig.3.2 The draft of SP

The inner size of the SP is 500mm × 300mm × 50mm. Fig.3.2 shows the draft. It has the one large front glass window for visualization and two side windows for illumination. The SP was made of stainless still and glass. The outer diameter of the steam injection pipe is 6.4 mm and the inner diameter of it is 4.2 mm.

3.1.1.2 Experimental Procedure

Before starting the experiment, there are several things to be checked and controlled. For this experiment, the non-condensable gas should be removed before experiment since the non-condensable gas would interrupt the DCC and affect the entire flow of water. And for the safety, the experiments are carried out under atmospheric pressure. To control such initial conditions, following steps are needed before experiment. Step (1) is conducted to reduce the non-condensable gas inside the steam generator. To control the pressure of SP, a vacuum pump (G-10DA, ULVAC KIKO. Inc.) was used.

(1) Heating up steam generator (SG), boiling, and blowing out steam outside for 10 min.

(2) Closing all the valves and switching of the power of SG and cooling down for 3 hours

(3) Checking the water level of suppression pool (SP) and SG

(4) Closing the valve between SP and SG and Making the setting pressure in SP and closing all the valves of SP

(5) Making the setting pressure in SG by vacuum pump and closing all the valves of SP

(6) Switching on the voltage regulator to heat the water in SG and controlling the voltage to 100V before the boiling temperature in the pressure

(7) Controlling the voltage to setting voltage when the SG pressure matches with the SG setting pressure

(8) Opening the valve between SP and SG

(9) Waiting the steam bubble stable

(10) Recording the data

3.1.1.3 Temperature Measurement

3.1.1.3.1 T-type Thermocouples and the Arrangement

Thermocouples (TC) are widely used temperature measurement sensors. Different types of thermocouples are composed of different kinds of chemical alloy and have different sensible ranges of temperature. T-type thermocouples are composed of copper and constantan and suited for measurements in the −200 to 350 °C range. The T-type thermocouples were installed inside SP and Fig.3.3 shows the arrangement. 16 thermocouples were installed for liquid temperature measurement and one was installed for temperature measurement gaseous part inside the SP.

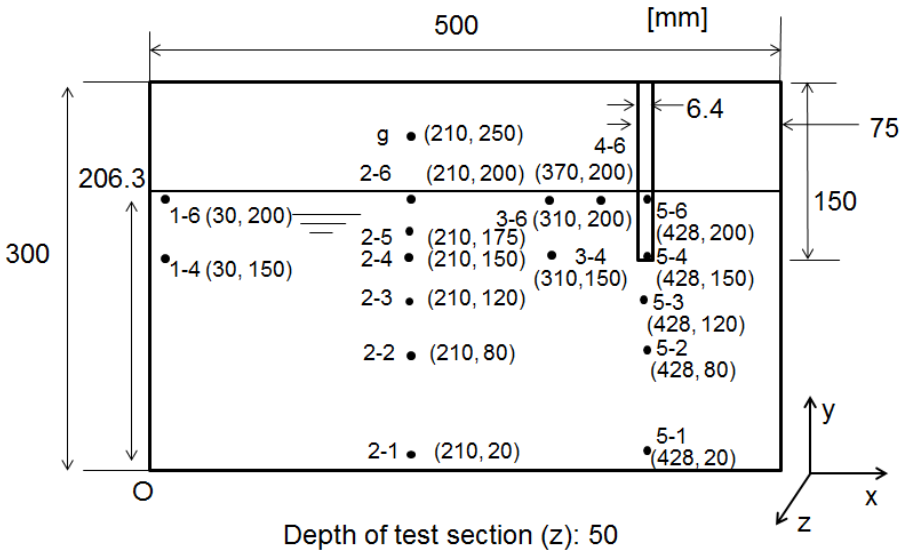

Fig.3.3 The arrangement of thermocouples (TC)

3.1.1.4 Pressure Measurement

3.1.1.4.1 Pressure Transducer

Pressure of SP was measured by pressure transducer. The thermocouples and the pressure transducer are connected to a data logger (KEYENCE, NR-TH08) and the electric signals are changed to temperature and pressure data. The range of the pressure transducer is from -100 kPa to 100 kPa at gage pressure.

3.1.1.5 Velocity Measurement

3.1.1.5.1 PIV and the Optical Setup

PIV (Particle Image Velocimetry) is the latest velocity measurement technique. It is the two or three dimensional measurement technique which can be distinguished with point-wise measurement technique such as LDV (Laser Doppler Velocimetry) and hot-wire anemometers. Using high speed camera, continuous images which shows the illuminated tracers are obtained. The continuous images are used to calculate the correlation number in selected interrogation windows and the amount of particles movement is calculated.

The two-dimensional velocity fields around a steam injection pipe inside the SP were measured using particle image velocimetry (PIV) technique. To visualize the fluid motion, the water was seeded with fluorescent particles (with a mean diameter of 4μm). The density of the particle is around 1.01-1.03 g/cm^3, which is suitable for the use as a tracer for liquid (water) flow. The traceability of the PIV particles was considered to be high and the particles could follow the fluid streamlines closely.

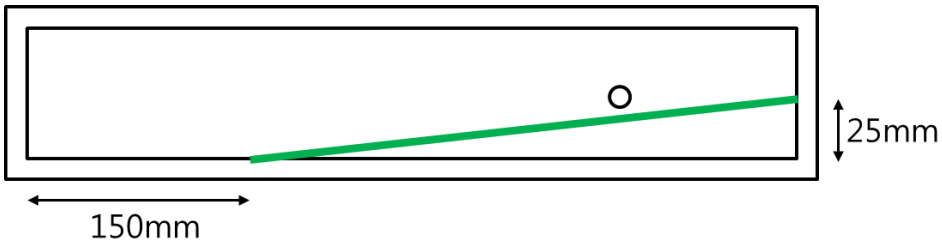

Fig.3.4 The laser sheet position (Top view)

532 nm continuous laser (Sintec Optronics, ST-I-N-532) was chosen to illuminate the flow around the steam injection pipe. The laser sheet illuminated the target area to provide a field of view for a high speed camera (PHOTRON, Fastcam APX RS) at approximately 134 mm x 134 mm. The visualization plane was at the center of depth wise direction. Laser sheet was injected from right side and passed in front of steam injection pipe as shown in Fig.3.4. Since the emission spectrum maximum of Rh-B dissolved in water is near 580 nm, red color short wave cutoff filter (SIGMA KOKI, SCF-50S-60R), of which transmission limit wavelength is 600 nm, was used to acquire fluorescent images and cut reflective light and errors.

Fig.3.5 shows an example of original images. The light scattered by the particles inside the fluid in the direction perpendicular to the laser sheet was recorded on the high speed camera. A spatial resolution of 1024 x 1024 pixels for the camera was selected. During each continuous run, a total of 500 images were captured at the frame rate of 500. From these images, instantaneous velocity vector maps were processed and analyzed using the recursive PIV analysis technique.

Three cylindrical lenses were used to produce a thin light sheet. One cylindrical lens with a focal length of 500 mm was used to make the laser sheet thin. Additionally, one cylindrical convex lens (Sigma Koki, CLB-1020-15PM) and one cylindrical confocal lens (Sigma Koki, CLB-1020-15NM) with focal length of 15 mm were used to expand the area of the laser sheet. The positions of the lenses were adjusted to produce a laser sheet about 1 mm in thickness.

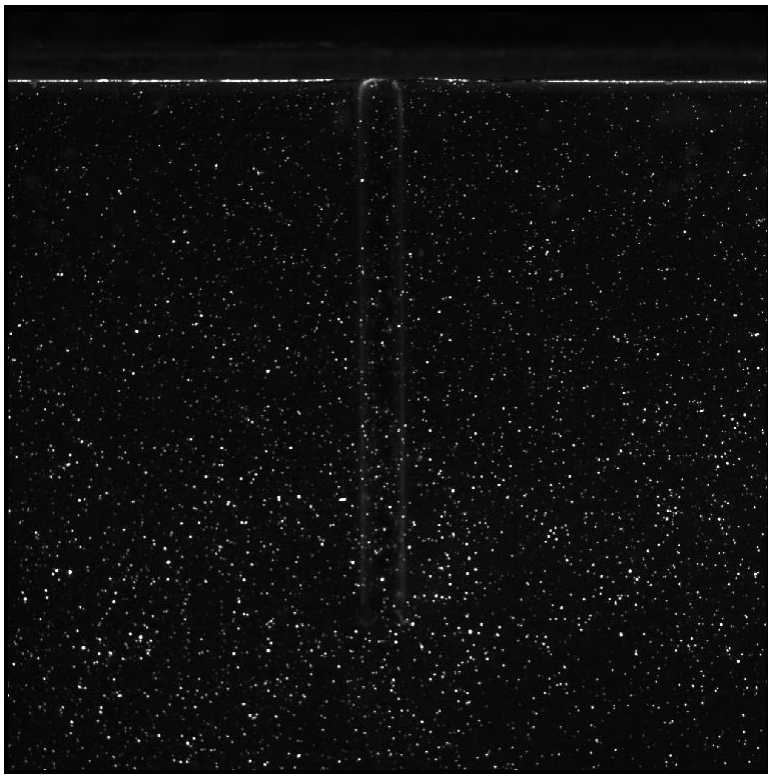

Fig.3.5 Example of original image for PIV

The first iteration started with an interrogation area of 64 x 64 pixels and 50% constant overlap ratio. The calculated displacements are passed to the next iterations as an initial displacement to perform the symmetric window shift with respect to the interrogation locations. It has been shown to reduce the rms error for the flows with high turbulence intensity. The same process ends the calculation with the size of 32 x 32 pixels interrogation size resulting in 16 x 16 pixels vector grid spacing.

3.1.2 Heat Input and Heat Loss

3.1.2.1 Measurement of Heat Input

To calculate heat input from DCC, two methods could be considered. First, from the power of heater, with the latent heat and the power, heat could be calculated assuming the steam saturated and getting the latent heat by the saturation pressure. Second, from measuring the

water level changes of the test section, with the latent heat and the mass of condensate, heat could be calculated. It is regarded to choose second method because this system has heat loss around boiler and second method does not include that factors. Although the heat loss occurs around main steam pipe line, those are covered by insulators and line heater to keep steam not to condense.

Equation (3-2) and (3-3) shows how to calculate the heat input by the amount of condensate by the second method, where Δz is water level changes in SP, A_{xy} is the area of water top, ρ_{water} is the condensate density, and t is the time that the experiment is carried out.

$$\dot{m} = \lim_{\Delta t \to 0} \frac{\Delta m}{\Delta t} = \frac{dm}{dt} = \frac{\Delta z \times A_{xy} \times \rho_{water}}{t} \tag{3-2}$$

$$q = h_{fg} \times \dot{m} \tag{3-3}$$

3.1.2.2 Measurement of Heat Loss

Since the whole amount of heat input is not large enough to neglect the heat loss, heat loss should be considered to apply this system to numerical simulation. The cooling test was carried out to calculate the overall heat transfer coefficient and compared with theoretical values. Heated water was injected into SP and kept for a while to heat up the entire experimental device. The water was cooled down for 1 hour and the temperature was measured. Fig.3.6 shows the temperature transients on the center line when cooling down the water. Without the point 2-1, the other points show quite similar temperature transients and the gradients. It shows almost linear motion and the experimental overall heat transfer coefficient, U_{ex}, could be calculated as one constant, 6.37 W/m^{2}K, at these temperature range.

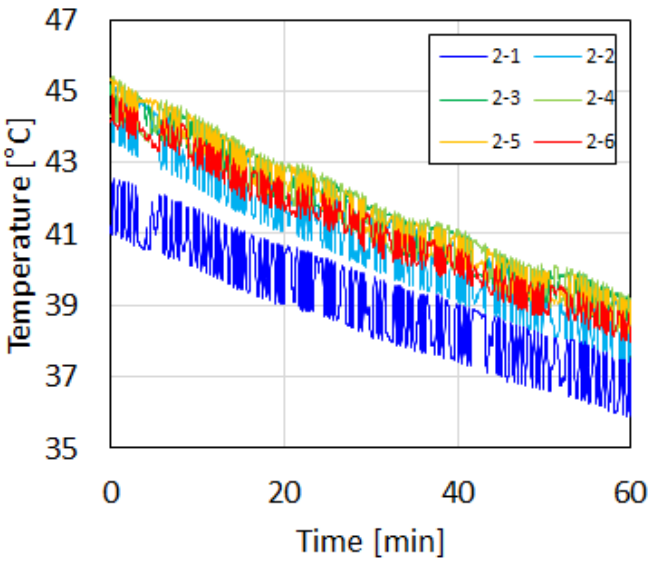

Fig.3.6 Cooling test

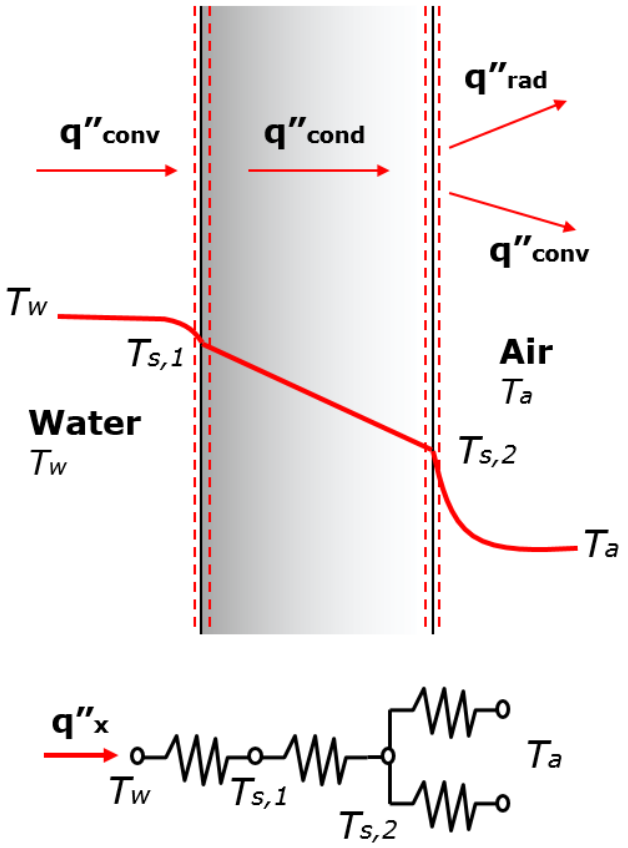

Fig.3.7 Heat transfer through a wall

(Temperature distribution and equivalent thermal circuit)

Fig.3.7 shows the schematic of heat transfer through the experimental device. From the SP water, heat is transferred to the wall by convection and transferred to the other side of wall by conduction. The heat is released by conduction and radiation to outside. Figure shows the equivalent thermal circuit. From the circuit, theoretical overall heat transfer coefficient, U_{th}, could be calculated, which is defined by an expression analogous to Newton's law of cooling. $T_{s,1}$ is assumed to be the same as the water temperature, T_w and the convection heat transfer from water to the wall surface could be neglected.

Equation (3-4) represents the relationship with three heat transfers and overall heat transfer coefficient by total thermal resistance. k_s is thermal conductivity of Stainless steel, 14.9 W/m·K at the temperature of 300K and t is the thickness of the wall, 5mm. Equation (3-5) demonstrates empirical correlations for laminar flow with vertical plate, where k_a is thermal conductivity of air, 2.63×10^{-2} W/m·K at the temperature of 300K. Equation (3-6) represents the Rayleigh number equation with Grashof number, Gr_L and Prandtl number, Pr. ν is kinetic viscosity of air, 15.89×10^{-6} m^2/s, and α is the thermal diffusivity, 22.5×10^{-6} m^2/s. β is the thermal expansion coefficient and for ideal gas, $\beta = 1/T_f$, where T_f is mean boundary layer temperature, termed the film temperature.

$$\frac{1}{U_{th}} = \frac{t}{k_s} + \frac{1}{h_{conv,air}+h_{rad}} \tag{3-4}$$

$$\mathrm{Nu}_L = \frac{h_{conv,air}L}{k_a} = 0.59 \times Ra_L^{\frac{1}{4}} \tag{3-5}$$

$$\mathrm{Ra}_L = Gr_L Pr = \frac{g\beta(T_{S,2}-T_a)L^3}{\nu\alpha} \tag{3-6}$$

On the relationship with equation (3-5) and (3-6), equation (3-7) is obtained to get the convection heat transfer coefficient between the wall outer surface and the environment. Equation (3-8) represents the radiation heat transfer coefficient, where ε is emissivity of the stainless steel, 0.22 for typical and cleaned stainless steel, and σ is the Stefan-Boltzmann constant, 5.67×10^{-8} $W/m^2\cdot K^4$. $h_{conv,air}$ is calculated as 4.43 W/m^2K and h_{rad} is calculated as

1.45 W/m^{2}K. U_{th} is obtained as 5.87 W/m^{2}K. It is underestimated compared to the experimental value. It is assumed that there is more heat loss from the other parts as well such as the supporters of the SP, steam injection pipe and connecting parts in the experimental device.

$$h_{conv,air} = 0.59 \times \left(\frac{g\beta(T_{s,2}-T_a)}{\nu\alpha L}\right)^{\frac{1}{4}} k_a \quad (3\text{-}7)$$

$$h_{rad} = \epsilon\sigma\left(T_a + T_{s,2}\right)\left(T_a^2 + T_{s,2}^2\right) \quad (3\text{-}8)$$

3.1.3 Partial Pressure Calculation

To decide the pressure of SP, there are three important parameters; Gas Temperature, Gaseous Volume and Number of Moles of non-condensable gas.

The gas temperature is the temperature of the gaseous part in SP. The gas temperature is decided by the temperature of the liquid top in SP, heat loss from SP wall and condensation and boiling on the liquid and gas interface. This experiment is carried out under the boiling point and the effects of condensation and boiling on the liquid and gas interface would be neglected. If the SP is well insulated, the gas temperature would be the same as liquid top temperature and the heat loss from SP would negligible but this stainless steel SP has quite large portion of heat loss compared to the heat input than real SP in light water reactors. Therefore, the heat loss from SP should be considered when analytical models are considered.

Gaseous volume decreases as the water level increases. When the gaseous volume changes, the pressure is highly sensitive according to the ideal gas equation. Initial number of moles of non-condensable gas should be known to calculate the pressure. Since the specific volume is the special property of a material, the amount of material should be figured out initially.

If it is assumed that the gas is only air and the volume is constant, according to the ideal gas law, the pressure is decided by the gas temperature as follows.

$$\frac{P}{T} = \frac{nR}{V}$$
$$\frac{P_1}{T_1} = \frac{P_2}{T_2} \Rightarrow P_2 = P_1 \frac{T_2}{T_1} \quad (3\text{-}9)$$

If it is assumed that the gas is only air and the volume changes, the pressure is decided by the gas temperature and gaseous volume as following equations.

$$\frac{PV}{T} = nR$$
$$\frac{P_1V_1}{T_1} = \frac{P_2V_2}{T_2} \Rightarrow P_2 = P_1 \frac{V_1}{V_2} \frac{T_2}{T_1} \quad (3\text{-}10)$$

By Dalton's law, the pressure of a mixture is sum of the partial pressure of the individual gases. Here, steam and air could be the individual gas and the total pressure is calculated by the sum of the steam pressure and the air pressure as following equations. The pressure of the steam is assumed as the saturation pressure at the temperature. The volume of the air and the one of the steam are assumed as the same as the entire gas volume and the number of moles of the air is assumed to be the same during the experiment. The number of moles of the air is calculated by the ideal gas law and initial conditions as equation (3-18). The pressure of the air is calculated with the ideal gas law, initial conditions and target temperature as equation (3-19). The target pressure is calculated as partial pressure equation as equation (3-20).

$$P_{tot} = P_{air} + P_{steam} \quad (3-11)$$

$$\frac{P_{air}}{P_{tot}} = \frac{n_{air}}{n_{tot}} = \frac{V_{air}}{V_{tot}} \quad (3-12)$$

$$P_{steam1} = P_{steam,sat}(T_1) \quad (3-13)$$

$$P_{steam2} = P_{steam,sat}(T_2) \quad (3-14)$$

$$P_{air1} = P_{tot1} - P_{steam1} \quad (3-15)$$

$$V_{air} = V_{steam} = V \quad (3-16)$$

$$n_{air1} = n_{air2} = n_{air} \quad (3-17)$$

$$P_{air1}V_1 = n_{air}RT_1 \Rightarrow n_{air} = \frac{P_{air1}V_1}{RT_1} \quad (3-18)$$

$$P_{air2}V_2 = n_{air}RT_2$$

$$\Rightarrow P_{air2} = \frac{V_1}{V_2}\frac{T_2}{T_1}P_{air1} \quad (3-19)$$

$$P_{tot2} = P_{steam2} + P_{air2} \quad (3-20)$$

3.1.4 Experimental Results

To investigate the mixing interface when thermal stratification occurs, there are the two different approaches to be attempted; one is from velocity field and the other one is from temperature field. To obtain the velocity field, PIV measurement technique could be used and to obtain the temperature field, LIF measurement technique could be applied. For this research, PIV measurement technique was used to obtain the velocity field around the condensation interface and to study natural circulation by direct contact condensation. It is assumed that the area which has main natural circulation is mixing area and the other area is non-mixing area.

The PIV experiment was carried out with measuring temperature with thermocouples at the same time. The initial temperature of SP water is 23.5°C and the initial pressure of SP is 30.8 kPa. Before the experiment, the air inside the steam generator was blown out to outside by

boiling water and the dissolved air was removed by keeping SP on vacuum condition by the vacuum pump. Fig.3.8 shows the pressure profiles for 30 minute since the steam injection was started. The pressure increased from 30.8 kPa to 34.1 kPa but there is no difference in the condensation regime. The steam mass flux was calculated as 2.81 kg/m^{2}s from the SP water level changes. It is regarded as oscillatory interface regime in Fig.2.1. And the heat input was calculated as 85.4 W using the latent heat.

Fig.3.9 shows the oscillating steam bubble and the shadowgraph. From the shadow graph, the hot plume is shown from the condensation interface upwards. The relatively strong shadow becomes weaker as it goes upward. This shadow is shown due to the different reflective index according to the different density. Therefore, from the figure it is supposed that the hot condensate which is generated from the condensation interface flows upward being oscillated by oscillatory interface and mixes with ambient fluid and its temperature becomes similar to the ambient fluid.

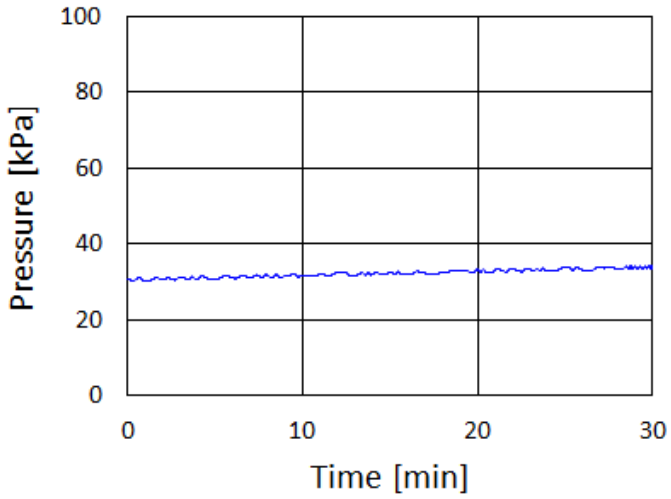

Fig.3.8 Pressure transient

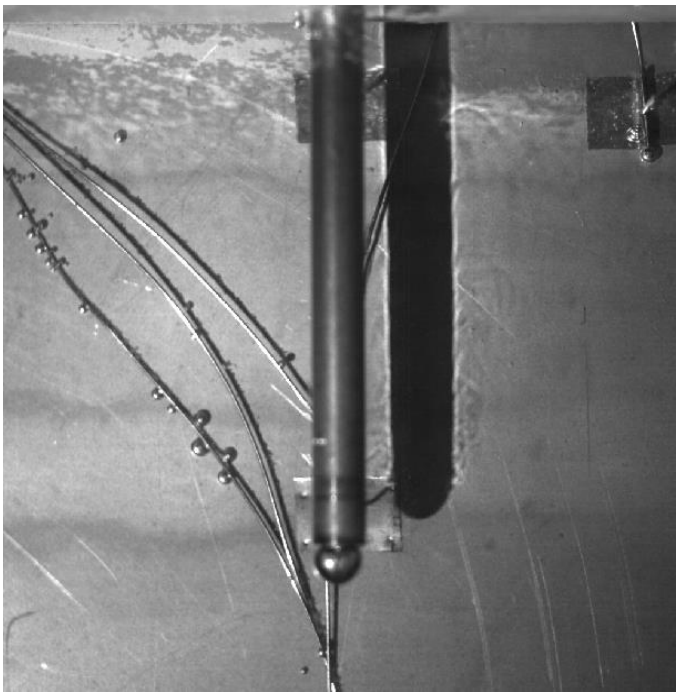

Fig.3.9 The steam bubble and the shadowgraph

3.1.4.1 Thermal Stratification (On the Liquid Center)

Fig.3.10 shows the temperature transient on the center line in the horizontal axis. Thermal stratification is shown as the temperature in the higher level is higher than the temperature in the lower level. The point 2-6 shows the highest temperature and the point 2-1 shows the lowest one. For the first 12 minutes, the temperatures of the points 2-1, 2-2 and 2-3 do not change but the ones of the points 2-4, 2-5 and 2-6 change from the beginning. It is assumed that the mixing interface exists between the two groups from the profiles.

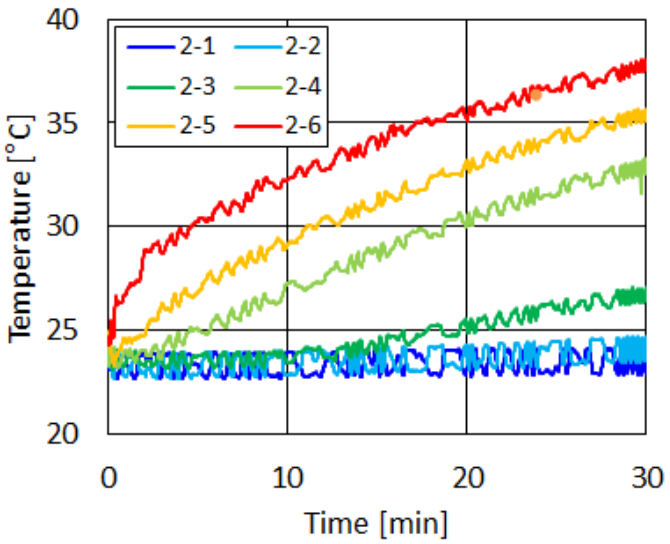

Fig.3.10 Temperature transient of liquid (On the center)

3.1.4.2 Heat Accumulation (On the Liquid Top)

The temperatures at the highest levels were measured to check the heat accumulation as Fig.3.11. Fig.3.11 (a) shows the temperature profiles at the points of 1-6, 2-6, 3-6, 4-6 and 5-6. Fig.3.11 (b) shows the temperature profiles without the closest one. The closest one to the steam injection pipe, 5-6, has not only the highest peaks but also lowest peaks. It is regarded that the complicated mixing occurs around the steam injection pipe since the unstable hot water plume flows upward from the condensation interface. The oscillation from the condensation interface transfers the instability to the area around the pipe. It is shown in the Fig.3.11 (b) that as the point is apart more, the temperature decrease. The temperature of the point 1-6 is the lowest and the one of the point 4-6 the highest. Around 4° is different at the two points which are 53D apart, where D is the outer diameter of the pipe.

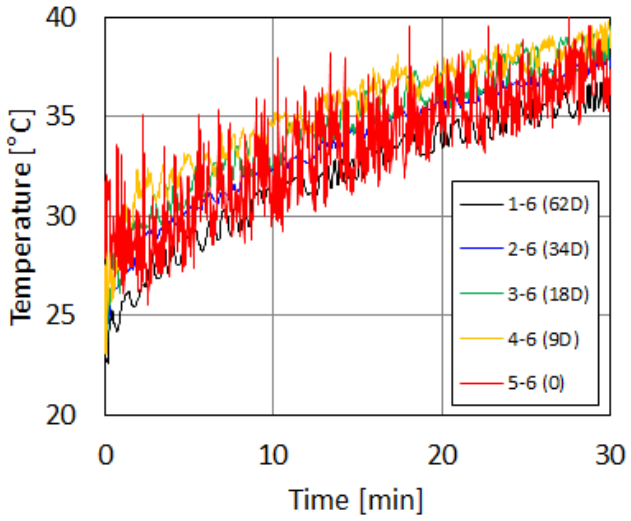

(a) At all the points on the liquid top

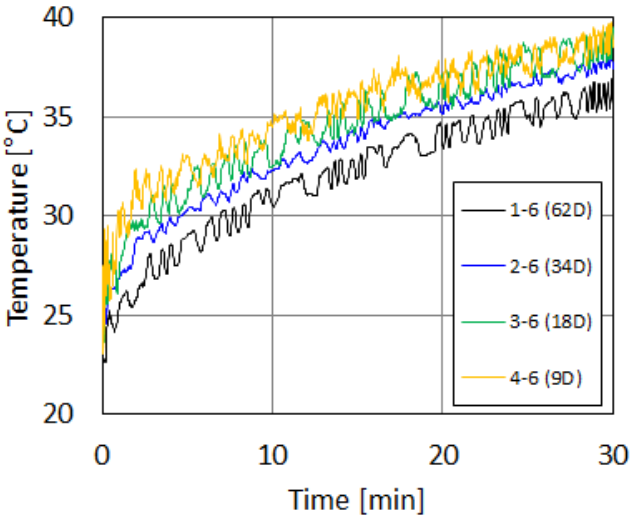

(b) At the points without 5-6

Fig.3.11 Temperature transient of liquid (On the top)

3.1.4.3 Temperature Fluctuation on the Liquid Top

As shown in the Fig.3.11, the degrees of the fluctuations are quite different at the different points. Fig.3.12 shows the standard deviation for 1 minute according to the time at the points. As expected, the standard deviation of the closest point is the largest. However, the lowest is

not at the furthermost point. The lowest one is shown in the center point, 34D, from the pipe to left end. It is assumed that the area on the horizontal center line is the most stable area and the farthest area has instability because there is natural circulation and the hot water from the top mixes with the relatively cold water. In process of time, overall standard deviations decrease and it is assumed that as subcooling decreases, the condensation interface gets stable.

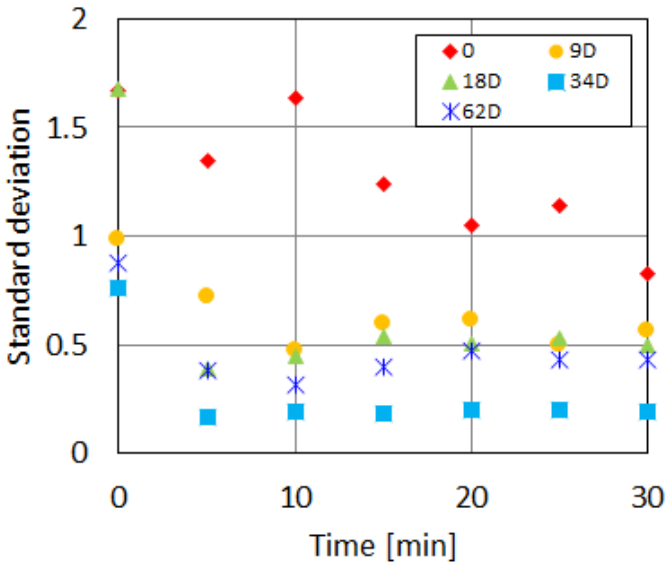

Fig.3.12 Standard deviation on the liquid top

3.1.4.4 Velocity Fields around the Steam Pipe (PIV)

Fig.3.13 shows the velocity fields at the time of 10, 20 and 30 minutes after steam injection start, where D is steam injection pipe inner diameter. The dotted line in the figure shows the steam injection pipe position. Although the images were obtained at the frame rate of 500, these figures were acquired at the frame rate of 50, which was judged to be proper to get the upward flow by buoyancy since average particle displacement of about 8 pixels is regarded to be ideal. The strong upward flow is shown around the steam injection pipe and it induces the

anticlockwise natural circulation on the left side. Because of the natural circulation on the left side the upward flows tend to be tilted rightward.

Due to the fluctuating condensation interface, this buoyancy driven upward flow has large instability. Since the high temperature condensate mixes with ambient fluid quickly with high instability, flow shows strong turbulence from the condensation interface to the top of the pool and the maximum velocity magnitude and the area change irregularly over time.

Fig.3.14 represents the selected lines for velocity profiles and Fig.3.15 shows the velocity profiles on the selected lines at 30 minutes after steam injection start. The profile on the A-A' line shows the u component. It is shown that the natural circulation occurred having the leftward flow near the water top with the maximum velocity of -4.6 mm/s and the rightward flow under the leftward flow with the maximum velocity of 3.0 mm/s. The profile on the B-B' line shows the velocity magnitude. Due to high instability, the profile shows large fluctuation. From the condensation interface to the water top, the velocity increases slowly in the beginning but as the instability gets higher from the pipe tip, the velocity profile fluctuates. The velocity magnitude of hot plume of condensate ranges from 13 to 32 mm/s. The profile on the C-C' line shows the v component. It demonstrates Gaussian distribution which moved around 0.5D to the right due to natural convection on the left.

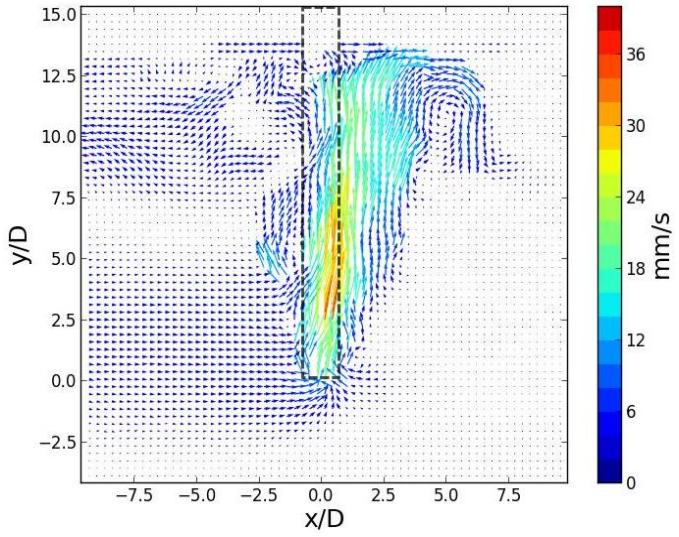

(a) 10 min. after steam injection start

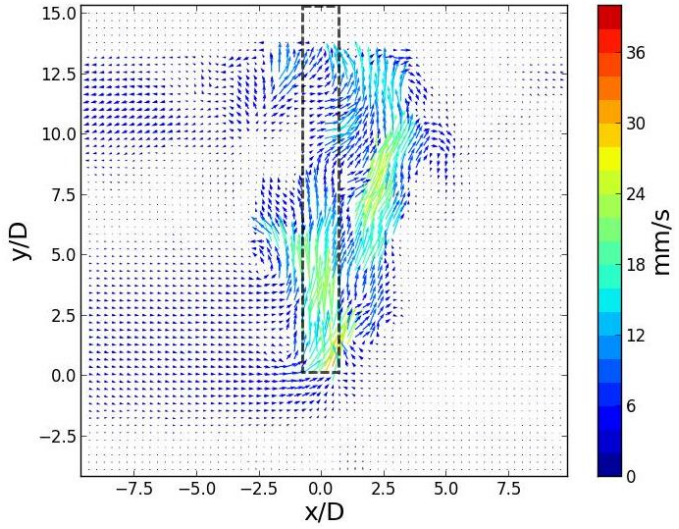

(b) 20 min. after steam injection start

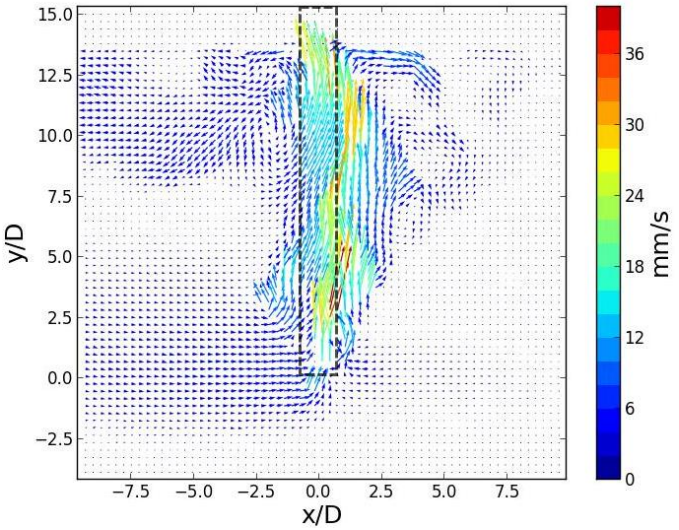

(c) 30 min. after steam injection start

Fig.3.13 Velocity fields around the steam injection pipe

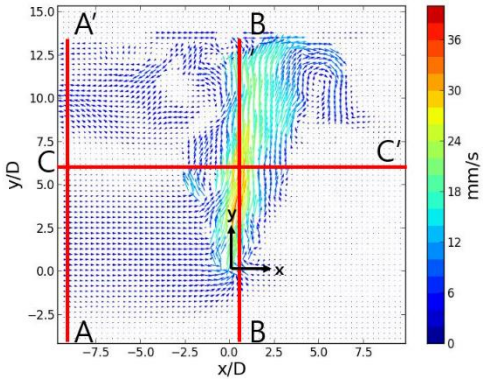

Fig.3.14 Selected lines for velocity profiles

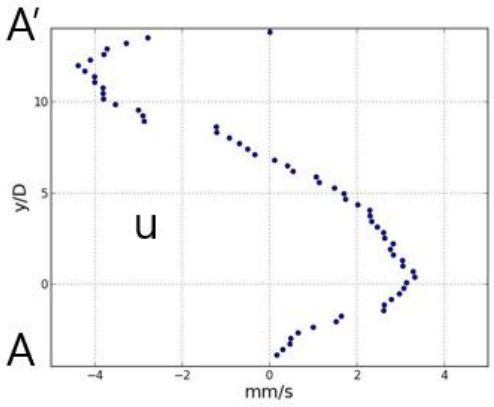

(a) On the line of A-A’

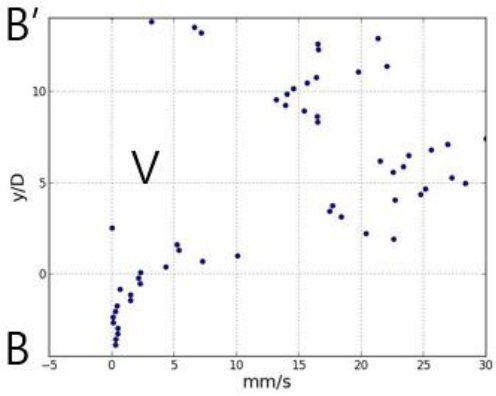

(b) On the line of B-B’

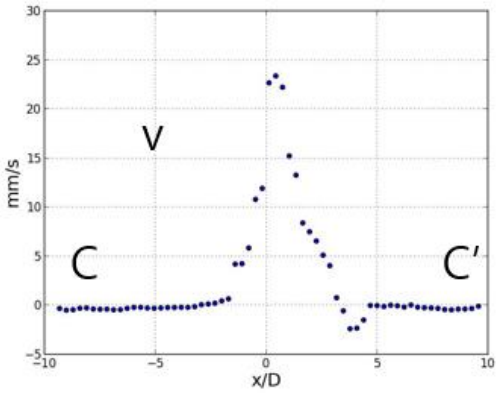

(c) On the line of C-C’

Fig.3.15 Velocity profiles on the selected lines (A, B and C)
at 30 min. after steam injection start

Fig.3.16 shows the velocity fields near condensation interface and represents the oscillation. Those fields are obtained at the cross correlation time step of 2ms. Those demonstrate the oscillating in and out motion. This oscillation generates momentum around the area and affects the mixing interface. The dotted line in figure shows the steam injection pipe position.

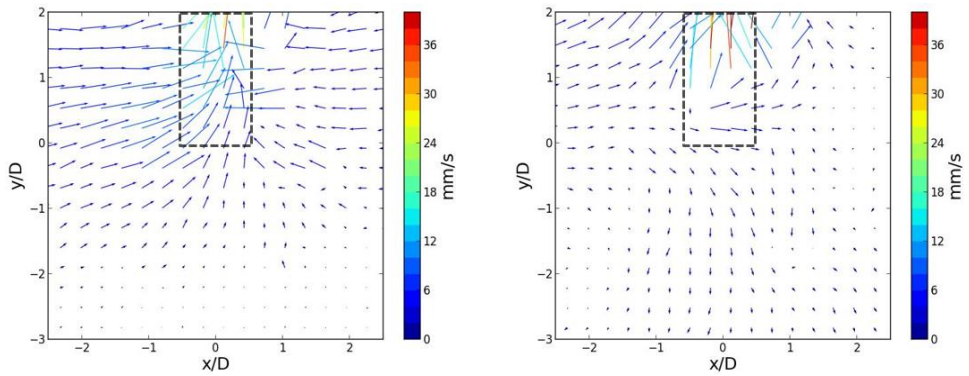

(a) Oscillating in (b) Oscillating out

Fig.3.16 Velocity fluctuation near the condensation interface

3.1.4.5 Mixing Interface

From the velocity profile, the level of which u component is 0 under natural convection area could be regarded as mixing interface. From the profile on the line of A-A', the vertical position of -4.7D (20mm under the pipe tip) is turned out to be the mixing interface for this regime.

3.1.4.6 Gas Temperature and Pressure and Partial Pressure Calculation

Fig.3.17 shows steam temperature inside the steam injection pipe, T_{st}, steam saturation temperature at the SP pressure, T_{sat}, water subcooling, T_{sub}, temperature of gaseous area inside SP, T_g. T_{sat} and T_{sub} are almost same so that the generated steam can be regarded as saturated steam. T_{sub} was started from 45 and ended at 38. This range is small so it is assumed that the condensation regime does not change.

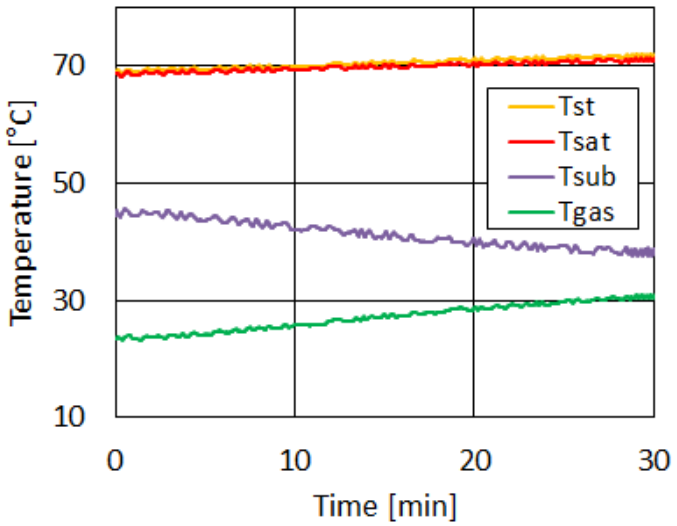

Fig.3.17 Steam temperature and subcooling

Based on the partial pressure equation as I stated above, pressure was calculated and compared with the measurement value. SP initial pressure, temperature transient of gaseous area and volume transient were used to calculate the SP pressure. Volume transient was assumed from SP water level. Fig.3.18 demonstrates the comparison of experimental value and calculated value. Calculated value shows good agreement with experimental value. So it is assumed that the pressure could be calculated when we know the temperature of the gaseous are and the gaseous volume. If the system is regarded as insulated system, the temperature of the gaseous area would be the same as the average temperature of water top area by heat balance. Therefore, in an insulated SP, the pressure could be calculated with the average temperature of water top area and SP water level.

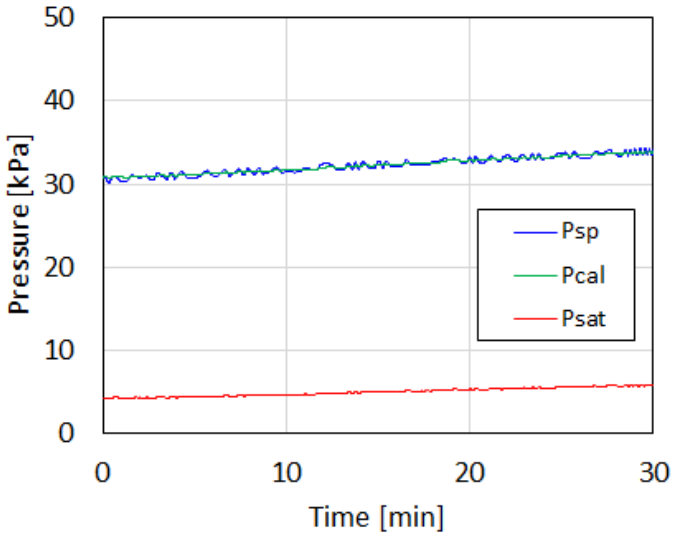

Fig.3.18 Validation of pressure

3.1.5 Discussion and Summary (Buoyancy, Natural Convection, Mixing Interface and Pressure Suppression)

This phenomenon is summarized as pressure increase due to the thermal stratification by direct contact condensation in suppression pool. It includes heat transfer, fluid dynamics and thermodynamics. The condensate from condensation interface has buoyancy to lead natural convection and the momentum depending on the condensation regime and mass flux decides the mixing interface. According to the mixing interface and momentum, the temperature field is determined and pressure suppression capacity is decided.

3.1.5.1 Condensation Interface, Fluctuation, Temperature, and Buoyancy

By direct contact condensation, the latent heat and sensible heat are transferred to ambient fluid. The fluctuation from condensation interface generates momentum and mixes hot condensate with ambient fluid. The hot water plume induces upward flow by buoyancy due to the density difference. Subcooling is related to not only the condensation regime but also buoyancy due to density difference of condensate and ambient fluid. Buoyancy is getting weaker as subcooling decreases and momentum from oscillating condensation interface is

getting stronger than buoyancy relatively. The momentum from the condensation interface and buoyancy determine the characteristics of the mixing area.

3.1.5.2 Mixing Interface and Cooling Capacity

When thermal stratification takes place inside SP, the cooling capacity is shorten radically. If the thermal conduction, radiation and diffusion are neglected, the only way to transfer heat is convection. It could be forced convection, natural convection and mixed convection. If the momentum is strong, that would be forced or mixed convection. If the momentum is weak, only natural convection would be considered. Therefore, the amount of momentum should be carefully investigated according to the different DCC regimes. And the position of mixing interface should be measured at the different DCC regimes. It could decide the cooling capacity of the suppression chamber. These data could be used for engineers to design the suppression chamber and to validate CFD codes.

3.1.5.3 Mixing Interface number and Pressure Suppression Capacity Ratio

To define the effects to SP by stratification, mixing interface number (MI) and pressure suppression capacity ratio (PSCR) are introduced. Mixing interface number is the ratio of the vertical length of mixing area divided by whole vertical length as shown in equation (3-20). This mixing interface number would be affected by the vertical position that the condensation happens and the momentum from condensation interface.

Pressure suppression capacity ratio is the ratio of acceptable heat in stratified system divided by the heat that whole water can accept as shown in equation (3-21). Since the pressure would radically increase when the steam is not condensed and steam is condensed at the condition under saturation temperature, the amount of pressure suppression would be decided by the amount of the acceptable heat until evaporation. However, finally it is decided by the ratio of the mixing area mass and whole water mass. And if the volume is rectangular, PSCR is the same as MI. In real suppression pool of light water reactors, the shape is not rectangular so those are not the same.

$$MI = \frac{H_m}{H} \tag{3-20}$$

$$\mathrm{PSCR} = \frac{C_v m_m \Delta T}{C_v m \Delta T} = \frac{m_m}{m} \tag{3-21}$$

These numbers are not the same even in the same SP. It depends on the DCC regimes as well. Therefore, these numbers should be known according to the type of SP and DCC regimes to define the exact cooling capacity. In this experiment, the mixing interface could be detected by A-A' velocity profile in Fig. 13 when u component is close to 0 under the mixing area. MI and PSCR are calculated as 0.36. Only 36% of the water are used to suppress the pressure in SP.

Thermal stratification by DCC was studied experimentally. To investigate the mechanism of thermal stratification, natural convection was visualized and quantified. Velocity fields were obtained by PIV technique and the analysis were carried out at the two different time steps, one for overall velocity field and the other one for the oscillating area around the condensation interface. Mixing interface number and pressure suppression capacity ratio are introduced to evaluate the cooling capacity of SP.

3.2 Numerical Simulation

3.2.1 Numerical Setup

The ANSYS CFX is a general-purpose CFD package capable of solving diverse and complex three-dimensional fluid flow problems. ANSYS CFX uses the Navier-Stokes equations to describe the fundamental processes of momentum, heat, and mass transfer. The basic procedure in modeling Thermal Stratification with ANSYS CFX consists of five steps-creating the geometry, meshing, pre-processing, solving, and post-processing.

ANSYS CFX is the CFD codes developed from CFX-4 and CFX-TASCFlow. The earlier analysis technique and the workbench is combined and it became a convenient CFD tool for users to work on GUI (Graphical User Interface) and serves fast and quite accurate analysis results. All the analysis processes, from CAD to post-processing, of CFX are progressed on the ANSYS workbench environment.

Numerical simulation of thermal stratification was carried out on single phase with ANSYS CFX 14.0. Since the steam condensation finishes around the exit of the steam pipe and only heat was transferred to water, wall heat flux and volumetric heat source was considered around the exit of the submerged steam pipe. Because the liquid free surface temperature does not increase over than the saturation temperature at the pressure of the pool, the evaporation and condensation at the interface of the top of the liquid and the bottom of the gas could be neglected. Therefore, single phase calculation was carried out.

ANSYS CFX uses conservative finite-element-based control volume method. A coupled solver, which solves the hydrodynamic equations (for u, v, w, p) as a single system, is used. A fully implicit discretization of the equations is used in this solution approach at any given time step. Implicit and pressure-based algorithm is used for all flow speeds and regardless of compressibility. ANSYS CFX uses a Multigrid (MG) accelerated Incomplete Lower Upper (ILU) factorization technique for solving the discrete system of linearized equations. Since it is an iterative solver, the exact solution of the equations is approached during the course of several iterations [41].

Unsteady Navier-Stokes equations are solved in ANSYS CFX in their conservation form. Equation (3-22), (3-23) and (3-24) are the instantaneous equations of mass, momentum and energy conservation. For the energy equation, total energy equation was selected as in the equation (3-25) and h_{tot} is total enthalpy, which is related to the static enthalpy h(T,p) as h_{tot} = h + $U^2/2$. The term $\nabla \cdot (\lambda \nabla T)$ demonstrates the work by viscous stresses. This term presents the internal heating by viscosity in the fluid but is negligible in most flows and this case. The term $U \cdot S_M$ represents the external momentum source. S_E is the volumetric heat source.

$$\frac{\partial p}{\partial t} + \nabla \cdot (\rho\, U) = 0 \tag{3-22}$$

$$\frac{\partial (\rho\, U)}{\partial t} + \nabla \cdot (\rho\, U \otimes U) = -\nabla p + \nabla \cdot \tau + S_M \tag{3-23}$$

$$\tau = \mu \left(\nabla U + (\nabla U)^T - \frac{2}{3} \delta \nabla \cdot U \right) \tag{3-24}$$

$$\frac{\partial (\rho\, h_{tot})}{\partial t} - \frac{\partial p}{\partial t} + \nabla \cdot (\rho\, U\, h_{tot}) = \nabla \cdot (\lambda \nabla T) + \nabla \cdot (U \cdot \tau) + U \cdot S_M + S_E \tag{3-25}$$

A source term is added to the momentum equations for buoyancy calculations as equation (3-26). The density difference $\rho - \rho_{ref}$ is evaluated using either the full buoyancy model or the Boussinesq model according to the physics. The full buoyancy model is used if the fluid density changes with temperature or pressure, which is expected for all ideal gases and real fluids. The Boussinesq model is used if the fluid density is constant, not a function of temperature or pressure.

$$S_{M,buoy} = (\rho - \rho_{ref})\, g \tag{3-26}$$

A momentum source is implemented in ANSYS CFX as a force per unit volume acting on the fluid. General momentum source is selected in cylindrical coordinate. Equation (3-27), (3-28) and (3-29) represents the momentums in the direction of radial, axial and theta components.

$$S_{M,R} = S_{spec,R} r \tag{3-27}$$

$$S_{M,\theta} = S_{spec,\theta}\varphi \tag{3-28}$$

$$S_{M,Z} = S_{spec,Z}z \tag{3-29}$$

No-slip velocity boundary condition is applied to the pipe and the wall as shown in equation (3-30) except top area and bubble. On top area, free-slip condition was applied as shown in equation (3-31) and (3-32). On the pipe, adiabatic condition was applied as equation (3-33) and convection surface condition, which is obtained from the surface energy balance, was applied to the wall considering heat loss as equation (3-34). The overall heat transfer coefficient, 6.37 W/m^{2}K, was calculated by SP cooling test and applied to the wall boundary. Heat input, 85.4 W, is applied to the heat source volume or bubble surface. The heat input was calculated by water level changes. For heat flux model, finite heat flux was applied to the bubble surface as equation (3-35).

$$U_{Wall} = 0 \tag{3-30}$$

$$U_{n,Wall} = 0 \tag{3-31}$$

$$\tau_w = 0 \tag{3-32}$$

$$\left.\frac{\partial T}{\partial x}\right|_{x=0} = 0 \tag{3-33}$$

$$-\mathrm{k}\left.\frac{\partial T}{\partial x}\right|_{x=0} = h[T_\infty - T(0,t)] \tag{3-34}$$

$$-\mathrm{k}\left.\frac{\partial T}{\partial x}\right|_{x=0} = \ddot{q}_s \tag{3-35}$$

Calculation was done on laminar mode because there is no forced convection, no large turbulence compared to the size of SP and the most conservative calculation about thermal stratification is on laminar. Natural and mixed convection flows can be modeled by CFX with buoyancy source terms. Natural convection flows can be modeled by CFX with buoyancy source terms.

Physical time duration is 30 min and time step is 0.2 s. The initial temperature is the same initial temperature with the experiment, 23.5°C. Applied advection scheme is upwind and 2nd order central differencing hybrid scheme and the transient scheme is 2nd order backward Euler scheme. The mesh was generated by the commercial meshing tool, ICEM CFD. Mesh type is tetra and mixed mesh. The number of total nodes which are calculated is 78613.

Fig.3.19 shows the overview of the Downsized 2D Suppression Pool model. This model is three dimensional. The volume was separated into two parts, the volume around condensation interface for heat source and the entire volume. The volume for the source is selected as subdomain and heat source could be applied to the subdomain. The summary of the numerical simulation conditions is demonstrated in Table.1.

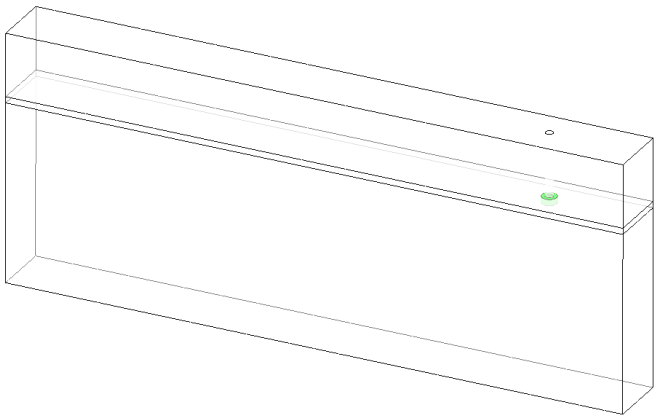

Fig.3.19 The overview of SP model

Table.1 The specification of conditions for 2D SP model

Turbulence	None (Laminar)
Heat transfer	Total energy model
Buoyancy	Full buoyancy model
Heat input	85.4W
Physical time duration	30 minutes
Advection scheme	Upwind and 2nd order central differencing hybrid scheme
Transient scheme	2nd order backward Euler scheme

3.2.1.1 Wall Heat Flux Model (M1)

Fig.3.20 shows the mesh around the steam pipe, the position to which wall heat flux was applied of the SP model. Considering the oscillating condensation interface, the heat flux wall was modelled larger than the steam injection pipe diameter. The heat input is 85.4 W and the heat flux is calculated as 482 kW/m^2. In this model, the momentum is neglected and only the heat from latent heat is considered. The buoyancy induced from the water density difference by transferred heat from wall heat flux is only the driving force for this model.

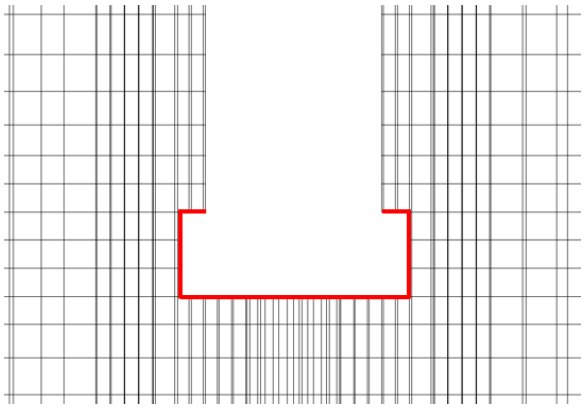

Fig.3.20 Wall heat flux model

3.2.1.2 Volumetric Heat Source Model (M2)

Fig.3.21 represents the heat source volume around the condensation interface. It could consider the mixed area around oscillating condensation interface. The heat input is 85.4 W and the volume of the subdomain for the heat source is 3.67×10^{-7} m^3. The heat source is calculated as 233 MW/ m^2. In this model, the momentum is neglected and only the heat from latent heat is considered in the subdomain. The buoyancy induced from the water density difference by transferred heat from heat source is only the driving force for this model.

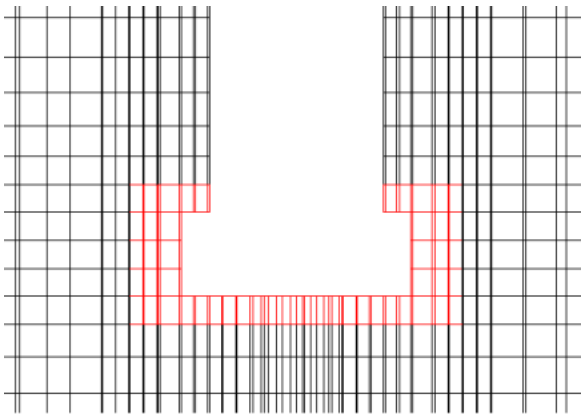

Fig.3.21 The subdomain for volumetric heat source

3.2.2 Results

Numerical simulations were carried out with two models and the results are shown in Fig.3.22 and Fig.3.23. Fig. 3.21 shows the temperature fields and fig. 3.22 shows the temperature profiles at the time of 30 minutes. In the temperature fields, the thermal stratifications and mixing interfaces are shown clearly. The wall flux model (M1) shows the plume of highest temperature around the steam injection pipe and the volumetric heat source model (M2) is the second. M1 shows the plume of higher mixing interface than M2.

Temperature profiles are obtained at the positions of fig.3.3. The profiles show clear thermal stratification and the similar trends are shown in the models. Thermally stratified region exists

in the mixing area and the temperature distribution is large compared to non-mixing area and the temperature does not change in non-mixing area. However, the temperature was overestimated than experiment as the maximum temperature is much larger than experimental result and the temperature range in mixing area is much wider than experiment. M1 shows higher maximum temperature and wider distribution than M2 in mixing area.

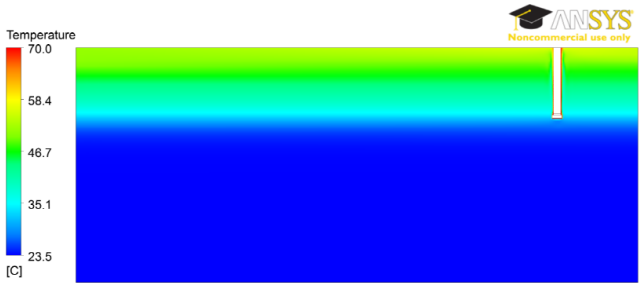

(a) Wall heat flux model

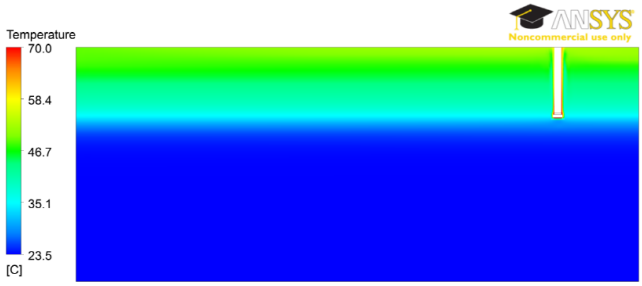

(b) Volumetric heat source model

Fig.3.22 Temperature fields according to different models

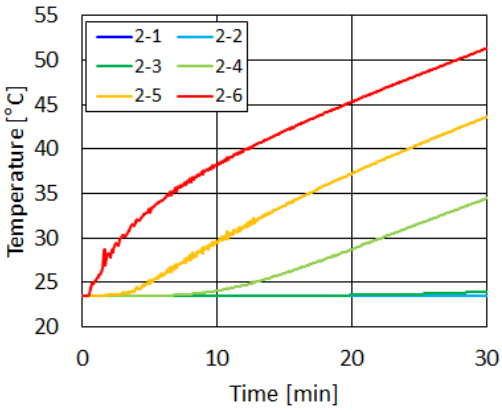

(a) Wall heat flux model

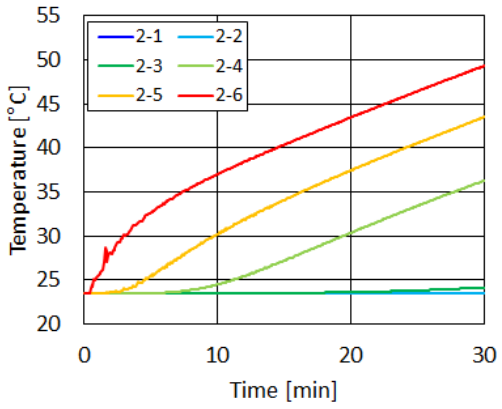

(b) Volumetric heat source model

Fig.3.23 Temperature profiles according to different models

Fig.3.24 shows the velocity fields at the time of 30 minutes. The plane was chosen at the location with experiment. The upward flow by buoyancy is clearly represented on the velocity fields in both cases. The velocity of M2 is higher than the one of M1. The trends of two cases are quite similar but the width of hot plume of M2 is wider than the one of M1 . Fig.3.25 shows the profiles at the selected line as shown in Fig.3.14. It is shown that the velocity of M2 is higher than the one of M1 at all the lines. Especially, at the line of B-B', the velocity of M1 is almost two times of the one of M2. The velocity profiles at the line of A-A' seem to be quite

different from experimental data. Since the natural circulation is weak, the secondary flows are shown inside the main natural circulation. The instability is not shown in numerical simulation because this simulation on laminar mode and there is no momentum.

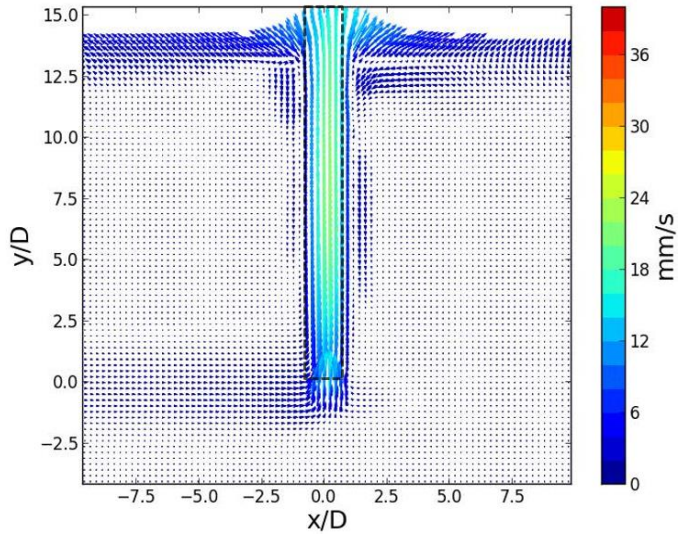

(a) Heat flux model (M1)

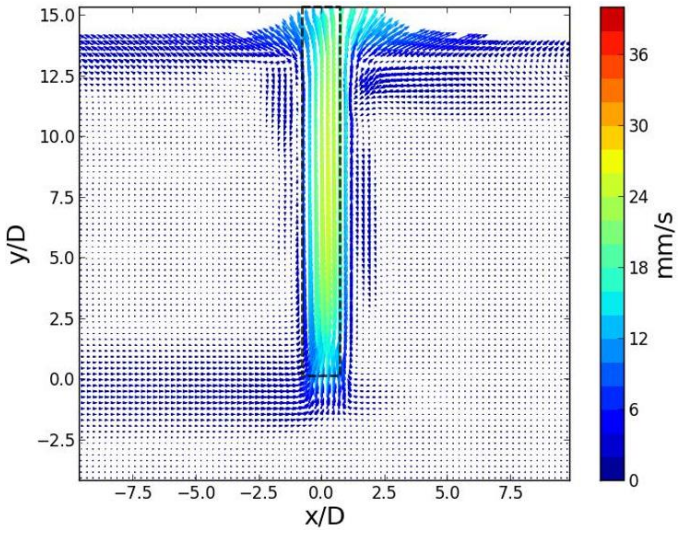

(b) Heat source model (M2)

Fig.3.24 Velocity fields at the time of 30 minutes

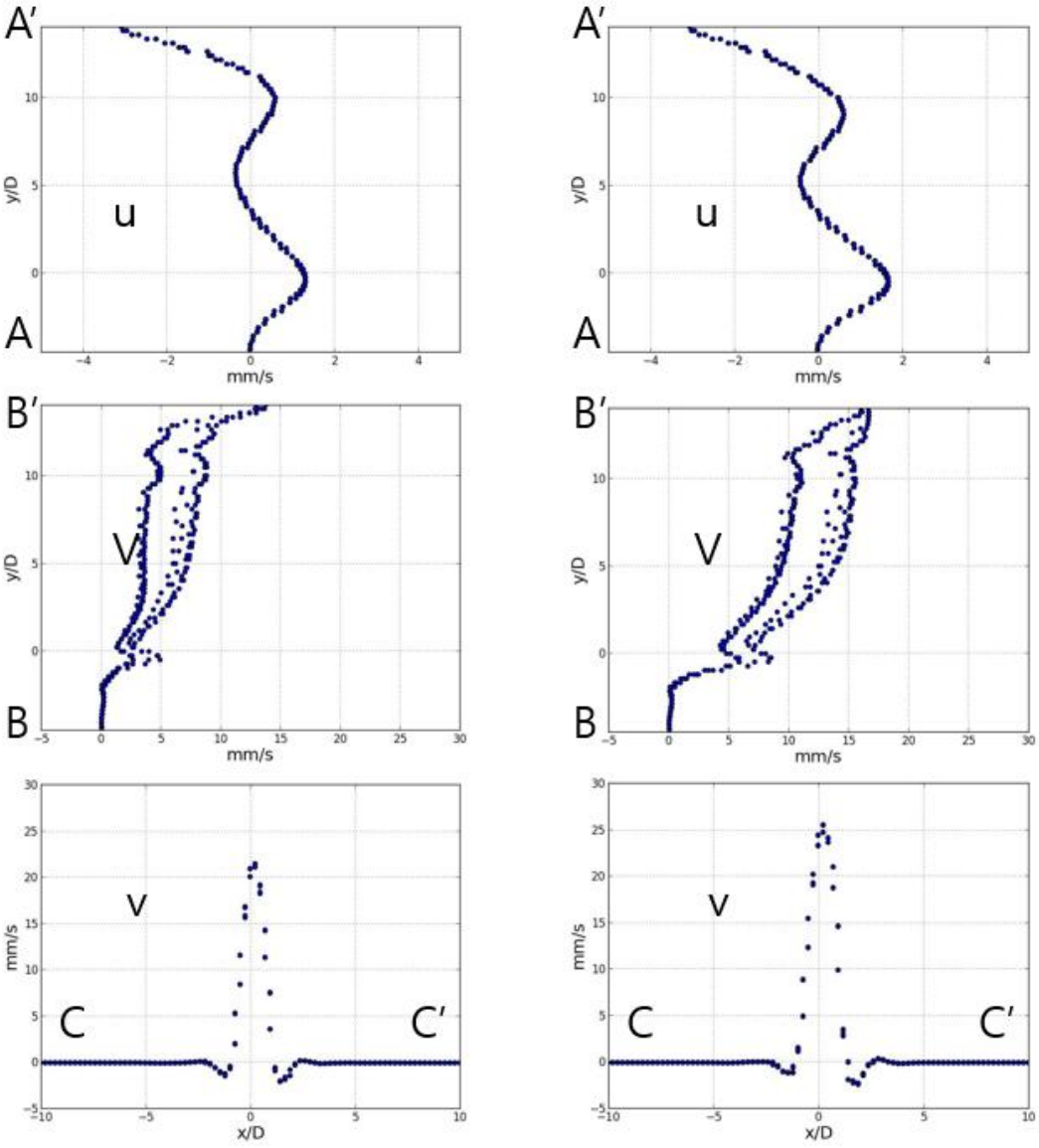

(a) Heat flux model (M1) (b) Heat source model (M2)

Fig.3.25 Velocity profiles at the time of 30 minutes

3.2.3 Discussion and Summary

It is assumed that the temperature distribution in mixing area is most important because it is related to the natural circulation which is one of the important mechanism about thermal stratification and the temperature of non-mixing area does not change much. Therefore, one of the validation points could be the temperature difference between channel 2-4 and 2-6. From experiment, the temperature difference is 4.9°C and it is almost kept during the experiment. At numerical simulations, the temperature differences are much larger, 16.9°C at M1 and 13.0°C at M2. Another validation point in temperature distribution could be the temperature of channel 2-6 since the temperature of water top is important because that is related to the temperature of gaseous area in SP and the pressure of SP. The temperature of channel 2-6 at the time of 30 minutes is 37.6°C but in numerical simulations it is much higher as shown in Fig.3.23.

From the velocity data, it is demonstrated that the natural circulation by buoyancy is weaker than experiment. It would cause problem to predict the mixing interface exactly. And the instability from the condensation interface could not be shown in numerical simulation. After condensation, the temperature of condensate is assumed to be the saturation temperature. The temperature of the hot plume by buoyancy should not be over than the saturation temperature. Since the maximum temperature is over than the saturation temperature around the wall surface to which the heat flux is applied and the heat source volume, M1 and M2 are not suitable to simulate thermal stratification. Because the momentum strongly affects the characteristic of temperature distribution of SP, it is suggested that not only heat input but also momentum be considered for this simulation.

CHAPTER 4 MOMENTUM MODEL FOR DIRECT CONTACT CONDENSATION

4.1 Background

In the Torus system, almost everywhere is single phase. Only the steam nozzle area (direct condensation) and free surface (phase change) should be considered in two-phase flow model. In this study, the single-phase numerical simulation code was applied to evaluate the thermal stratification. However, as discussed in Section 3.2, the single phase code cannot simulate the thermal stratification, because it does input the momentum. Not only the heat input, but momentum input should be taken into account into the single-phase numerical simulation model. In this section, the momentum model for the CFD simulation code will be empirically obtained using the experimental results and applied the CFD code to validate the model. Comparing with the two-phase flow CFD code, the simulation cost and the accuracy may be reduced dramatically.

4.2 Momentum Model

As the momentum is regarded as one of the critical factors to decide the mixing interface, the momentum which affects the thermal stratification is needed to be calculated. The momenturm rate is calculated as dmυ/dt and this momentum could be investigated in the radial direction and axial direction. Fig.4.1 shows the images of oscillating steam bubble. These images were obtained by the high speed camera at the frame rate of 500. The average frequency of this oscillation is 40 Hz. The motions of oscillaing in and out are based on the vertical motion but the horizontal motion is the opposite. Momentum rate is calculated with the mass flow rate and the velocity. To calculate the momentum experimentally, two appraoches were tried; velocity magnitude approach and corresponding velocity approach.

Firstly, the velocity magnitude approach is tried. Fig.4.2 shows the slectected lines for velocity profiles to investigate the momentum around the condensation interface. The velocity profiles are shown in Fig.4.3. Fig.4.3 (a) and (c) shows the velocity profiles when oscillaing in and (b) and

(d) shows the ones when oscillaing out as shown in Fig.4.1. Fig.4.3 (a) and (b) represents the v components on the line of D-D' and (c) and (d) represents the u components on the line of E-E'.

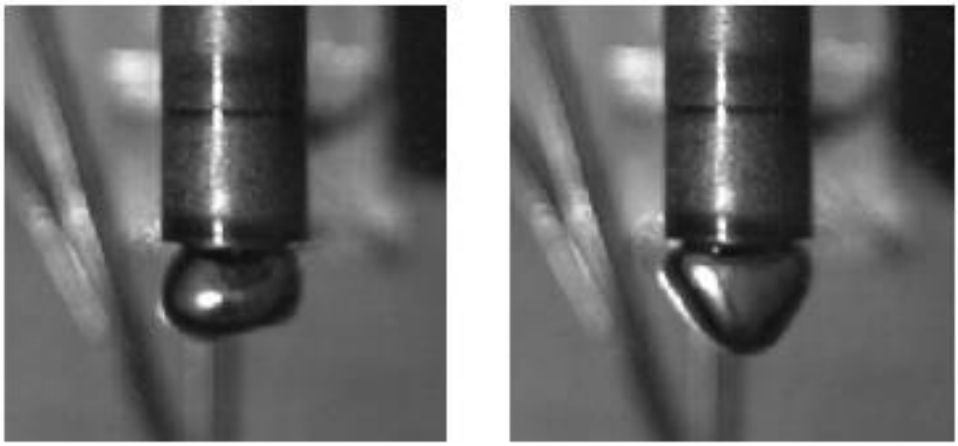

(a) Oscillating in (b) Oscillating out

Fig.4.1 Oscillating steam bubble

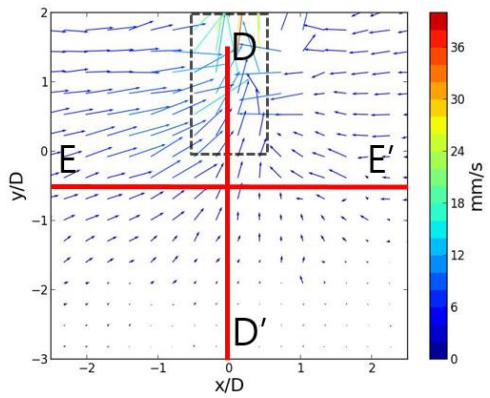

Fig.4.2 Selected lines for velocity profiles (Near condensation interface)

When oscillaing in, the v components on the line of D are over than 0 and the u components on the line of E have relatively large absolute values. However, when oscillaing out, the v components on the line of D have negative values under the pipe tip and increase quickly along the pipe over the pipe tip. The u components on the line of E have relatively small absolute

values compared to the oscillating in motion. When oscillaing in, the u component has wider distribution and when oscillaing out, the v component has wider distribution.

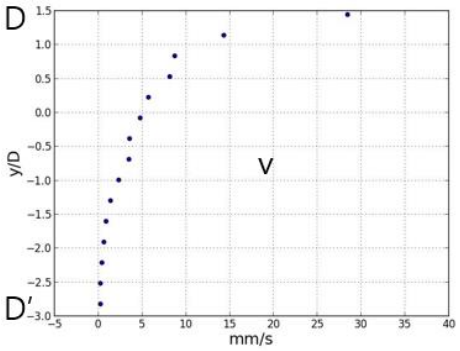

(a) Ocillating in (D-D’)

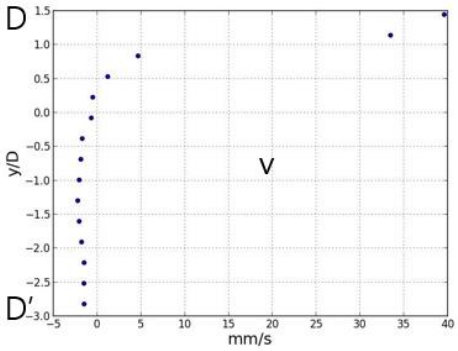

(b) Ocillating out (D-D’)

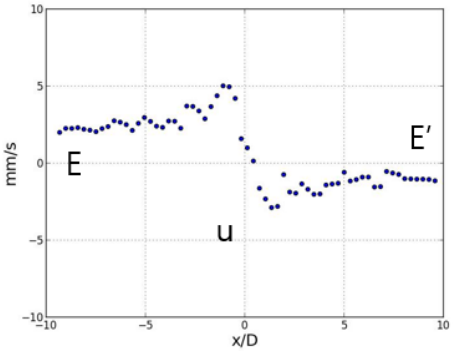

(c) Ocillating in (E-E’)

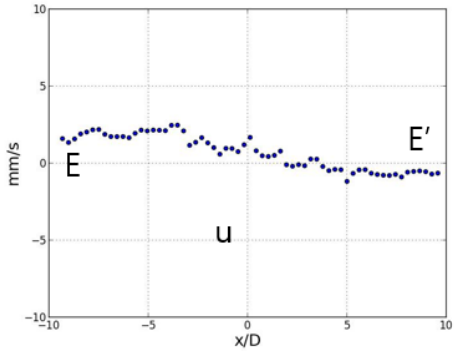

(b) Ocillating out (E-E’)

Fig.4.3 Velocity profiles on the selected lines (D and E)
at 30 min. after steam injection start

The radial momentum rate was caculated by the maximum u component and the steam mass flow rate and the axial momentum rate was calculated by the maximum negative v component and the steam mass flow rate as shown in the equation (4-1), where the density is the property of the saturated condensate. Since the negative v component affects the mixing interface, only negative value of v component was considered for the axial momentum as shown in the Fig.4.3.

The steam mass flow rate is 3.53×10^{-5} kg/s. In axial direction, since there are not only the force by momentum but also the buoyancy, it is difficult to assume the maximum velocity which is not affected by buoyancy. Therefore, the radical maximum velocity is used for calculating momemtum and is used as axial maximum velocity as well. The radial maximum velocity at the time of 5 min is 2.1 mm/s. The radial and axial momentum rate is calculated as 7.41×10^{-8} C_{DCC} kg·m/s2.

$$\dot{p} = C_{DCC}\dot{m}v_{max} \tag{4-1}$$

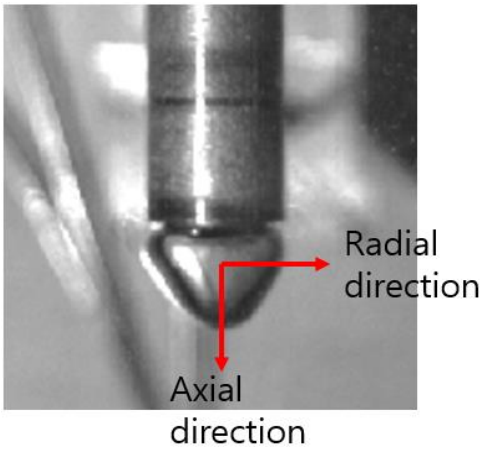

Fig.4.4 The direction of momentum rate

Secondly, the corresponding velocity approach is investigated. The oscillation makes large instability at near-field of condensation interface but it makes relatively stable flow at far-field. The corresponding velocity at far-field could be used to obtain momentum. The corresponding velocity is calculated as $\sqrt{2}\delta f$ as reference [21]. In this approach, the momentum rate is calculated with mass flow rate, $\dot{m}$, bubble oscillating distance, δ, and the bubble frequency, f, as shown in equation (4-2). The bubble amplitude, δ, is obtained from fig.4.1 as 1mm. It is

estimated as the vertical difference of bubble boundary between oscillating in motion and oscillating out motion. The oscillating frequency, f, is obtained from bubble motion as 40 Hz. C_{DCC} is the constant according to the different DCC regime. The radial and axial momentum rate is calculated as $\sqrt{2}\times10^{-6}$ C_{DCC} kg·m/s^2.

$$\dot{p} = C_{DCC}\sqrt{2}\dot{m}\delta f \text{ [kg m/s²]} \quad (4\text{-}2)$$

The two approach shows large difference. Since velocity is affected by not only the momentum but also the buoyancy, it is difficult to consider the velocity to be only from momentum. Therefore, the second approach is seemed to be more appropriate. Because the mometum is induced from the bubble oscillation, corresponding velocity approach is used to calculate momentum experimentally and the constant, C_{DCC} is obtained from the comparison of experiment and numerical simulation.

Two additional numerical models are introduced; wall heat flux and volumetric momentum source model (M3) and volumetric heat and momentum source model (M4). To the heat flux model (M1) and the heat source model (M2), momentum source is added to the subdomain which heat source is applied to.

4.2.1 Wall Heat Flux and Volumetric Momentum Source Model (M3)

The heat input is 85.4 W and the heat flux is calculated as 482 kW/m^2. In this model, the momentum from the oscillating condensation interface and the heat from latent heat are considered. Momentum rate was applied to the subdomain but the heat model is wall heat flux model. The momentum was calculated from the acceleration around the condensation interface and the density at saturation. The buoyancy induced from the water density difference by transferred heat from wall heat flux is the main driving force and the momentum in subdomain affects the flow for this model. It is assumed that the heat is dispersed by momentum.

4.2.2 Volumetric Heat and Momentum Source Model (M4)

Volumetric Heat and Momentum Source Model is the model which the heat and the momentum are applied to the volume of the subdomain. Heat source and momentum source are applied to the subdomain. The heat input and the momentum rate are the same as the previous models.

4.3 Experimental Results

To investigate the momentum generated from condensation interface, several experiments were carried out. To visualize the steam bubble, a high speed camera was used at the frame rate of 3000 and thermocouples were used to measure temperature. Table.2 shows the experimental conditions including initial absolute pressure, initial temperature, mass flow rate, mass flux and heat input.

Table.2 Experimental conditions for steam bubble visualization

	Initial pres. [kPa]	Subcooling range [K]	Mass flow rate [g/s]	Mass flux [kg/m^{2}s]	Heat input [W]
Case1	31.0	33.1 – 44.3	0.0424	3.06	98.8
Case2	31.5	30.5 – 43.1	0.0446	3.22	104
Case3	29.0	24.4 – 41.4	0.0594	4.29	138
Case4	31.6	23.4 - 42	0.0736	5.32	172

From these four cases, two different DCC regimes and the transitional area were found. The regimes highly depends on the mass flux and the subcooling. Fig.4.5 shows the oscillating in and out motion of oscillatory interface regime and fig.4.6 shows transitional regime of oscillatory interface and external chug with encapsulating bubble. Fig.4.7 shows the process of the external chug with encapsulating bubble regime.

At oscillatory interface regime, the condensation interface of the steam bubble does not move much only being oscillated at the amount of less than 0.25D, where D is the inner diameter of steam injection pipe. At the transitional regime, the steam bubble size is getting larger and the oscillation frequency suddenly decreases. At external chug with encapsulating bubble regime, it has a cycle, which has steam bubble generation step, encapsulating of pipe step and steam bubble disappear step as shown in fig.4.7. It has much larger oscillating distance and lower frequency. Fig.4.8 represents the relationship among subcooling, oscillation frequency (f) and oscillating distance (δ/D). When the regime changes from oscillatory interface regime to transitional area, the frequency drops. When the regime changes from transitional area to external chugging, the oscillating distance increases. When mass flux is constant, subcooling makes the regime change but does not affect the value of frequency and oscillating distance.

When mass flux is low and subcooling is high, the condensation occurs near the pipe exit and the oscillatory interface regime is represented. However, when subcooling decreases, the condensation is delayed from previous condensation interface and buoyancy helps the bubble encapsulate the pipe. When the surface of the bubble is getting large enough, the area to be condensed is large, condensation suddenly occurs and the steam bubble quickly disappears. It shows the chugging motion and generate high momemtum. When mass flux is getting high, the oscillatory interface regime is skipped and chugging motion is shown directly.

For all the cases, the oscillating frequency and the oscillating distance were calculated and the regime was investigated. According to the mass flux and subcooling, the regime map is introduced in fig.4.9. By studying oscillating frequency and oscillating distance, two regimes and the transitional area were found and added to the regime map. The other regimes shown in fig.4.9 are based on the DCC regime by C.K.Chan et al. The '+' mark and 'x' mark represent oscillatory interface regime and external chug with encapsulating bubble regime respectively. The mark with rectangular boundary demonstrates the transitional points.

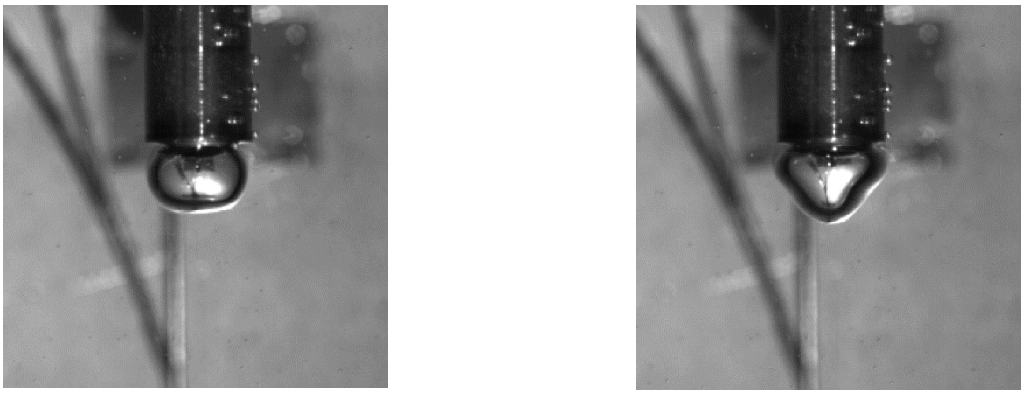

(a) Oscillating in (b) Oscillating out

Fig.4.5 Oscillatory interface regime

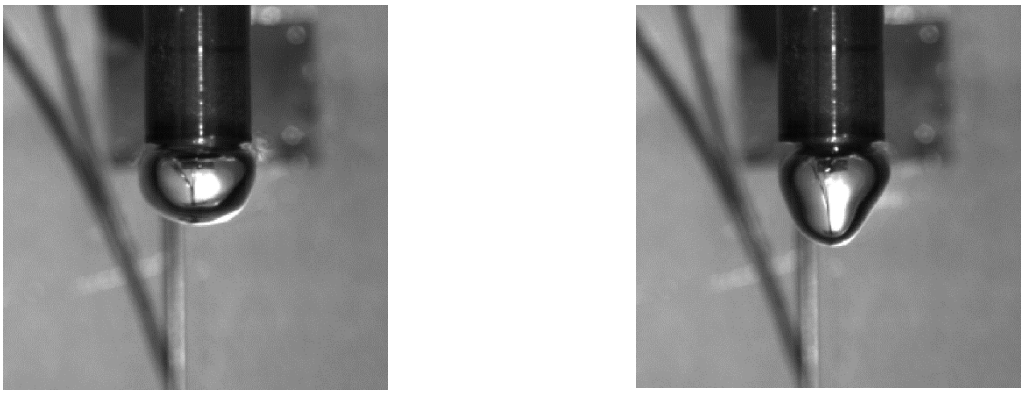

(a) Oscillating in (b) Oscillating out

Fig.4.6 Transitional regime of oscillatory interface and external chug with encapsulating bubble

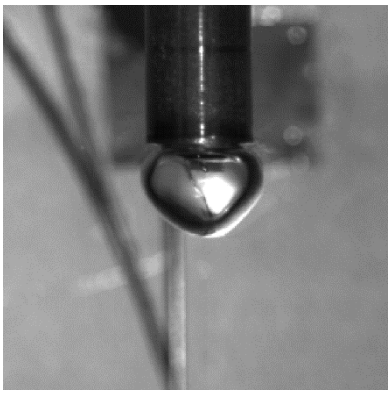

(a) Time = 0×T

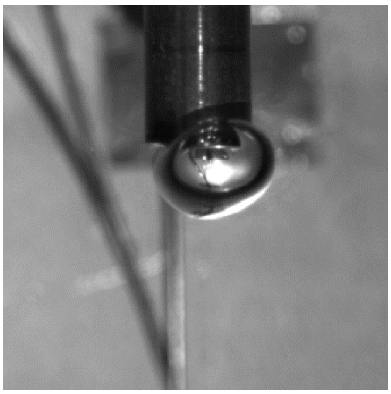

(b) Time =0.064 ×T

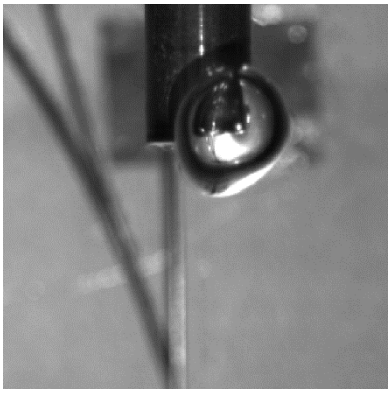

(c) Time = 0.84×T

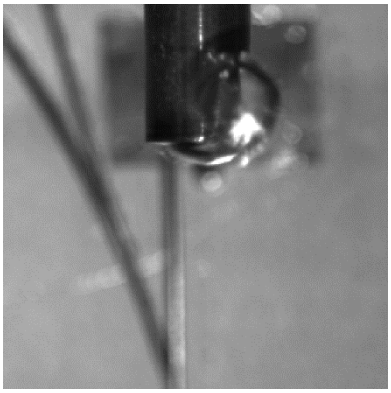

(d) Time = 0.95×T

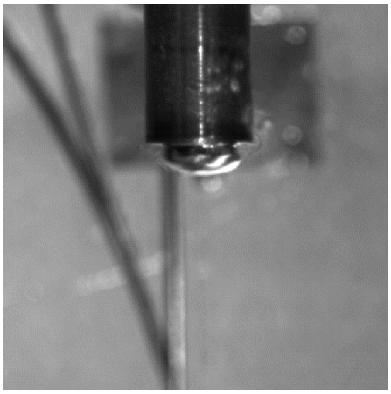

(e) Time =0.98×T

Fig.4.7 External chug with encapsulating bubble

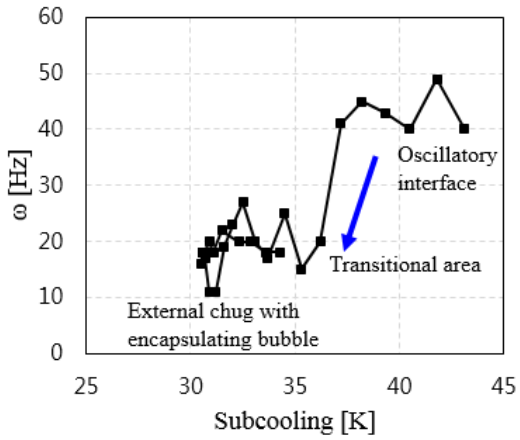

(a) Subcooling – *f*

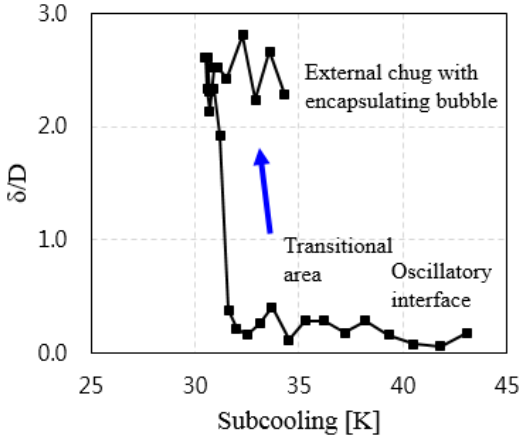

(b) Subcooling – δ/D

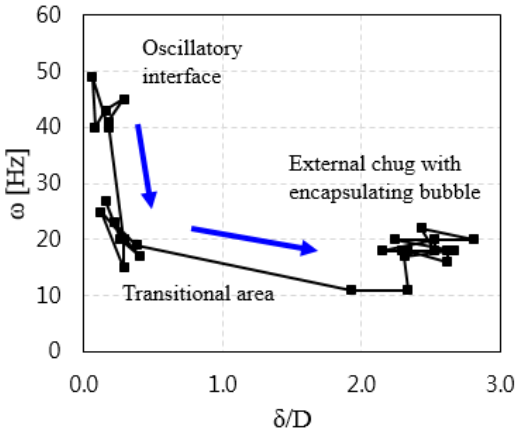

(c) δ/D – *f*

Fig.4.8 Regime transition of case2

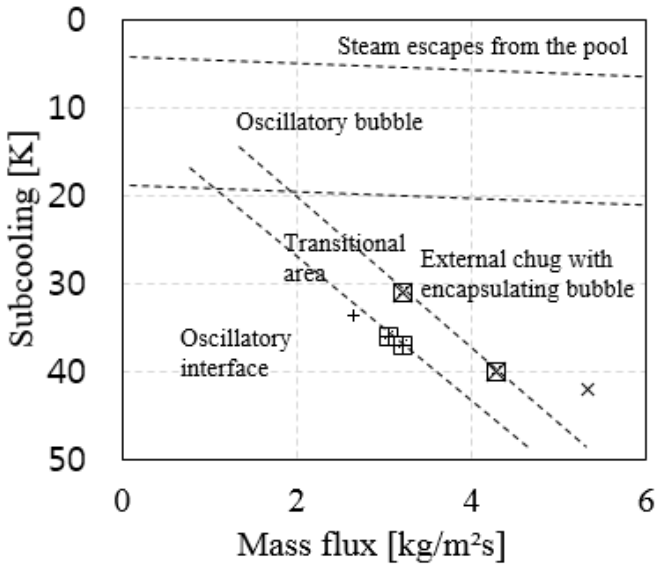

Fig.4.9 DCC regime map for oscillatory interface and chugging regimes

According to the DCC regimes, the momentum equation is introduced as shown in equation (4-2). Fig.4.10 show the schematic of momentum generation at the oscillatory interface regime. The oscillating distance, δ, is very small but it mixes the ambient fluid and the condensate. The condensate temperature decreases quickly from saturation temperature because of the oscillatory condensation interface. It is assumed that the speed of bubble motion is related to momentum. To calculate the speed of bubble motion, the oscillating frequency, f, and the oscillating distance, δ, were used and $f \cdot \delta$ is considered to be the speed of the bubble motion. The bubble motion is quite complicated but it is assumed that the vertical motion is strongly related to the formation of thermal stratification.

It is arguable to decide the momentum from flow experimentally. Especially, the control volume which is affected by momentum is difficult to be defined. However, it is assumed that the control volume is related to the amount of condensate but larger than that. Therefore, mass flow rate, $\dot{m}$, is used to consider the control volume and C_{DCC} is added as constants depending on DCC regimes. $\dot{m}$, f and δ are obtained from experiment and C_{DCC} is obtained by comparing numerical simulation results and experimental results. Although the bubble shapes are different

according to different regimes, the principle would not be different from the oscillatory interface regime.

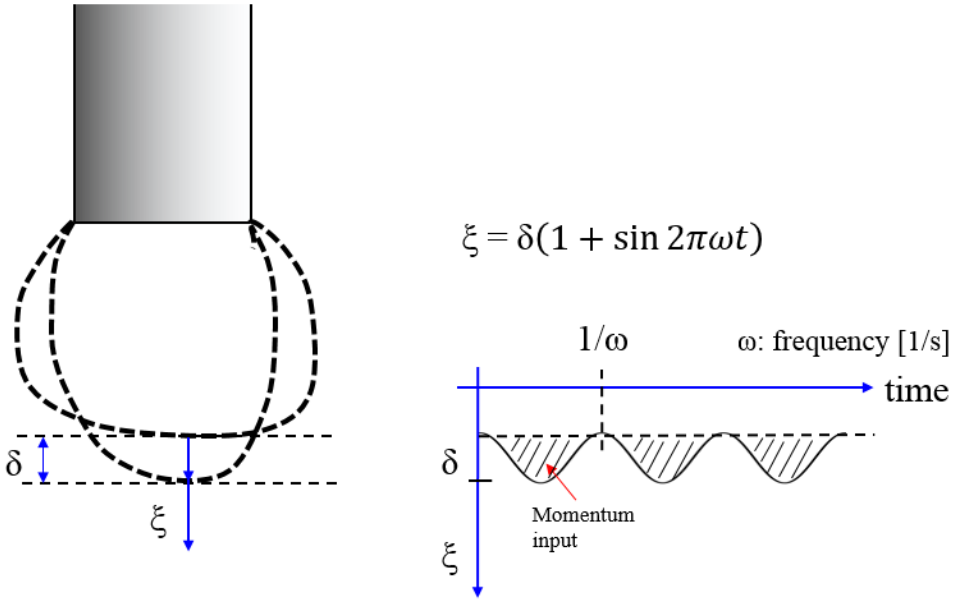

Fig.4.10 The schematic of momentum generation

$$\dot{p} = C_{DCC}\sqrt{2}\dot{m}\delta f \ \text{[kg m/s}^2\text{]} \tag{4-2}$$

f and δ are assumed be the function of mass flux (j_m), subcooling (ΔT_{sub}) and steam injection pipe inner diameter (D). Table.3 shows the summary of the experiments including f and δ. According to the experiments, the oscillating frequency of oscillatory interface regime is around 40 Hz and the one of transitional regime and the external chug with encapsulating bubble regime is around 20 Hz. It is not affected by j_m and ΔT_{sub} but it would be affected by the pipe inner diameter. δ is found to depend on j_m but does not change with ΔT_{sub}. The correlation function of δ at the external chugging regime was obtained depending on j_m with the RMS value of 99.8%. Table.4 shows the summary of the momentum rate calculation. C_{DCC} would be obtained from comparing to numerical simulation. For numerical simulation, the momentum is applied to control volume axially and radially.

Table.3 The summary of experiments (D = 4.2mm)

j_m [kg/m^{2}s]	Oscillatory interface		Transitional regime		External chug with encapsulating bubble	
	ƒ [Hz]	δ/D	ƒ [Hz]	δ/D	ƒ [Hz]	δ/D
3.06	40	0.25	20	0.25		
3.22	40	0.25	20	0.25	20	2.5
4.29			20	0.25	20	3.3
5.32					20	3.8

Table.4 The summary of the momentum calculation (D = 4.2mm)

Oscillatory interface		Transitional regime		External chug with encapsulating bubble	
ƒ [Hz]	δ/D	ƒ [Hz]	δ/D	ƒ [Hz]	δ/D
40	0.25	20	0.25	20	$2.60 \times \ln(j_m) - 0.524$
$\dot{p} = 10\sqrt{2}C_{DCC}D\dot{m}$		$\dot{p} = 5\sqrt{2}C_{DCC}D\dot{m}$		$\dot{p} = C_{DCC}\sqrt{2}D\dot{m}[52.0 \times \ln(j_m) - 10.48]$	

4.4 Numerical Validation

4.4.1 Model Validation

The wall heat flux and volumetric momentum source model (M3) and volumetric heat and momentum source model (M4) are chosen for model validation. For momentum input, the $C_{DCC}\sqrt{2}$ was determined as 40. The exact value of C_{DCC} would be decided by model validations. Since the temperature and velocity were obtained by thermocouples and PIV method, temperature validation and velocity validation are carried out. By temperature validation, C_{DCC} is obtained.

4.4.1.1 Temperature Validation

The temperature profiles in numerical simulation were obtained on the same position of thermocouples in experiment and compared with experimental data. Fig.4.11 shows the temperature profiles. In channel 2-1, 2-2 and 2-3, the profiles of numerical simulation follows well with experimental results that the temperature of channel 2-1 and 2-2 does not increase but the one of channel 2-3 slightly increases due to the momentum near condensation interface. In channel 2-4, 2-5 and 2-6, the temperature increases together with almost constant differences in numerical simulation and experiment but the temperature gap between channel 2-3 and 2-4 is quite different with experimental results. The temperature gradient shows differences in numerical simulation and experiment that the temperature gradient quickly decreases in the process of time in experiment but in the numerical simulation decreases very slightly. That would be because of the heat loss which could not be considered exactly in numerical simulation. The two analytical models shows almost the same results in temperature profiles.

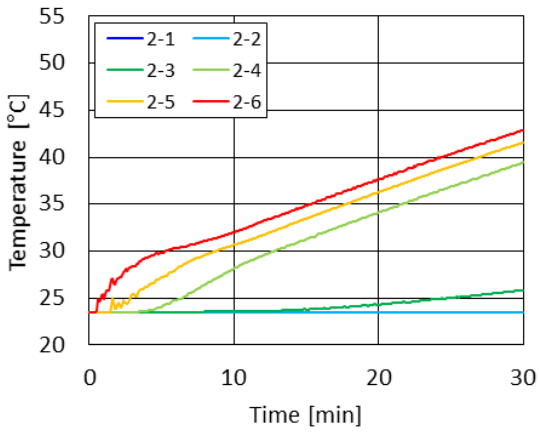

(a) Wall heat flux and volumetric momentum source model (M3)

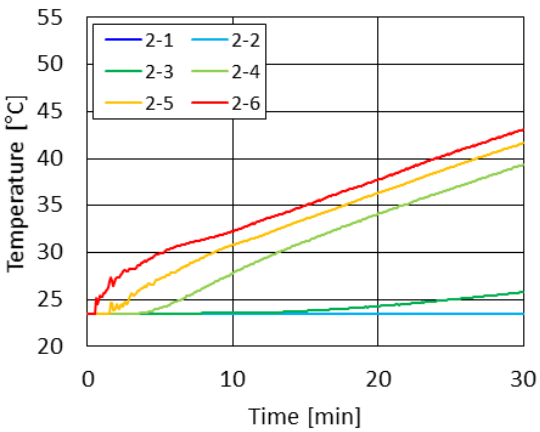

(b) Volumetric heat and momentum source model (M4)

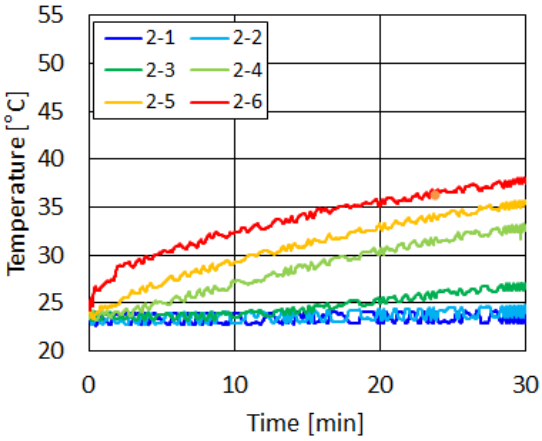

(c) Experiment

Fig.4.11 Temperature profiles for validation

4.4.1.2 Velocity Validation

To validate velocity, the velocity fields are shown at the same plane of PIV measurement. Although numerical simulation does not represent the unstable hot plume shown in the experiment, it shows the strong upward flow induced by buoyancy and the natural circulation. Fig.4.12 shows the velocity fields. Both models shows similar results but M4 shows wider and stronger waving upward flow than M3. Since downward axial momentum is applied to the selected volume, downward flow is shown near the volume and the upward flow induced by buoyancy is right-sided due to natural convection on the left side in both models. M4 shows more instability on the upward flow than M3.

Fig.4.13, fig.4.14 and fig.4.15 shows the velocity profiles on the selected lines, A-A', B-B' and C-C' at the time of 30 minutes, as shown in Fig.3.14. The line B-B' was selected on the center of the upward flow plume at each model. On the line of A-A', experiment shows the clear natural circulation having separated leftward and rightward flow and numerical simulations show good agreement with experiment, which is good advancement from heat flux model (M1) and heat source model (M2) simulation. On the line of B-B', the numerical simulation shows high velocity magnitude as the experiment, which was not shown in M1 and M2 simulation. On the line of C-C', Gaussian distribution is shown in both experiment and numerical simulation and the width of the distribution was improved than M1 and M2.

Generally, M3 and M4 show similar results. Both models show instability on hot condensate plume. The discrepancies between the experiment and the simulations could be induced by several factors; oscillation around the condensation interface, changing viscosity by temperature changes, undefined heat loss, turbulent effects and etc.

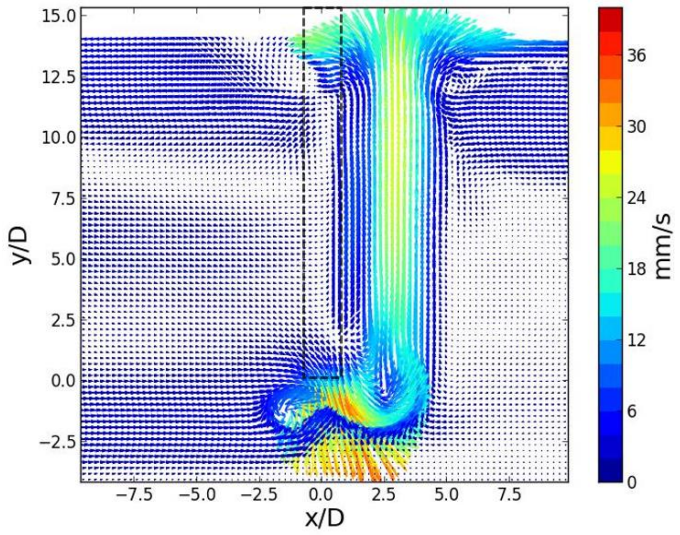

(a) Wall heat flux and volumetric momentum source model (M3)

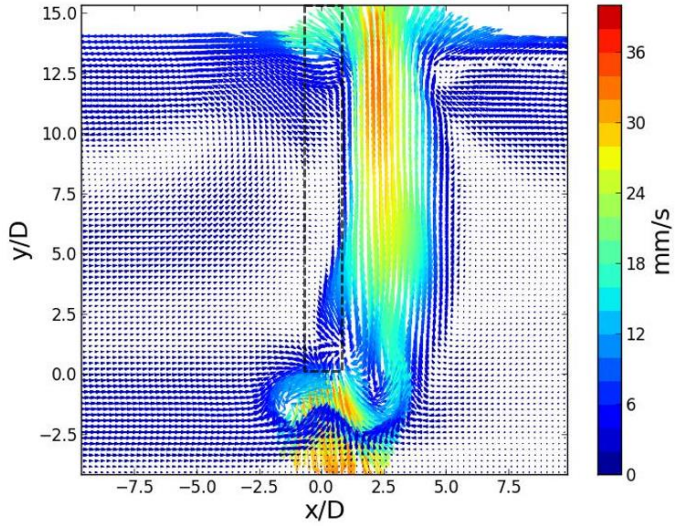

(b) Volumetric heat and momentum source model (M4)

(Continued)

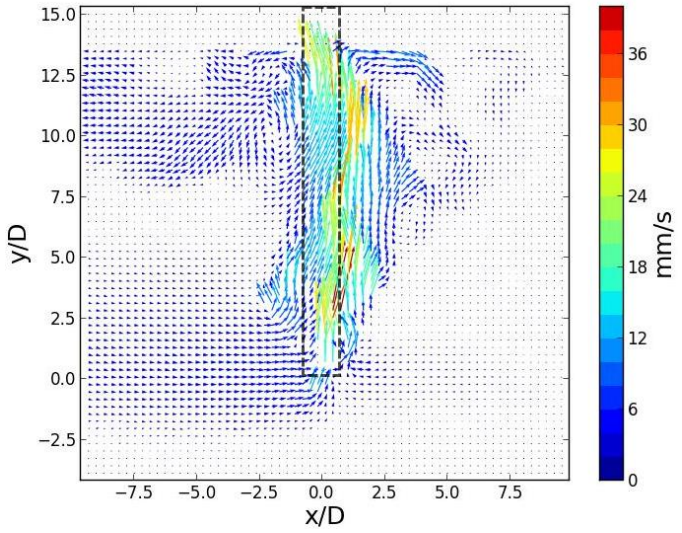

(c) Experiment

Fig.4.12 Velocity field around steam injection pipe at the time of 30 minutes

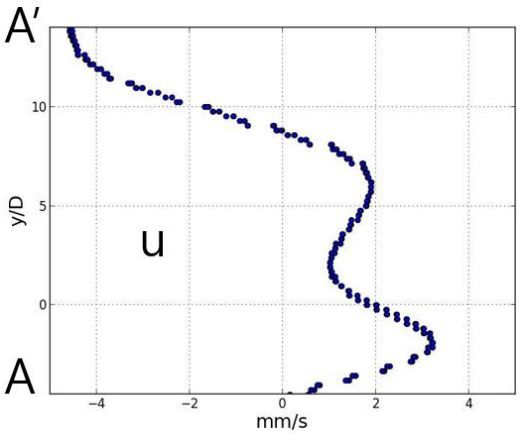

(a) Wall heat flux and volumetric momentum source model (M3)

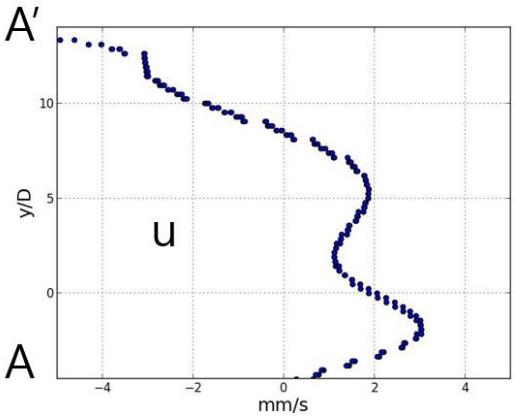

(b) Volumetric heat and momentum source model (M4)

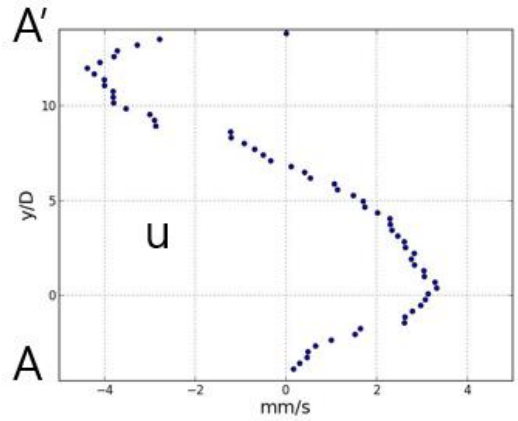

(c) Experiment

Fig.4.13 Velocity profiles (u component) on the A-A’ at the time of 30 minutes

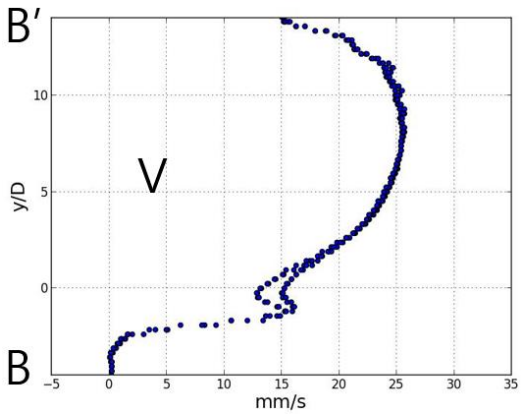

(a) Wall heat flux and volumetric momentum source model (M3)

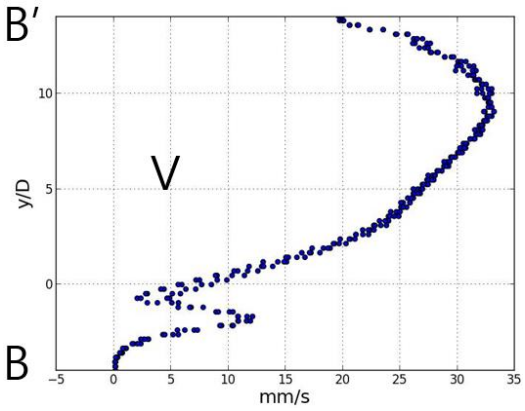

(b) Volumetric heat and momentum source model (M4)

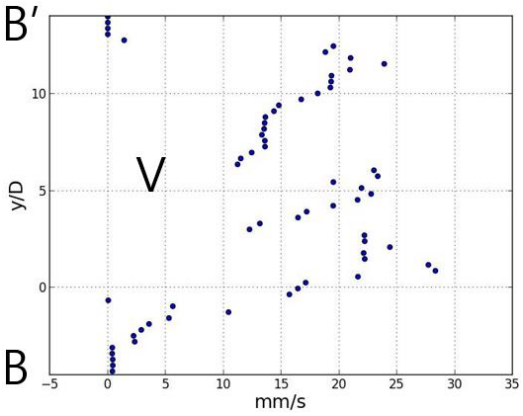

(c) Experiment

Fig.4.14 Velocity profiles (velocity magnitude) on the B-B' at the time of 30 minutes

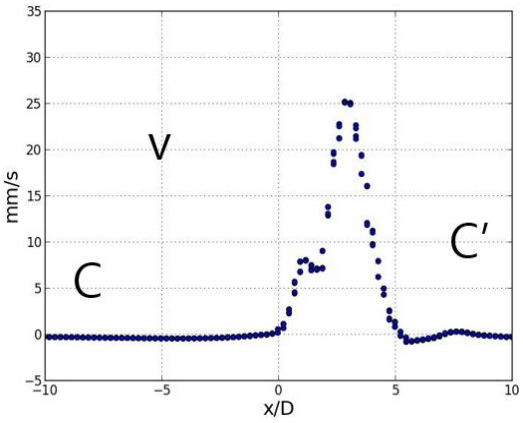

(a) Wall heat flux and volumetric momentum source model (M3)

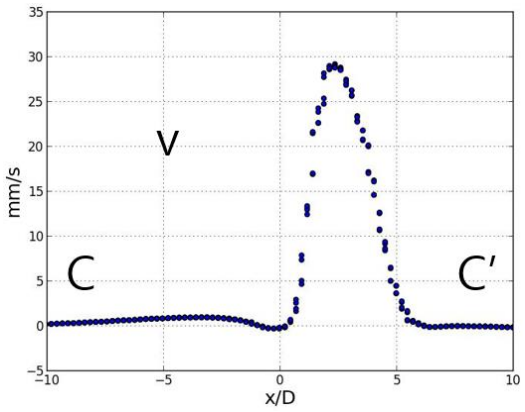

(b) Volumetric heat and momentum source model (M4)

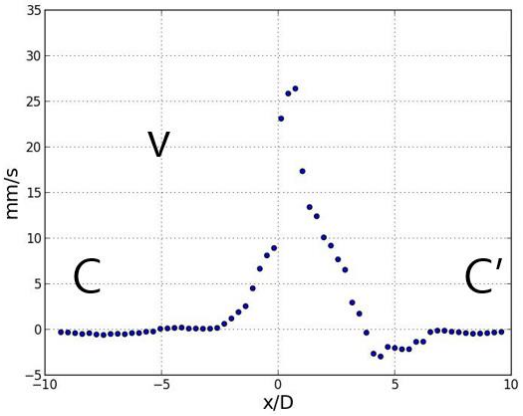

(c) Experiment

Fig.4.15 Velocity profiles (velocity magnitude) on the C-C' at the time of 30 minute

4.4.1.3 Investigation of C_{DCC}

By previous model validations, volumetric heat and momentum source model was chosen. To decide $C_{DCC}\sqrt{2}$, several tests were carried out by changing the constant. The constant changed from 10 to 30 as shown in fig.4.16. As the constant gets larger, the temperature range of mixing area gets smaller due to mixing. It is shown that the temperature differences among channel 2-4, 2-5 and 2-6 are almost constant at all the cases. It is the same phenomenon in experiment as well. Since the temperature distribution, especially of mixing area, is important for thermal stratification, the temperature differences between channel 2-4 and 2-6 were obtained to compare with experimental data.

At the time of 30 minute in experiment, the temperature difference between channel 2-4 and 2-6 is 4.9 °C. In the case of $\sqrt{2}C_{DCC}$ =30, 40 and 50, the temperature differences are 7.5, 3.7 and 1.3 respectively. It decreases as C_{DCC} increases. By interpolation, C_{DCC} is obtained as 25.6. At the value, the temperature profile is shown in fig.4.17. However, while experiment shows decreasing temperature gradient, numerical simulation shows the much lower decrease of temperature gradient. The different temperature gradient would be related to heat loss assumption.

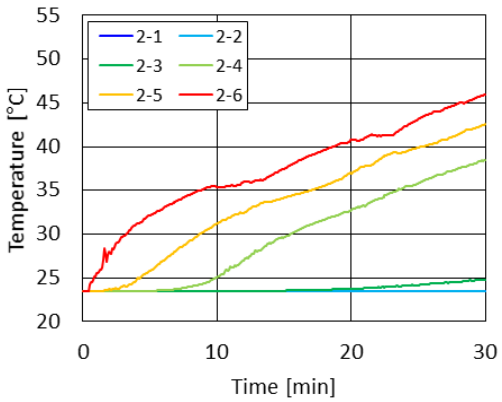

(a) $\sqrt{2}C_{DCC}$ = 30

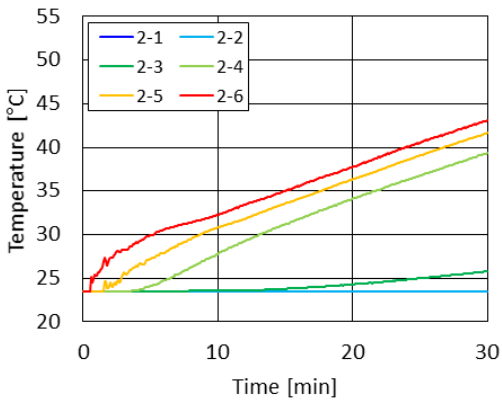

(b) $\sqrt{2}C_{DCC}$ = 40

(Continued)

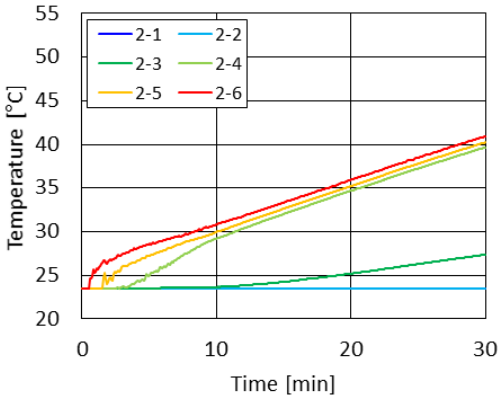

(c) $\sqrt{2}C_{DCC} = 50$

Fig.4.16 Temperature profiles with different C_{DCC} values

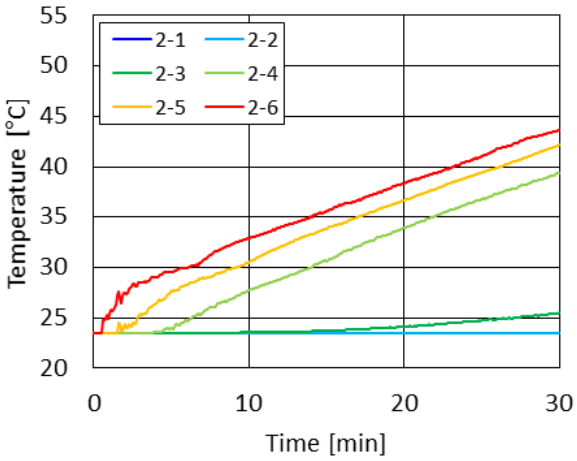

Fig.4.17 Temperature profiles with the C_{DCC} value of 25.6

4.4.1.4 Correction of Overall Heat Transfer Coefficient

As shown in fig.4.17, the temperature gradient at mixing area was overestimated although the driving force induced by heat and momentum source has good agreement with experimental results as it is shown by the temperature difference in mixing area and the flow field near

condensation interface. It is estimated that the overall heat transfer coefficient for heat loss was not correctly decided. There could be several factors to affect the difference of cooling test results and normal experiments; the conduction heat loss of stainless steel from hot area to gaseous area, the heat loss from gaseous area surface of SP, the heat loss from the other systems like steam pipe from steam generator to SP, etc.

The corrected overall heat transfer coefficient was obtained from numerical simulations. Changing the coefficient, the calculations were carried out and the corrected coefficient was obtained by interpolation as 68.2 W/m^{2}K. Fig.4.24 shows the comparison of the temperature profiles in experiment and numerical simulation. It shows good agreement. Corrected volumetric heat and momentum source model (cM4) was completed.

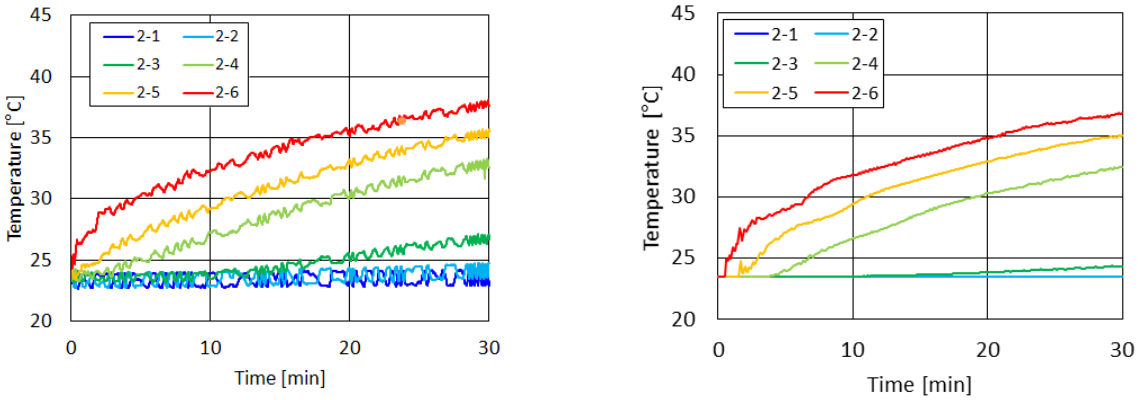

(a) Experiment

(b) CFD (HTC: 68.2 W/m^{2}K)

Fig.4.18 Temperature profiles on the SP center with corrected HTC
(Oscillatory interface regime)

4.4.2 Results

Based on cM4, numerical simulation was carried out. Temperature and velocity are investigated.

4.4.2.1 Temperature

Fig.4.19 shows the temperature fields according to time. The instability is shown in the fluctuating hot condensate plume. To find the mixing interface by temperature, the location which has highest temperature gradient around the mixing interface could be the mixing interface. The temperature increases in mixing area but the temperature of non-mixing area does not change. However, since continually the mixing interface gets wider, it is demonstrated that it is difficult to decide the mixing interface by temperature. By momentum input, mixing effects by oscillating condensation interface were represented around the heat source volume. Fig.4.20 shows the temperature profiles for 30 minutes. It shows good agreement with experiment.

(a) 0 minute

(b) 5 minute

(c) 10 minute

(d) 15 minute

(e) 20 minute

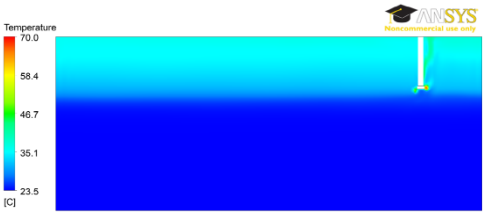

(f) 25 minute

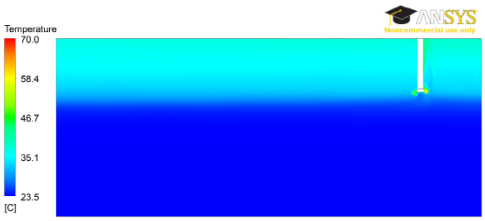

(g) 30 minute

Fig.4.19 Temperature fields

(Volumetric heat and momentum source model, C_{DCC}=25.6)

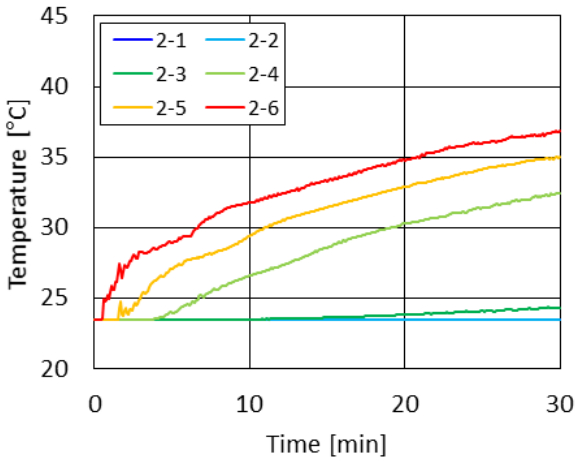

Fig.4.20 Temperature profiles

(Volumetric heat and momentum source model, C_{DCC}=25.6)

4.4.2.2 Velocity

Fig.4.21 represents the stream line with the color of velocity magnitude. It is shown that the area near pipe has strong upward flow and it induces the natural circulation in mixing area. Non mixing area has secondary flow by natural convection but the velocity is very weak. Fig.4.22 shows the velocity fields in the process of the time. It represents that the buoyant flow has high fluctuation by momentum and the flow field changes in the process. The velocity fields have instability from momentum source which could not be shown in M1 and M2 simulation.

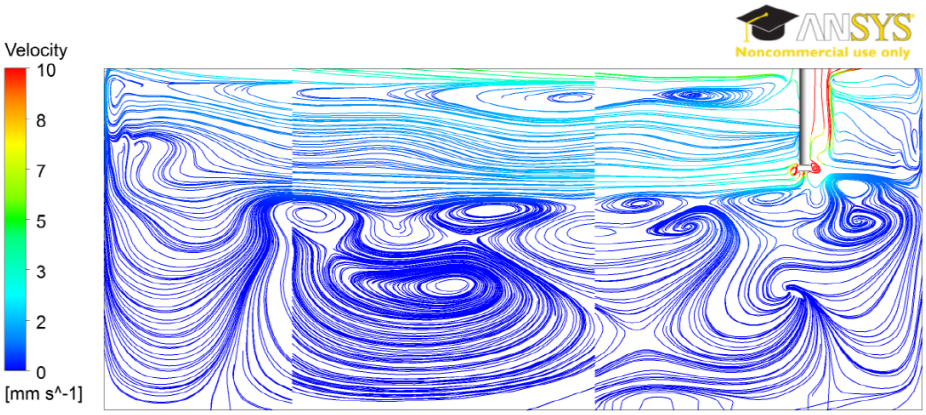

Fig.4.21 Stream line with velocity magnitude

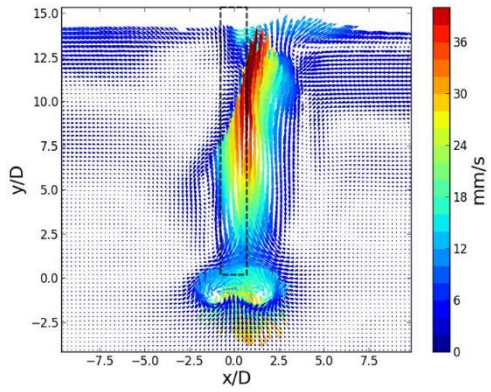

(a) 5 minute

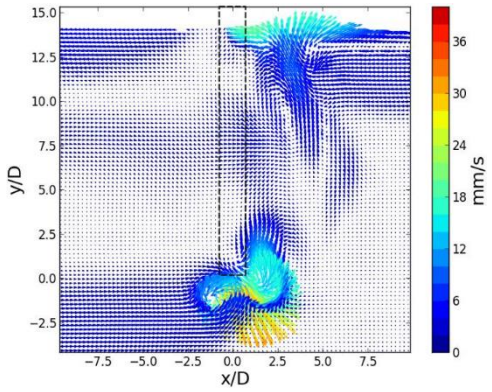

(b) 10 minute

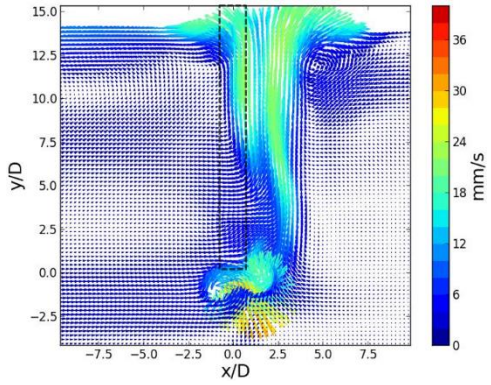

(c) 15 minute

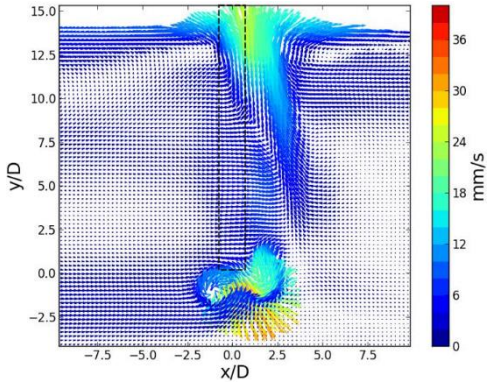

(d) 20 minute

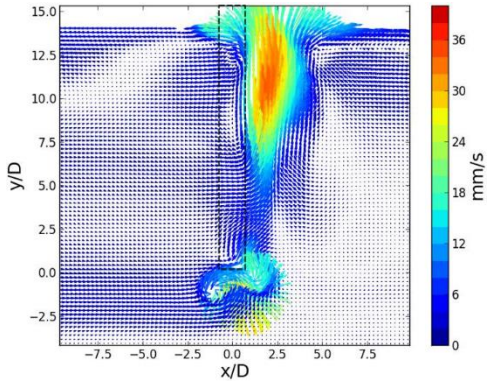

(e) 25 minute

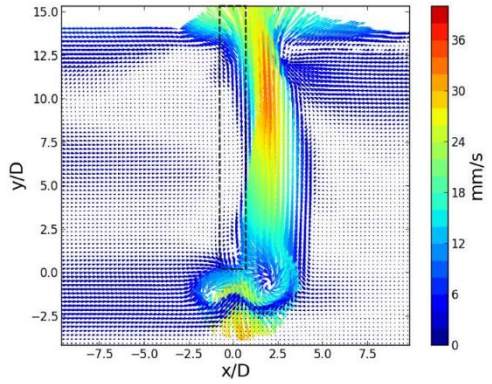

(f) 30 minute

Fig.4.22 Velocity fields

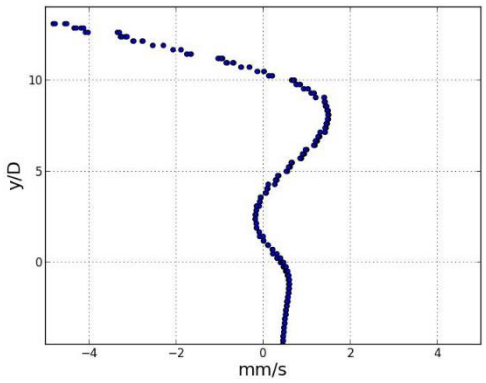

(a) 5 minute

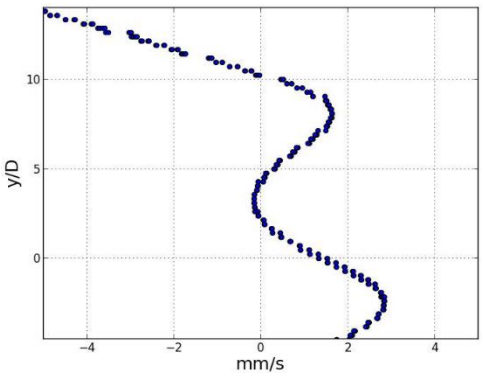

(b) 10 minute

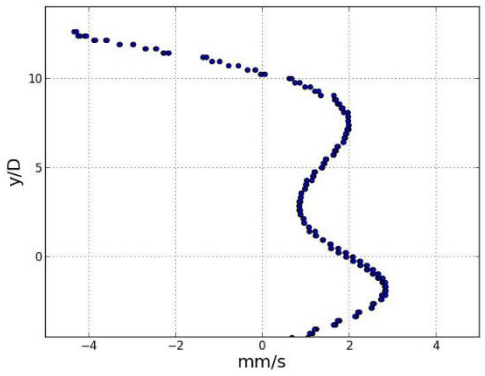

(c) 15 minute

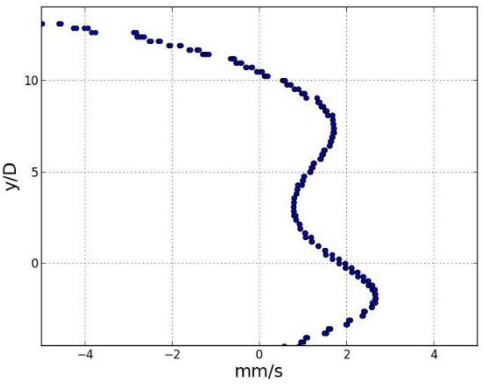

(d) 20 minute

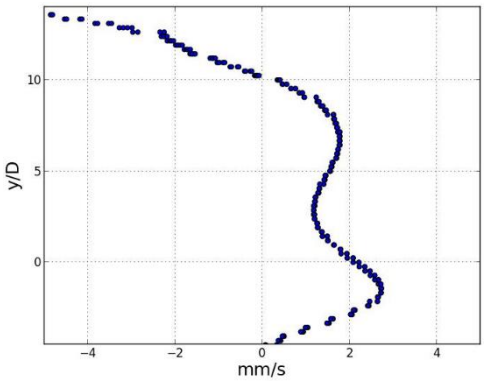

(e) 25 minute

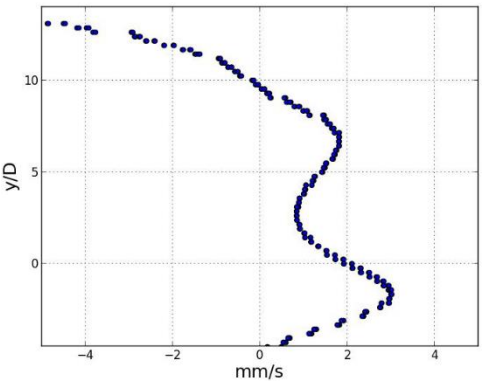

(f) 30 minute

Fig.4.23 u profiles at the line of A-A’

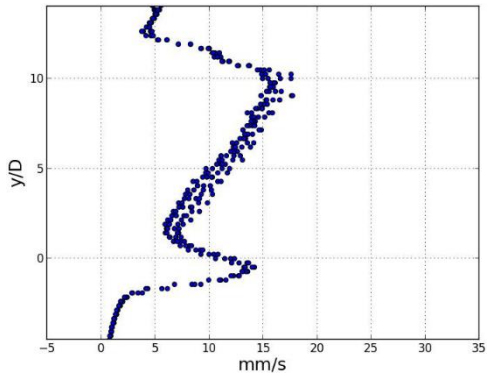

(a) 5 minute

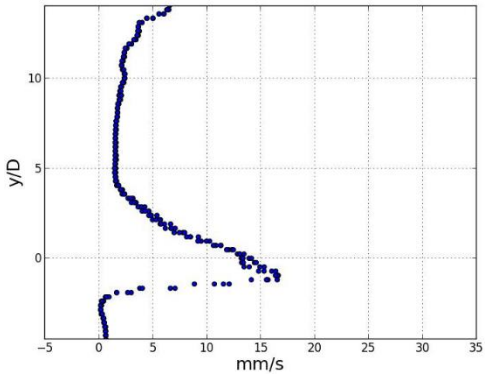

(b) 10 minute

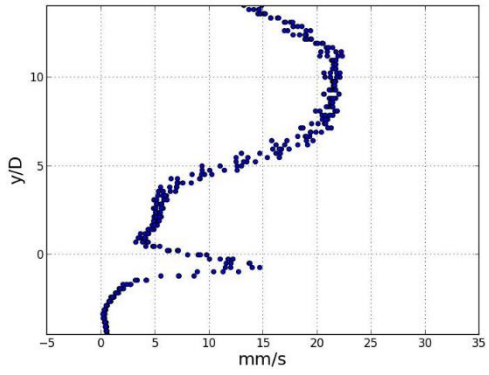

(c) 15 minute

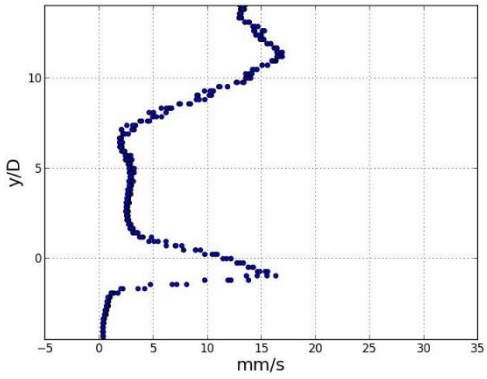

(d) 20 minute

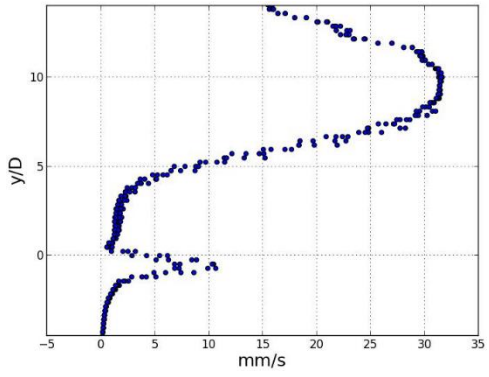

(e) 25 minute

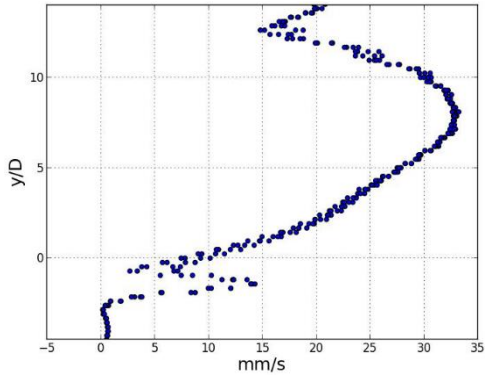

(f) 30 minute

Fig.4.24 Velocity magnitude profiles at the line of B-B'

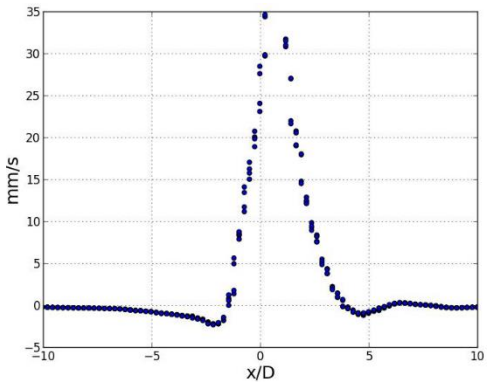

(a) 5 minute

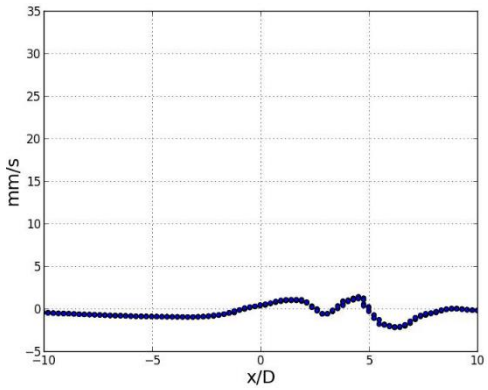

(b) 10 minute

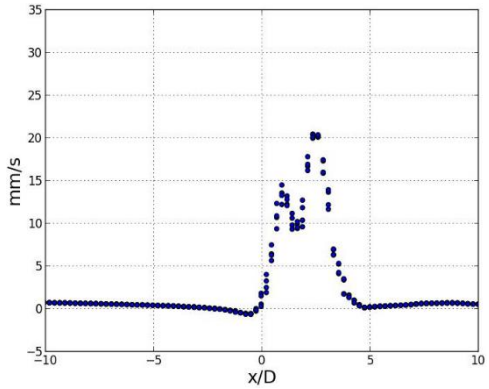

(c) 15 minute

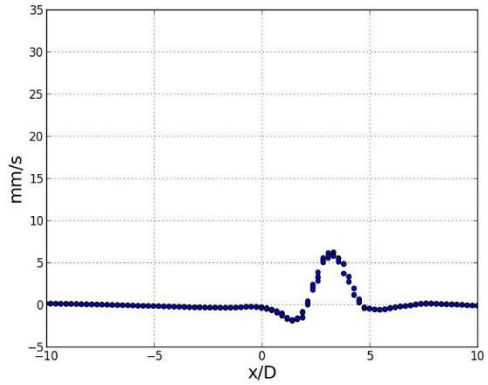

(d) 20 minute

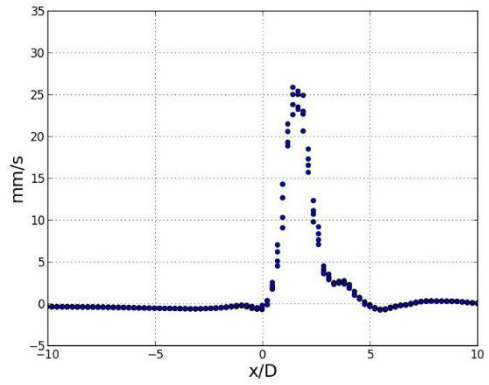

(e) 25 minute

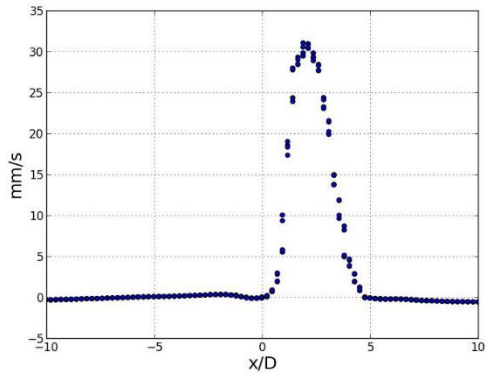

(f) 30 minute

Fig.4.25 v profiles at the line of C-C’

Fig.4.23 shows the u component profiles at the line of A-A' as shown in Fig.3.14. The natural circulation is shown and it is getting stronger. Maximum velocity of leftward flow does not increase since 5 minutes but the one of rightward flow increase slightly until 30 minutes. While the amounts of leftward flow and rightward flow are similar in experiment, rightward flow is much stronger than leftward flow in numerical simulation.

Fig.4.24 shows the velocity magnitude profiles at the line of B-B'. The maximum velocity is similar to the experiment and it shows strong fluctuation and instability from momentum source. Fig.4.25 shows the v component profiles at the line of C-C'. The width of the distribution is shorter than experiment but the maximum v component is quite similar.

4.5 Discussion and Summary

Since single phase code cannot simulate thermal stratification correctly, momentum was considered in this chapter. To calculate momentum, the corresponding velocity at far-field was investigated. To obtain the corresponding velocity, steam bubble visualization experiment was carried out and the oscillation frequency and steam bubble amplitude were studied. It is found that the frequency has constant value in the same DCC regime with variance. In ECEB regime, the amplitude increases with increasing steam mass flux. The momentum was considered in the radial direction and axial direction.

By model validation, corrected volumetric heat and momentum source model (cM4) was chosen as thermal stratification simulation model. Comparing with experimental data, C_{DCC} was obtained as 25.6. This model results show good agreement with experiment. Firstly, it shows strong natural convection in mixing area. Secondly, it shows fluctuation and instability along the hot plume from heat and momentum source volume. Third, it shows good agreement in velocity magnitude. Fourth, the temperature gradients in mixing area are in good agreement with experiments applying corrected overall heat transfer coefficient.

CHAPTER 5 DOWNSIZED TORUS SUPPRESSION POOL MODEL SIMULATION

5.1 Downsized Torus Suppression Pool

5.1.1 Experimental setup

1:20 scaled-down torus SP model was designed and equipped with a boiler in Tokai as shown in Fig.5.1. The diameter of the torus is 1.5 m and the diameter of the cross section is 0.4 m. The original model of this torus SP model is the SP of Mark I containment. To validate CFD results, one steam pipe is installed and submerged into the subcooled water inside the torus. A steam generator (Miura, ME-100) is connected to the pipe and sends steam to the SP as shown in Fig.5.2. The steam generator is controlled by the pressure and the maximum pressure is 0.69MPa. The mass flow rate served is 149 kg/h but the flow rate is controlled by valves to be injected to SP. The switch on/off type steam generator is one reason which makes the mass flow rate fluctuated. In the yellow color section, there are 132 holes (12 rows separating 30 degree circular direction of the steam pipe and 11 holes in each row) for steam injection. This system is covered by heat isolation material and the main steam lines were covered by line heaters for steam not to be condensed inside the pipe before the steam injection exit.

A safety valve is installed for SP not to exceed the design pressure (0.2 MPa) and a vacuum pump is equipped to control the pressure of SP. A flow meter (OVAL Corporation, VPW9015) is installed on the steam pipe outside of the torus to measure flow rate. Water level is represented by a bypass glass tube but could be calculated exactly by measuring the pressure difference of the gaseous part and the bottom of SP.

36 thermocouples (T-type) and a pressure transducer (Sensez, HLVC-100KP-02) were installed inside the SP as shown in Fig.5.3 and Table.5 to obtain time resolved temperature and pressure data. The measurable pressure range is from -100kPa to 100kPa. The thermocouples and the pressure transducer are connected to a data logger (KEYENCE, NR-TH08) and the electric signals are changed to temperature and pressure data. To investigate the horizontal characteristic of pool temperature, 8 different horizontal positions were chosen. 5 different depths for checking thermal stratification in liquid part and one depth for gas part were chosen.

Before the experiment, the air inside the steam generator was blown out to outside and the dissolved air was removed by keeping SP on vacuum condition by the vacuum pump. The flow rate is controlled by two valves; one is near the steam generator and the other one is near the SP.

Fig.5.1 The experimental equipment

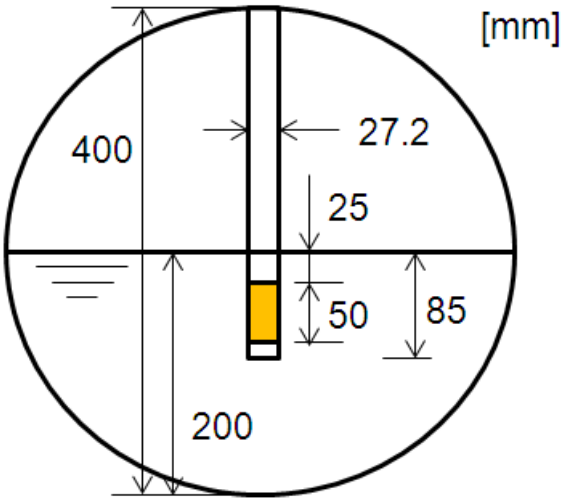

Fig.5.2 The cross section of the torus and the steam pipe for CFD validation

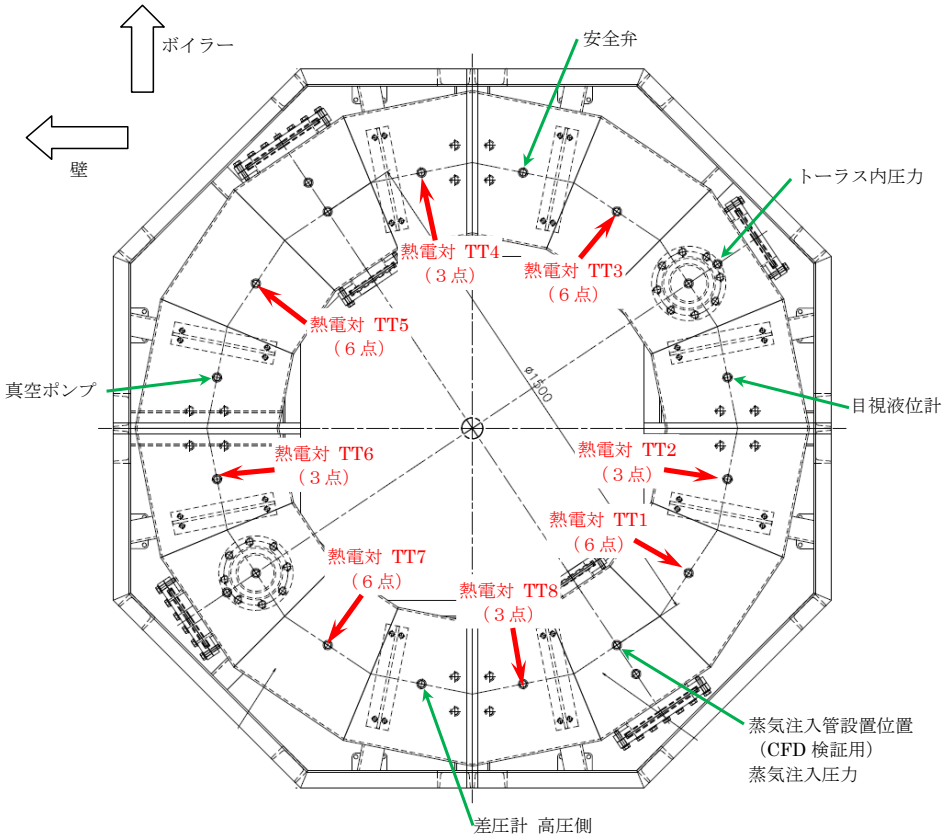

Fig.5.3 The schematic of downsized torus and the position of thermocouples

Table.5 The installation specification of thermocouples

	Height [mm]					
	10	50	100	150	200	300
TT1	TT1-010	TT1-050	TT1-100	TT1-150	TT1-200	TT1-300
TT2	TT2-010		TT2-100		TT2-200	
TT3	TT3-010	TT3-050	TT3-100	TT3-150	TT3-200	TT3-300
TT4	TT4-010		TT4-100		TT4-200	
TT5	TT5-010	TT5-050	TT5-100	TT5-150	TT5-200	TT5-300
TT6	TT6-010		TT6-100		TT6-200	
TT7	TT7-010	TT7-050	TT7-100	TT7-150	TT7-200	TT7-300
TT8	TT8-010		TT8-100		TT8-200	

5.1.2 Experimental condition and the results

The initial water temperature is 25.7°C and the initial SP pressure is 16.6 kPa. The SP pressure and the saturation temperature are represented in fig.5.4. Fig.5.5 shows saturation temperature and the temperature at the height of 150mm. The difference is the subcooling. The steam flow rate is 3.77 kg/hr and the steam mass flux is calculated as 10.1 kg/m^{2}s. According to DCC regime map, this belongs to external chug with encapsulating bubble regime.

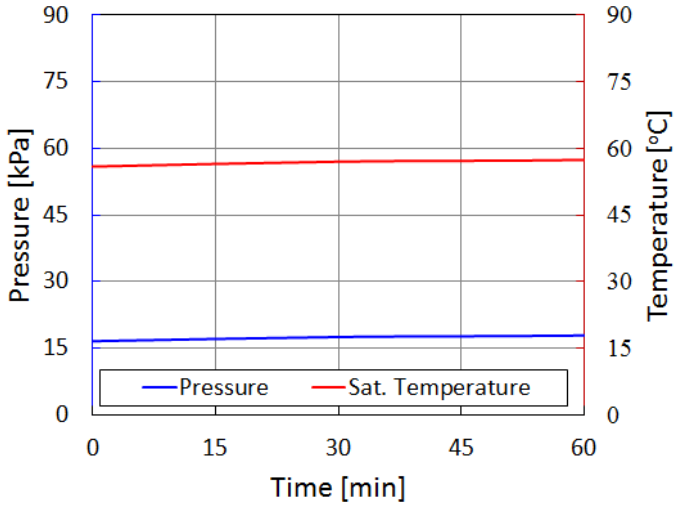

Fig.5.4 SP pressure and the saturation temperature

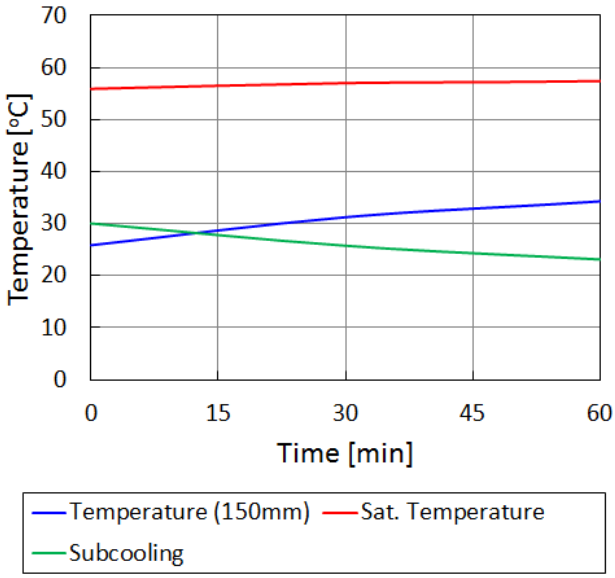

Fig.5.5 Water temperature, saturation temperature and subcooling

Steam was condensed in subcooled water and thermal stratification was shown as fig.5.6. Fig.5.6 shows the temperature at the position of TT1. The temperature of TT1-200, TT1-150 and TT1-100 increase from the beginning having almost constant differences. The temperature of TT1-050 and TT1-010 increase having lower temperature gradients. The temperature gradient of TT1-010 is the lowest.

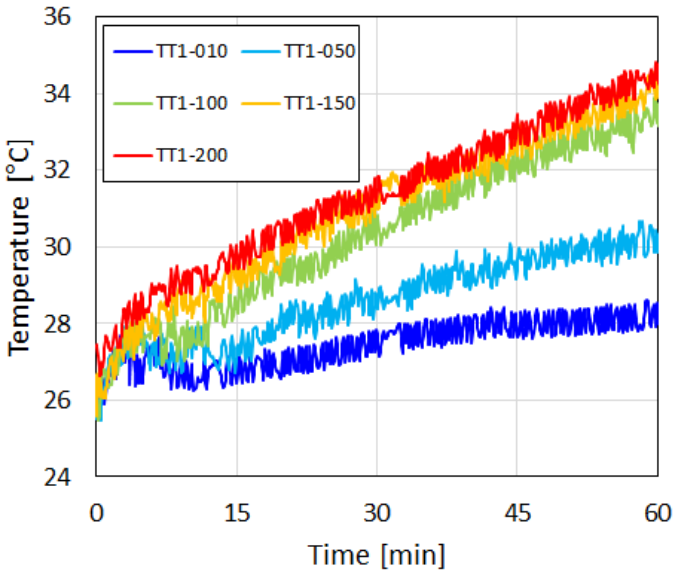

Fig.5.6 Temperature profile at TT1

5.2 Numerical Setup

5.2.1 Downsized Torus Suppression Pool Model

Numerical simulation of thermal stratification was carried out on single phase with ANSYS CFX 14.0. Since the steam condensation finishes around the exit of the steam pipe and only heat and momentum are transferred to water, heat source and momentum source are considered around the exit of the submerged steam pipe. Because the top temperature does not increase over than the saturation temperature at the pressure of the pool, the evaporation and condensation at the interface of the top of the liquid and the bottom of the gas do not happen. Therefore, single phase calculation was carried out for this simulation.

Natural and mixed convection flows can be modeled by CFX with buoyancy source terms. Because this is natural convection and buoyancy-driven flow by density difference, full buoyancy model was selected. Calculation is done on laminar mode. Because there is no forced convection and no large turbulence compared to the size of the torus, the flow could be regarded as laminar flow. Since the most conservative calculation about thermal stratification is on laminar, the calculation was done on laminar mode firstly.

Fig.5.7 shows the overview of the downsized torus suppression pool model and the mesh. This model is three dimensional. The mesh was generated by the commercial meshing tool, ICEM CFD. Mesh type is tetra and mixed mesh. The number of total nodes which are calculated is 37367. The volume was separated into two parts, the volume around condensation interface for heat source or momentum source and the entire volume. The volume for the source is selected as subdomain and heat and momentum source could be applied to the subdomain as shown in fig.5.8. The part of red color is the subdomain for heat and momentum source. Volumetric heat and momentum source model was chosen for this simulation. Heat input, 2.48kW, was calculated from steam mass flow rate and applied to the volumetric heat source. Momentum input was calculated by the equation (3-23) and applied.

The wall boundary is set up as adiabatic and no slip condition except for liquid top, free slip condition. Applied advection scheme is upwind and 2nd order central differencing hybrid scheme and the transient scheme is 2nd order backward Euler scheme. The summary of the numerical simulation conditions is demonstrated in Table.6. Physical time duration is 30 minutes and time step is 0.2 s. The initial temperature is the same initial temperature with the experiment, 25.7°C.

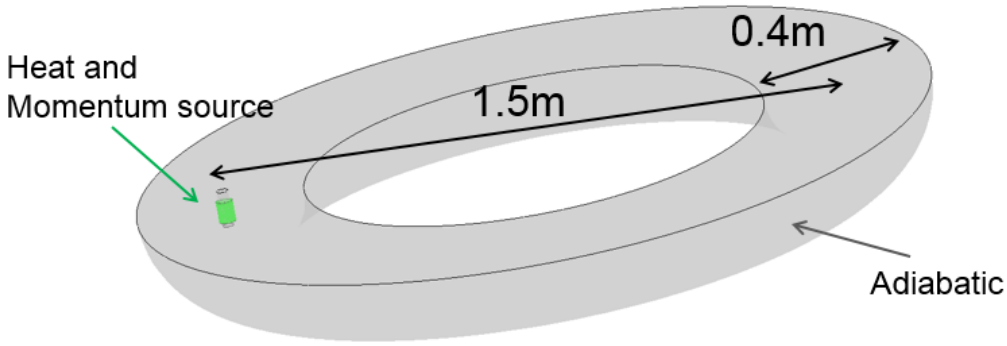

(a) Model surface view

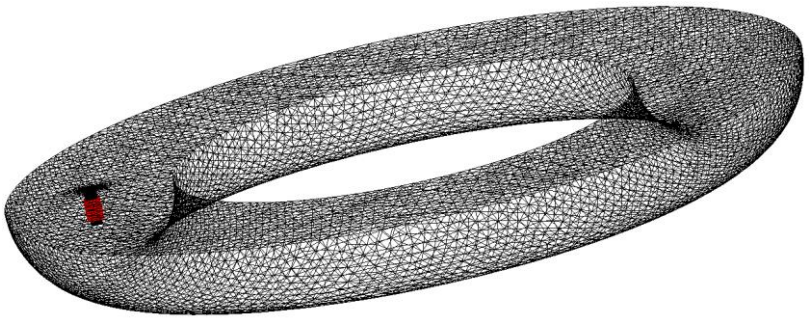

(b) Mesh

Fig.5.7 The overview of the downsized torus suppression pool model

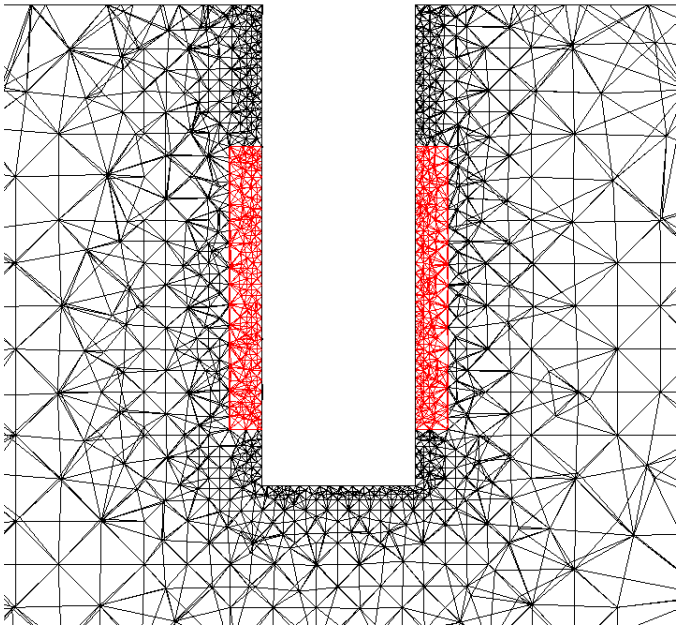

Fig.5.8 Grids around the steam injection pipe

Table.6 The specification of conditions for downsized torus SP model

Turbulence	None (Laminar)
Heat transfer	Total energy model
Buoyancy	Full buoyancy model
Heat input	2.48kW
Momentum input	$C_{DCC}\ \dot{m}\delta f$
Physical time duration	40 minutes
Advection scheme	Upwind and 2nd order central differencing hybrid scheme
Transient scheme	2nd order backward Euler scheme

To calculate the momentum, δ and f should be defined. Because the size of the steam exit is different from 2D SP, the relationship between j_m and δ and f would be different from Table.2 and Table.3. According to table.3, δ would be 2.8 mm and f would be 40 Hz. Fig.5.9 shows steam bubbles around the exit of steam injection pipe. This image was obtained by a high speed camera at the frame rate of 5000. The bubble oscillating frequency, f, was around 250Hz. The maximum bubble size was 4 mm in length and 2 mm in width. Therefore, the oscillating distance, δ, can be 4 mm radially and 1 mm axially since the bubble has both sides, upward and downward, in the axial direction and the oscillating distance of one direction in the axial direction would be the half of the bubble size as shown in fig.5.6 (b). C_{DDC} was used as the same value for oscillatory interface regime of 2D SP model. The momentum input was calculated as 1.48×10^{-2} kg·m/s^2.

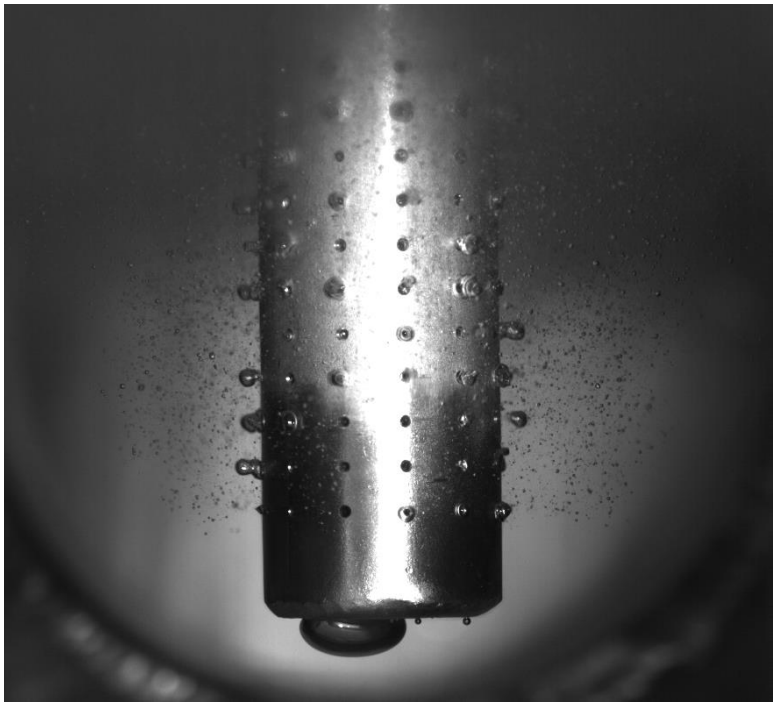

(a) Steam bubbles and condensation

(Continued)

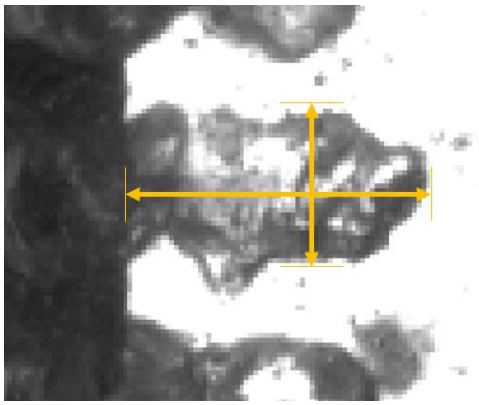

(b) Steam bubble size

Fig.5.9 Steam bubbles around the exit of steam injection pipe

5.3 Validation

5.3.1 Temperature Profiles

At the same position, the temperature distributions obtains as shown in fig.5.10, fig.5.11, fig.5.12 and fig.5.13. It is shown that the temperature is overestimated at the height of 150mm and 200mm but the temperature is underestimated at the height of 10mm, 50mm and 100mm from fig.5.10 and fig.5.11. It is assumed that the momentum is weaker in numerical simulation than experiment. Because of the weak momentum, the temperatures on bottom layer do not change as shown in fig.5.12. Fig.5.13 shows that top area has heat accumulation area around the steam injection pipe at the amount of around 2K. This simulation shows thermal stratification but the momentum should be recalculated. Since this C_{DCC} is for oscillatory interface, this C_{DCC} for chugging regime should be investigated and applied. However, it shows similar trend with experimental results.

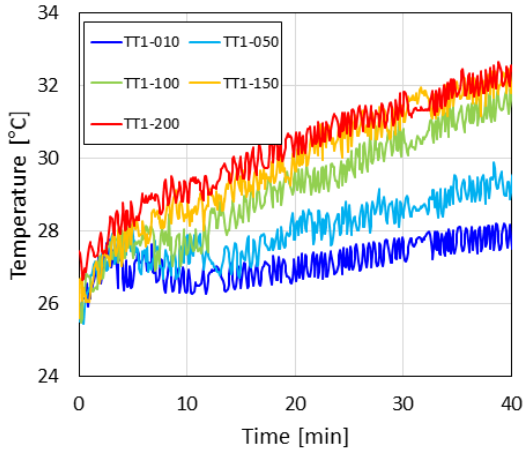

(a) Experiment

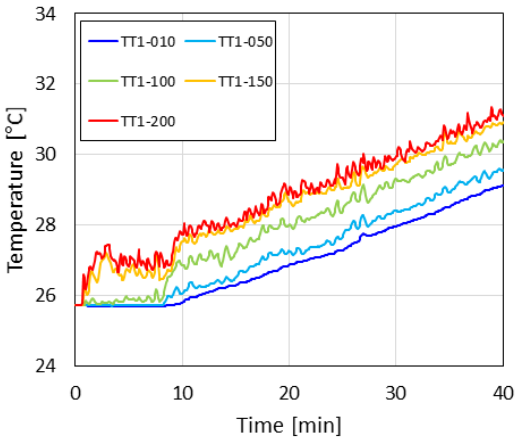

(b) Numerical simulation

Fig.5.10 Temperature profiles at the line of TT1

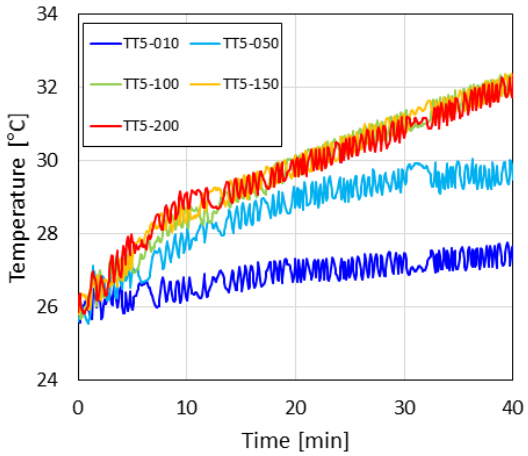

(a) Experiment

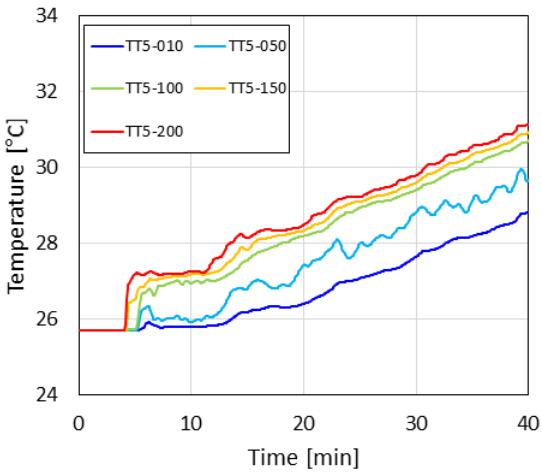

(b) Numerical simulation

Fig.5.11 Temperature profiles at the lie of TT5

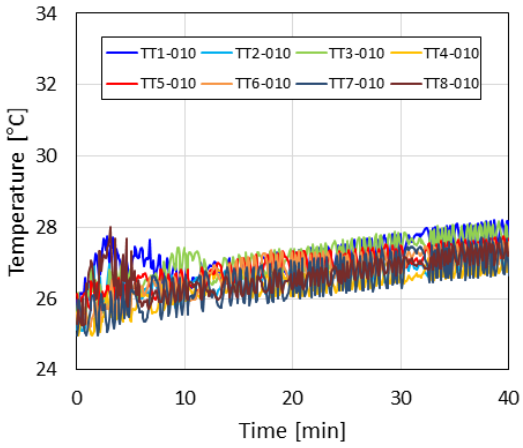

(a) Experiment

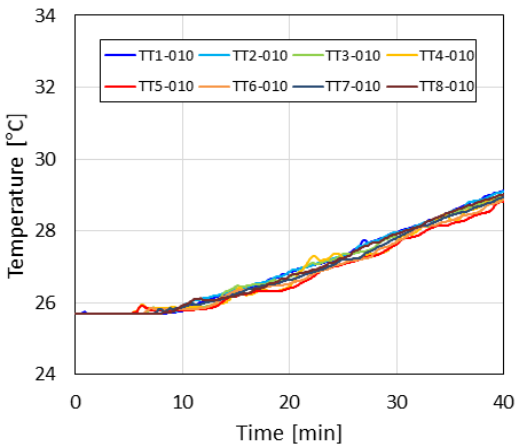

(b) Numerical simulation

Fig.5.12 Temperature profiles on bottom layer

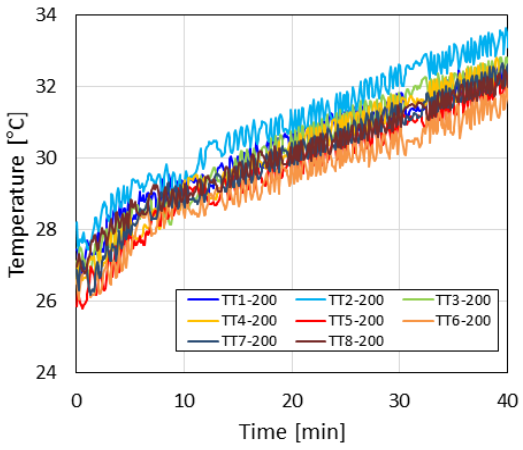

(a) Experiment

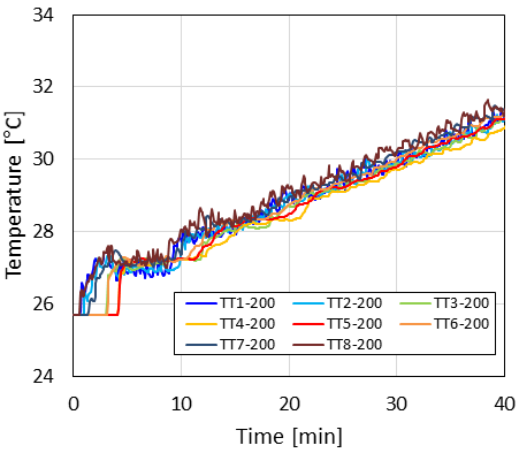

(b) Numerical simulation

Fig.5.13 Temperature profiles on top layer

5.4 Simulation Results and Discussion

5.4.1 Temperature Fields

Fig.5.14 demonstrates the overall temperature distribution around the surface of water area at the time of 40 minutes. Thermal stratification and mixing interface is clearly identified. Fig.5.15 shows the temperature distribution on the top of the water at the time of 40 minutes. As shown in fig.5.13, heat accumulation around the steam injection pipe is demonstrated in the fig.5.15.

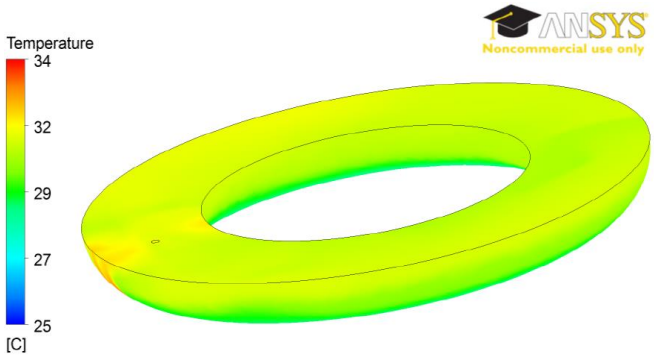

Fig.5.14 Temperature distribution

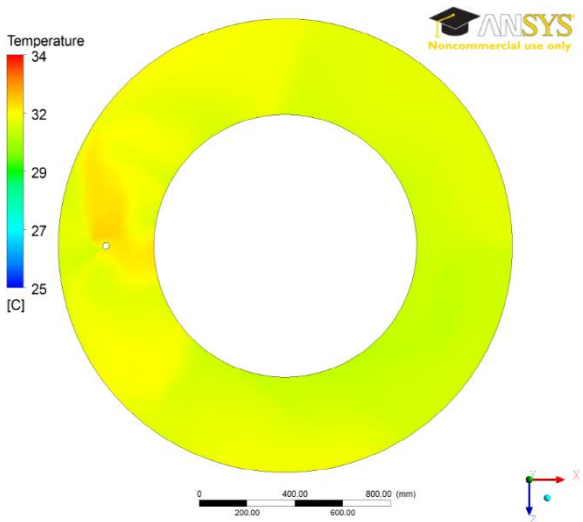

Fig.5.15 Temperature distribution on the top of the water

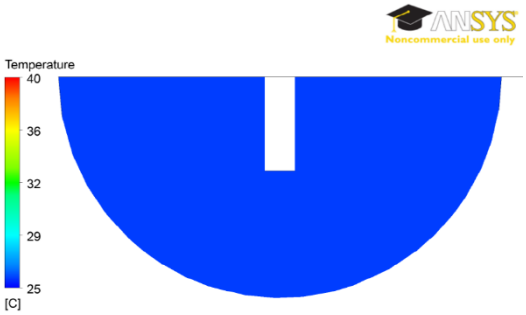

(a) 0 minute

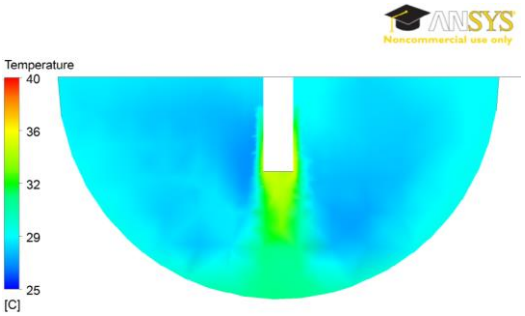

(b) 10 minutes

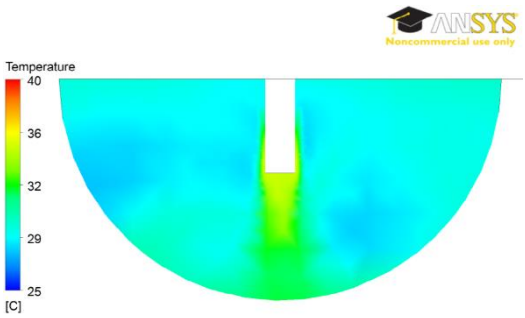

(c) 20 minutes

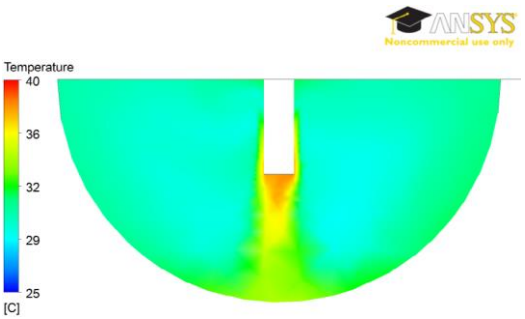

(d) 30 minutes

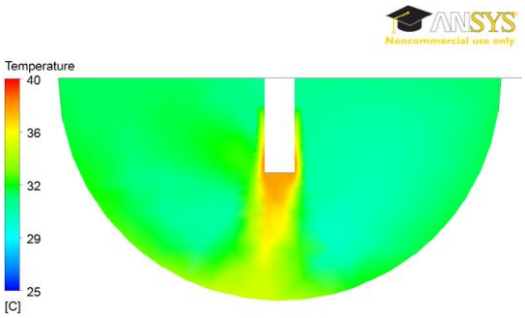

(e) 40 minutes

Fig.5.16 Temperature fields around the steam injection pipe

Fig.5.16 shows the temperature fields around the steam injection pipe in the process of time. The momentum from the control volume mixes the circumferential water with hot water from heat source. The mixing area shows the quite constant temperature distribution, which is regarded as the effects of momentum. It is assumed that since the momentum is weak, the hot water is not able to mix the water under the level of steam injection pipe.

5.4.2 Velocity Fields

Fig.5.17 and fig.5.18 represent the velocity field and the streamline around steam injection pipe. Hot water from heat source make upward flow by buoyancy and induce natural convection in mixing area.

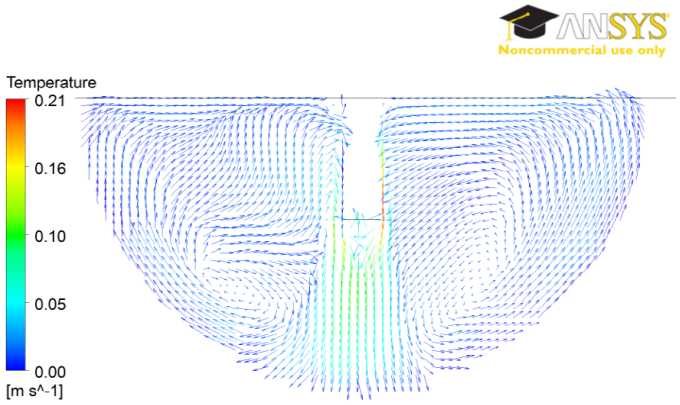

Fig.5.17 Velocity field around steam injection pipe

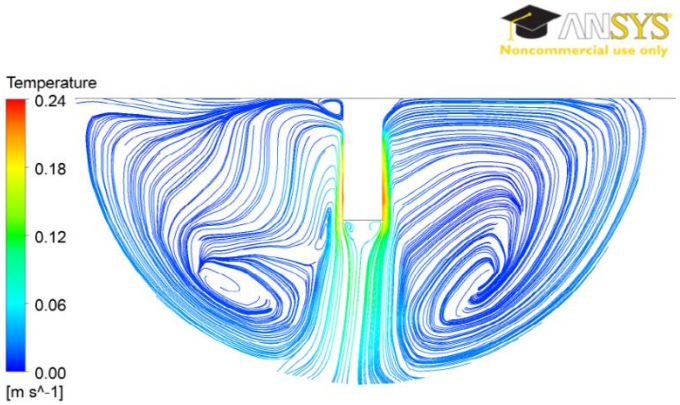

Fig.5.18 Streamline near steam injection pipe

5.5 Summary and discussion

Volumetric heat and momentum source model was applied to simulate downsized torus experiment. Since C_{DCC} for oscillatory interface is used, the momentum is weak. Weak momentum cannot mix lower part and the temperature on bottom area was not changed in numerical simulation. More careful calculation of momentum is needed for simulation of thermal stratification. C_{DCC} should be known at all the DCC regimes for momentum to be applied.

5.6. Conclusion

To understand unexpected pressure increase of SP in Fukushima accident and give useful information to LWRs designers for nuclear safety, downsized 2D SP was designed and experiments were carried out. This research is carried out to understand thermal stratification in SP experimentally and analytically and to predict the thermal stratification by single phase CFD code. Because of complicated phenomena depending on DCC regimes and the difficulties of accurate momentum calculation from two phase simulation, single phase model is selected and additional heat and momentum models are investigated.

At oscillatory interface regime, temperature distribution and velocity field around steam injection pipe were obtained. To measure momentum from condensation interface, the oscillating frequency and the amplitude were investigated and the regime between oscillatory interface and external chugging was found. To simulate thermal stratification, volumetric heat and momentum source model was chosen and C_{DDC} was obtained for oscillatory interface regime. To simulate thermal stratification exactly, C_{DDC} for all the regimes would be found and apply to downsized 2D SP and downsized torus SP. Finally, the unexpected pressure increase in Fukushima accident would be defined clearly.

CHAPTER 6 NON-DIMENSIONAL STUDY FOR THERMAL STRATIFICATION BY DCC

6.1 Background

It is highly difficult to investigate thermal stratification by DCC in the same scale with the SP of real light water reactors. It is not only inefficient in cost and time but also dangerous to generate the environment making SP work. It is not easy to carry out numerical simulation by two-phase code because of the complexity of two-phase and huge consuming time. Especially for the oscillating flow with high frequency, time step would have to be very short to make the calculation converged. To simulate with single-phase code, momentum should be carefully calculated to generate thermal stratification accurately. To calculate the momentum induced from oscillating condensation interface in long time, non-dimensional study should be preceded to decide the frequency and amplitude. To validate the single-phase code, the experimental results would be needed for validation. The experiment would be carried out in down-sized experimental devices and the experimental results could be valued by non-dimensional parameters.

6.2 Non-dimensional Numbers related to Thermal Stratification by DCC

There are several non-dimensional numbers which are well known in thermal hydraulics to investigate thermal stratification; Grashof number, Reynolds number and Richardson number as defined in equation (6-1), (6-2) and (6-3). Grashof number approximates the ratio of the buoyancy to viscous force, where L is the distance from the pipe tip to the bottom surface of SP. Reynolds number represents inertial force to viscous force. Richardson number demonstrates the ratio of the potential to kinetic energy that represents the ratio of the buoyancy to inertial force in thermal convection. It shows the importance of the natural convection to the forced convection.

$$Gr = g\left(\frac{\rho_{sat}-\rho_T}{\rho_{sat}}\right)\frac{L^3}{\nu^2} = \frac{g\beta\left(T_{sat}-T_T\right)L^3}{\nu^2} \tag{6-1}$$

$$\mathrm{Re} = \nu u L \tag{6-2}$$

$$Ri = \frac{Gr}{\mathrm{Re}^2} = \left(\frac{\rho_{sat} - \rho_T}{\rho_{sat}} \right) \frac{gL}{u^2} = \frac{g\beta \left(T_{sat} - T_T \right) L}{u^2} \tag{6-3}$$

If it is assumed that the subcooling, thermal expansion and viscosity is same, these equations could be changed as in the following equations. From Grashof number (*Gr*), Reynolds number (*Re*) and Richardson number (*Ri*), equation (6-4), (6-5) and (6-6) are induced. The subscript '2D' means the 2D downsized SP and 'F' means Fukushima unit#2 SP.

$$L_{2D}^3 = L_F^3 \tag{6-4}$$

$$u_{2D} L_{2D} = u_F L_F \tag{6-5}$$

$$\frac{L_{2D}}{u_{2D}^2} = \frac{L_F}{u_F^2} \tag{6-6}$$

Since the experimental devices are downsized, equation (6-4) cannot be valid. For reference, the L_t is 2.875m. To establish the equation (6-5), when the L_{2D} is shorter than L_F, u_{2D} should be larger than u_F. It seems to be difficult to make such high velocity in 2D downsized SP. Therefore, equation (6-6) would be valid compared to other ones. By this approximation, Richardson number is regarded as the most important non-dimensional parameter in this study.

6.3 Thermal Stratification Study by Richardson Number

6.3.1 DCC Richardson number

When *Ri* is much higher than 1, natural convection by buoyancy is getting stronger than the forced convection and thermal stratification may occur. On the other hand, if *Ri* is much lower than 1, forced convection by steam injection and condensation oscillation is getting stronger

than natural convection and SP water would be mixed. If the injected material is same phase with ambient fluid and there is no oscillation but stable injection flow, u could be the mean velocity of injected material. However, although the steam is injected as mean steam velocity, the steam condensed directly around the pipe tip and the inertial force is not transferred exactly to ambient fluid. And if the mean condensate velocity is calculated by the condensate volume flow rate and the area of cross section, the velocity is extremely low. Consequently, the velocity should be obtained from the steam bubble oscillation. Fig. 6.1 demonstrate the corresponding velocity at far-field. The velocity is generated from the oscillation of condensation interface. At near-field, DCC could make harsh oscillation with certain amplitude and frequency but at far-field, it determines the velocity and momentum by the oscillation amplitude and frequency. The corresponding velocity is calculated as $\sqrt{2}\delta f$. The momentum can be obtained as shown in the fig.6.1.

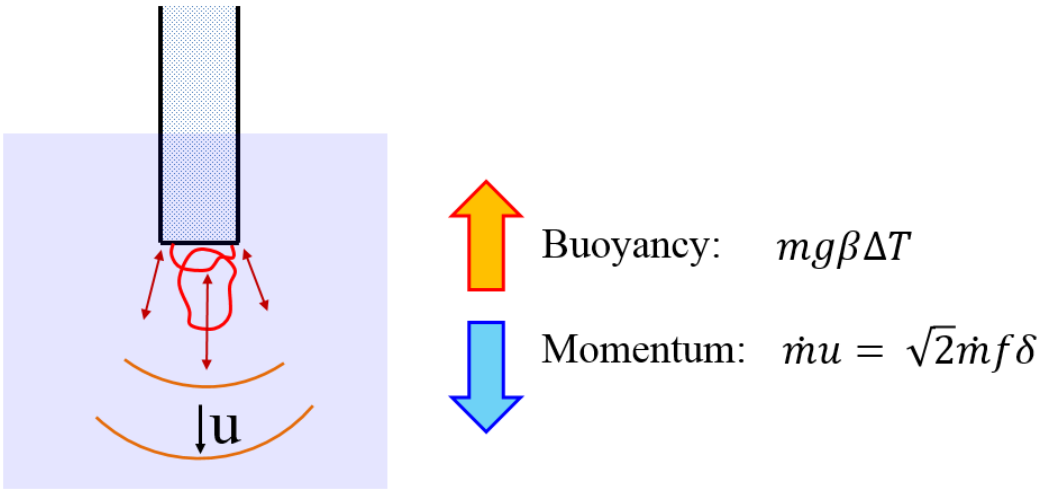

Fig.6.1 The schematic of corresponding velocity generation at far-field

As the corresponding velocity is used in equation (6-3), the equation is represented as equation (6-7). The amplitude and frequency are highly important parameter to determine DCC Richardson number.

$$Ri_{DCC} = \frac{g\beta\left(T_{sat} - T_T\right)L}{2f^2\delta^2} \tag{6-7}$$

6.3.2 Steam bubble Visualization for Ri_{DCC}

According to Chan et al. (1982), DCC regimes are categorized mainly into chugging regime, bubbling regime and jet regime [3]. In the regime map, chugging regime is represented when steam mass flux is less than 75 kg/m^{2}s. The inner diameter of steam injection pipe was 51mm. However, according to Petrovic et al. (2007), the threshold steam mass flux between chugging and bubbling increases with increasing steam injection pipe inner diameter. Aya et al. (1983) represented chugging regime until around 25 kg/m^{2}s when the diameter is 18 mm. Since the diameter of unit#2 of Fukushima nuclear power plant is 283.7mm, it is assumed that over all the period of Fukushima accident, the chugging regime was represented.

To investigate the relationship between thermal stratification and Richardson number, several experiments were carried out with the same experimental setup in the chapter 4. A high speed camera (PHOTRON, Fastcam APX RS) was used to obtain steam bubble motion images at the frame rate from 1,000 to 30,000 and at spatial resolution from 256 x 256 pixels to 512 x 512 pixels. More than 1000 images were obtained at each case. Temperature was measured by T-type thermocouples with the same arrangement of fig.3.3.

11 experimental cases were performed at different steam mass fluxes and each case was carried out for more than 1 hour. The specifications are shown in Table.7. Almost all the cases are started from around 30 kPa in absolute pressure except Case10 and 11. From the images, steam bubble frequency and amplitude were obtained to calculate Richardson number. Richardson numbers were obtained from 0.01 to 700. Steam injection inner diameter is 4.2mm and L is 0.15m.

Table.7 Experimental conditions for steam bubble visualization (D = 4.2mm)

	Pressure [kPa]	Subcooling range [K]	Mass flow rate [g/s]	Mass flux [kg/m^{2}s]	Heat input [W]
Case1	30.9 – 37.4	33.1 - 44.3	0.0424	3.06	98.8
Case2	31.5 – 38.8	30.5 - 43.1	0.0446	3.22	104
Case3	29.0 – 38.5	24.4 - 41.4	0.0594	4.29	138
Case4	31.6 – 45.4	23.4 - 42	0.0736	5.32	172
Case5	32.1 – 46.6	28.4 - 48.2	0.0747	5.39	174
Case6	34.6 – 60.1	21.4 - 39.3	0.119	8.57	276
Case7	33.5 – 71.9	25.0 - 51.8	0.143	10.3	332
Case8	32.4 – 83.2	17.9 - 51.4	0.194	14.0	452
Case9	31.2 – 88.5	14.7 - 44.5	0.263	19.0	614
Case10	13.7 – 31.7	17.2 - 32.8	0.0826	5.96	196
Case11	52.4 - 110	19.2 - 60.8	0.163	11.8	375

From these experiments, three regimes were demonstrated; (1) Oscillatory interface (2) External chug with detached bubble (ECDB), (3) External chug with encapsulated bubble (ECEB) and (4) Oscillatory bubble. Oscillatory interface and ECEB in low steam mass flux case were explained in chapter 4. ECDB and ECEB regimes in high steam mass flux case are shown in fig.6.2 and fig.6.3. If the steam mass flux is higher than 5 kg/m^{2}s, it is called as high steam mass flux case and if the steam mass flux is lower than 5 kg/m^{2}s, it is called as low steam mass flux case in this research. In high steam mass flux cases, oscillatory interface regime is not shown.

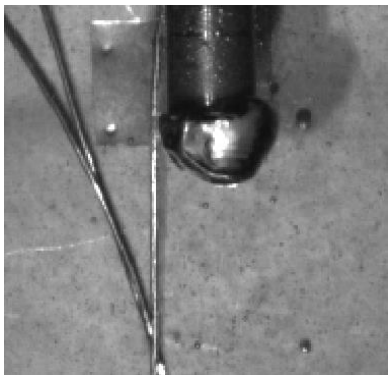

(a) Time = 0 × T

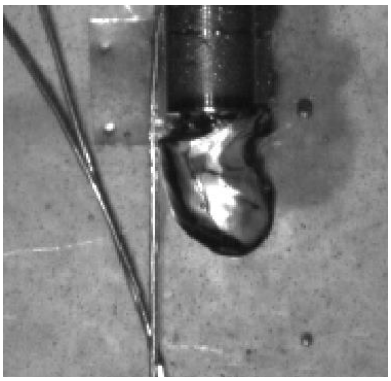

(b) Time = 0.27 × T

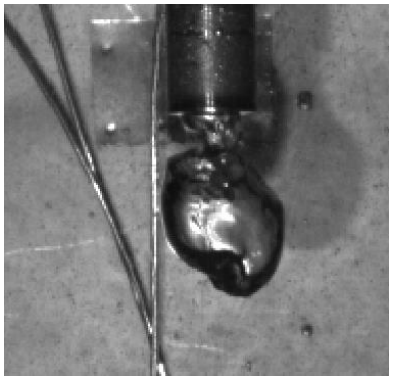

(c) Time = 0.49 × T

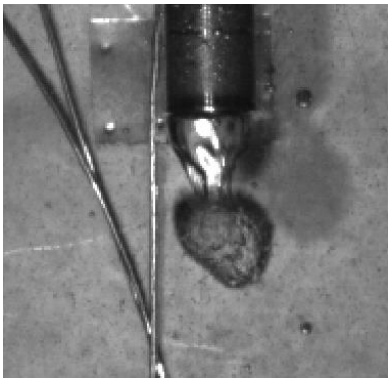

(d) Time = 0.54 × T

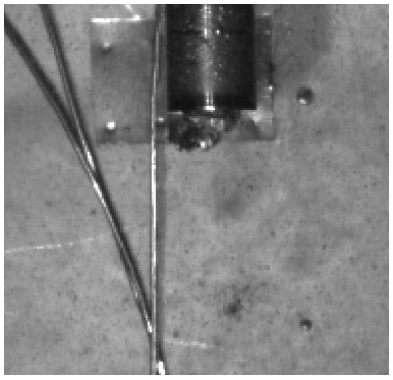

(e) Time = 0.62 × T

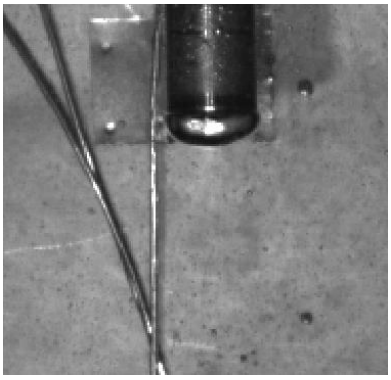

(f) Time = 0.86 × T

Fig.6.2 External chug with detached bubble at high mass flux

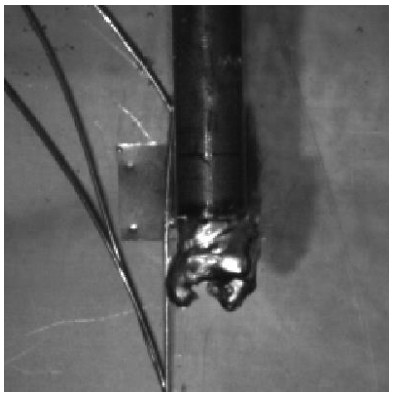

(a) Time = 0 × T

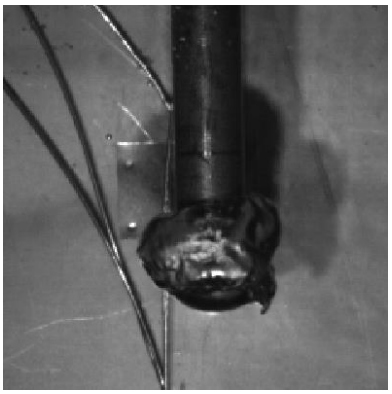

(b) Time = 0.26 × T

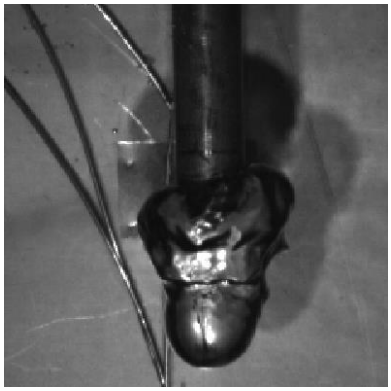

(c) Time = 0.49 × T

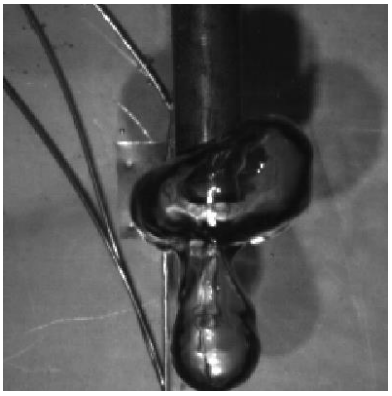

(d) Time = 0.70 × T

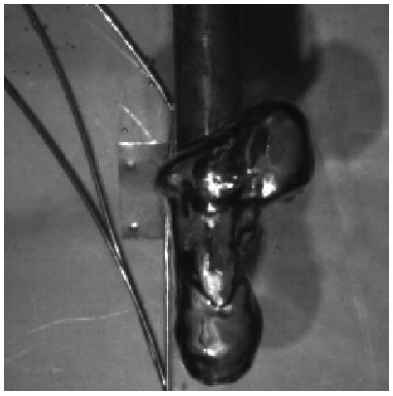

(e) Time = 0.85 × T

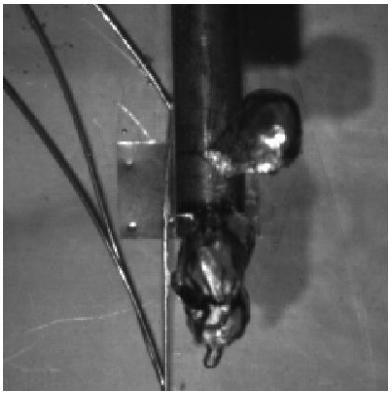

(f) Time = 0.95 × T

Fig.6.3 External chug with encapsulating bubble at high mass flux

As shown in fig.6.2, in ECDB, steam bubble is grown and around the pipe tip, steam bubble is disconnected and quick condensation happens. Frequency is higher than ECEB since condensation rate is higher than ECEB due to larger subcooling. Steam bubble is disappeared before the bubble goes up due to buoyancy. However, in ECEB, condensation is delayed and steam bubble grows more than ECDB. Steam bubble goes up due to buoyancy and encapsulate pipe tip. When the bubble is in the middle of encapsulating and growing, steam bubble is disconnected and quick condensation happens. Because of lower condensation late, frequency is lower than the one of ECDB.

From the visualization experiments, the frequency and the amplitude of steam bubble oscillation. The frequency was obtained from the dominant large motion with a cycle as explained in previous paragraph. Approximation of amplitude is quite complicated because the motion of condensation interface is highly unstable. Fig.6.4 shows how the amplitude was obtained from steam bubble visualization at each regime. For oscillatory interface regime and ECDB regime, the averaged distance between the highest and lowest interface in one cycle during experiment was regarded as the amplitude as represented in fig.6.4 (a) and (c). The lines represent the condensation interface. Solid line shows the interface when the steam bubble is minimum and dotted line shows the interface when it is maximum, where T is the time of one cycle. For ECEB regime, the difference of δ_1, the distance of highest and lowest interface, and δ_2, the size of smallest steam bubble as represented in fig.6.4 (b) and (d). The broken line at fig.6.4 (b) shows the growing steam bubble in the middle of the cycle.

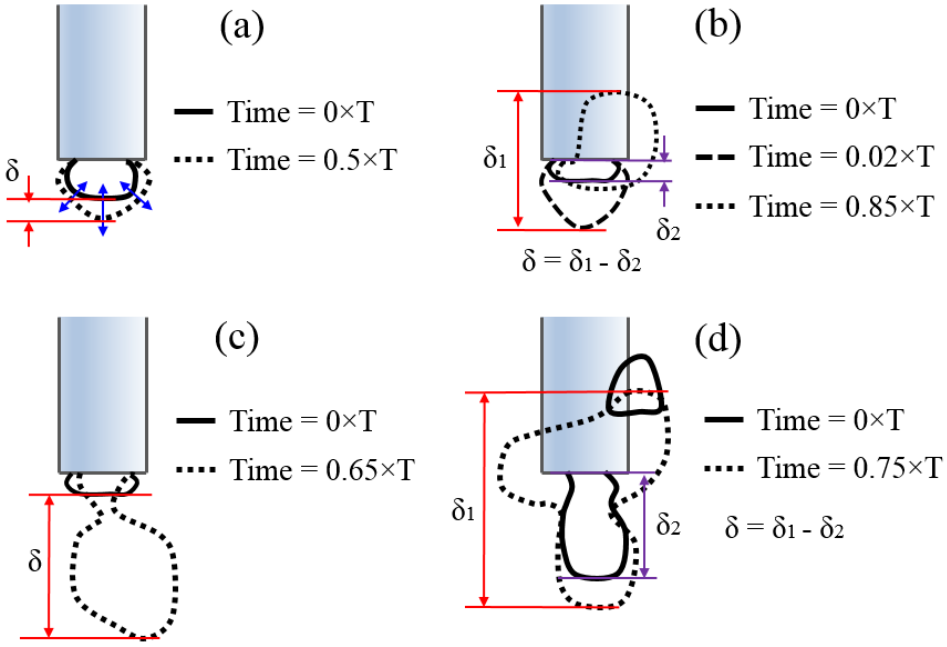

Fig.6.4 The amplitude measurement at each regime; (a) Oscillatory interface (b) ECEB at low mas flux (c) ECDB (d) ECEB at high mass flux

6.3.3 Investigation of Thermal Stratification Region

The Steam bubble visualization experiments represent that there are several regions related to thermal stratification and Ri_{DCC}. From Case1 to case 6, thermal stratification was shown from the beginning but from Case 7 to Case 11, thermal stratification occurred in the middle of experiment. Firstly, according to the experimental results, there are three regions regarding to thermal stratification related to Ri_{DCC}; (1) Unconditional Thermal Stratification, (2) Conditional Thermal Stratification and (3) No Thermal Stratification (Mixing). Following Table.8 demonstrates the criteria of thermal stratification depending on Ri_{DCC}.

Table.8 Criteria of thermal stratification

Region	Condition	j_m [kg/m2s]	DCC Regime
Unconditional Thermal Stratification	$2 < Ri_{DCC}$ High	j_m <5	Oscillatory Interface, Transitional area
		j_m >5	Any regime (L is large)
Conditional Thermal Stratification	$0.1 < Ri_{DCC} < 2$ Low	j_m <5	Transitional area, ECEB
		j_m >5	ECDB, ECEB, Oscillatory Bubble
No Thermal Stratification (Mixing)	$Ri_{DCC} < 0.1$ Extremely Low		

6.3.3.1 Unconditional Thermal Stratification region

Unconditional thermal stratification region shows when Richardson number is over than 2. In this case, the hot condensate after condensation directly flows upward near condensation interface and thermal stratification occurs. This region can be explained dividing two area according to steam mass flux; (a) Low steam mass flux case and (b) High steam mass flux case. The exact criteria slightly different depending on SP pressure but if the steam mass flux is lower than 5 kg/m^{2}s, it could be low steam mass flux case and if the steam mass flux is higher than 5 kg/m^{2}s, it could be high steam mass flux case for this research.

Low steam mass flux case in unconditional thermal stratification region shows oscillatory interface regime and transitional area of external chug with encapsulating bubble regime. When the regime changes from oscillatory interface to transitional area as subcooling decreases, the Ri_{DCC} decreases but still thermal stratification is shown. Case1 and 2 are included in this region.

Fig.6.5 shows the temperature profile and Ri_{DCC}, steam bubble frequency, amplitude according to time and subcooling of Case2. 1000 images were obtained by high speed camera every 5 minutes at the frame rate of 1000 to study frequency and amplitude.

From temperature profile, thermal stratification is shown clearly. Due to weak momentum, thermal stratification is shown even in mixing area. Richardson number is highly unstable because the frequency and amplitude are not stable. It ranges from 15 to 700 but it is still high enough to make thermal stratification. Subcooling decreases in the process of time since SP water temperature increases. As subcooling decreases, frequency suddenly decreases because the regime changes from oscillatory interface to transition area. Amplitude slightly increases as subcooling decreases but it is small compared to other regimes.

High steam mass flux case in unconditional thermal stratification region is found when L is large compared to generated momentum from DCC. In nuclear industry, it would be difficult to find this region. Thermal stratification could be shown in any regime in this region. This region should not be shown in SP because it means the SP is not efficient to suppress pressure.

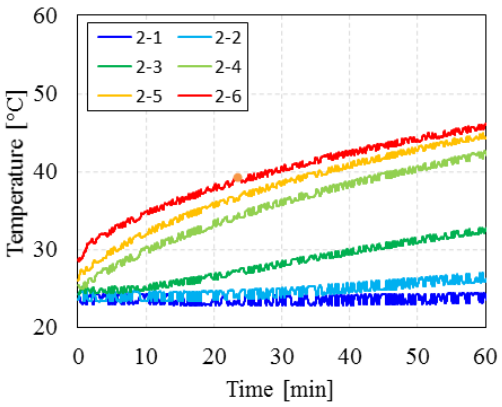

(a) Temperature profile

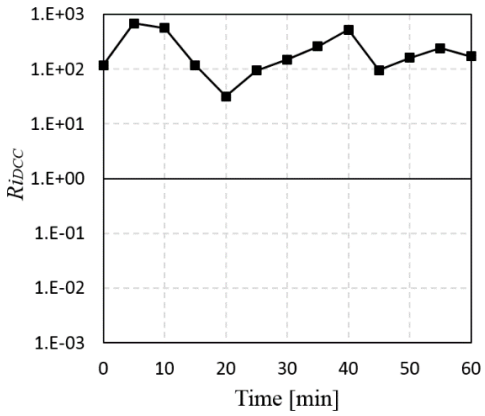

(b) Time – Ri_{DCC}

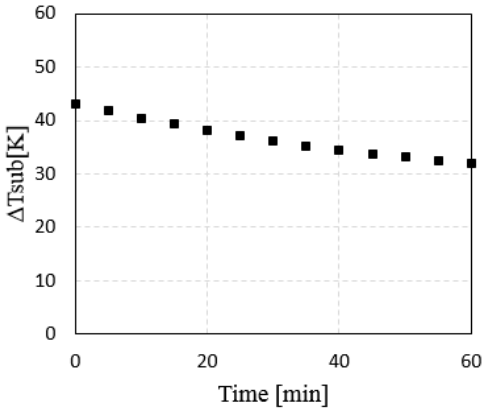

(c) Time – Subcooling

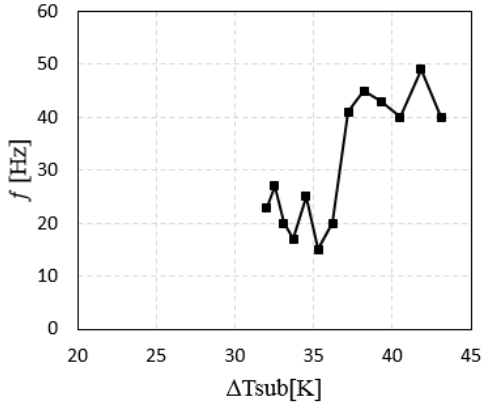

(d) Subcooling – f

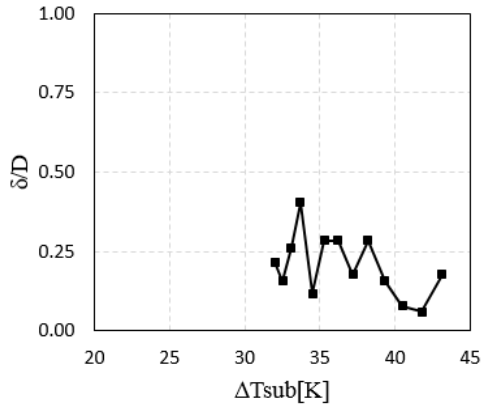

(e) Subcooling – δ/D

Fig.6.5 Case2

6.3.3.2 Conditional Thermal Stratification region

Conditional thermal stratification region is represented when Richardson number is between 0.1 and 2. In this case, buoyancy force and inertial force are similar and thermal stratification occurs conditionally depending on subcooling and pressure. This region can be explained dividing two area according to steam mass flux; (a) Low steam mass flux case and (b) High steam mass flux case.

Low steam mass flux case in conditional thermal stratification region shows transitional area and external chug with encapsulating bubble regime (ECEB). When the regime changes from transitional area to ECEB regime as subcooling decreases, the Ri_{DCC} decreases but still thermal stratification is shown. Case3, 4, 5 and 6 are included in this region. Case6 starts directly from ECEB regime since the steam mass flux is relatively high in Case6 compared to other cases. Fig.6.6 shows the temperature profile and Ri_{DCC}, steam bubble frequency, amplitude according to time and subcooling of Case4. 1500 images were obtained by high speed camera 21 times in 75 minutes at the frame rate of 3000 to study frequency and amplitude.

From temperature profile, thermal stratification is shown clearly. Due to relatively strong momentum, thermal stratification which is shown initially in mixing area disappeared when the regime changed to ECEB. However, thermal stratification is demonstrated over entire SP. Subcooling decreases in the process of time since SP water temperature increases. Richardson number rapidly decreases because the amplitude increases when the regime changes. It ranges from 4.0 to 0.7 but it still makes thermal stratification occur. Frequency decreases when regime changes but it is very difficult to exactly define the frequency in transition area since the bubble oscillates highly randomly.

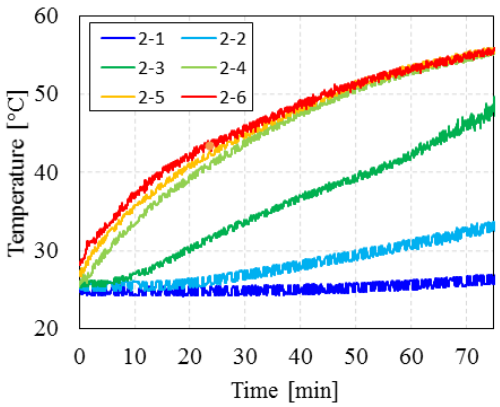

(a) Temperature profile

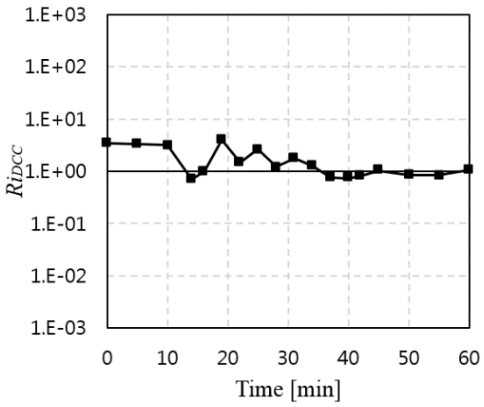

(b) Time – Ri_{DCC}

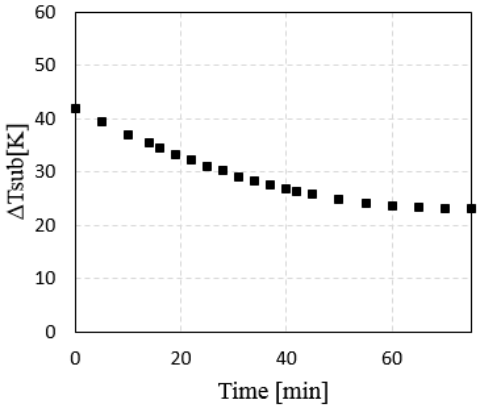

(c) Time – Subcooling

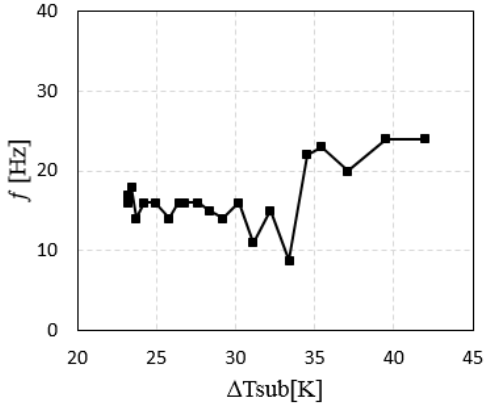

(d) Subcooling – *f*

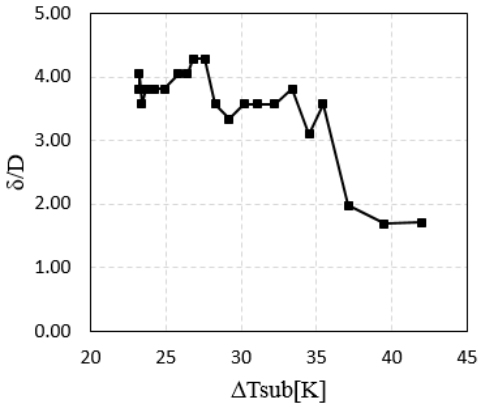

(e) Subcooling – δ/D

Fig.6.6 Case4

High steam mass flux case in conditional thermal stratification region is shown in internal chugging, external chug with detached bubble regime (ECDB), external chug with encapsulating bubble regime (ECEB) and oscillatory bubble regime. Depending on steam mass flux and subcooling, internal chugging is not represented. In internal chugging regime, ECBD regime and oscillatory bubble regime, it is more difficult that thermal stratification occur than in ECEB regime since those momentum are relatively larger than the one of ECEB regime. Case7, 8, 10 and 11 are included in this region. Fig.6.7 shows the temperature profile and Ri_{DCC}, steam bubble frequency, amplitude according to time and subcooling of Case10. 1000 images were obtained by high speed camera every 5 minutes at the frame rate from 1500 to 10000 to study frequency and amplitude.

From temperature profile, thermal stratification is shown in the middle. Due to relatively strong momentum, thermal stratification is not shown initially over entire SP. However, thermal stratification is demonstrated when ECEB regime starts. Subcooling decreases in the process of time since SP water temperature increases and the regime changes in the order of internal chugging, ECDB, ECEB and oscillatory bubble. Richardson numbers in ECEB regime are relatively higher than the ones in other regimes. It ranges from 0.2 to 1.1. As subcooling decreases and regimes change, the frequency decreases and amplitude increases.

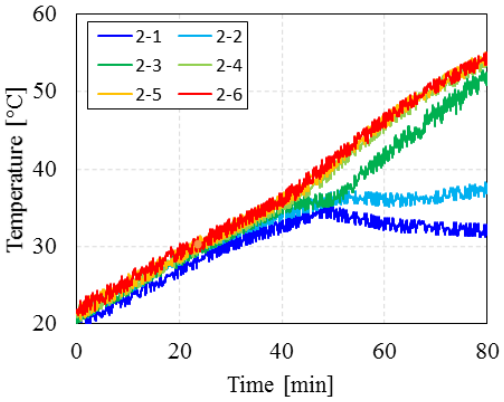

(a) Temperature profile

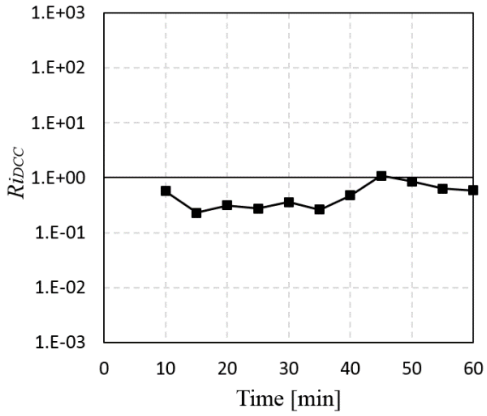

(b) Time – Ri_{DCC}

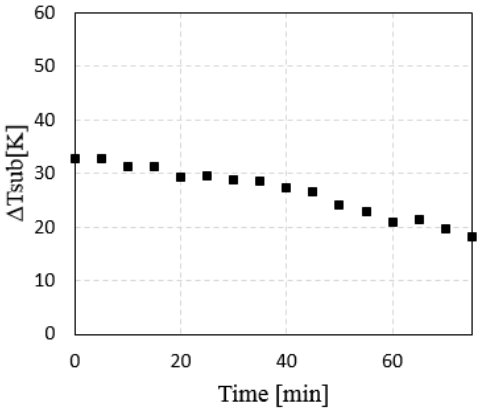

(c) Time – Subcooling

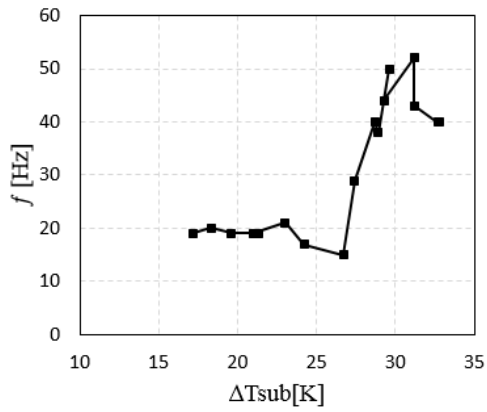

(d) Subcooling – f

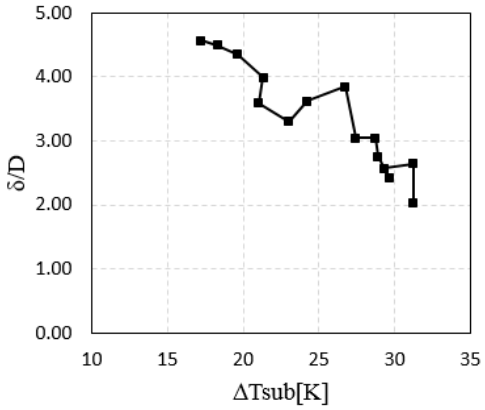

(e) Subcooling – δ/D

Fig.6.7 Case10

6.3.3.3 Mixing region

Mixing region is shown when Richardson number is less than 0.1. In this case, the momentum induced from DCC is much larger than buoyancy and L is short enough for entire SP to be mixed. If Richardson number is less than 0.1 over entire process, thermal stratification is difficult to be occurred. Case9 is in this region. Fig.6.8 shows the temperature profile and Ri_{DCC}, steam bubble frequency, amplitude according to time and subcooling of Case9. 1000 images were obtained by high speed camera every 5 minutes at the frame rate from 10000 to 15000 to study frequency and amplitude.

From temperature profile, thermal stratification is not shown except when ECEB is represented. Ri_{DCC} ranges from 0.02 to 0.2 This case shows conditional thermal stratification region and mixing region together. Subcooling decreases in the process of time since SP water temperature increases. Initially internal chugging is shown and it changes to other regimes. As subcooling decreases, frequency decreases because the regime changes from internal chugging to ECDB, ECEB and amplitude gradually increases.

The frequency in internal regime is extremely high compared to other regimes. Compared to other cases, it is assumed that until 35 minutes, internal chugging is shown in Case9 since the frequency of ECDB is between 40 and 50 in other cases. In Case9, the maximum frequency is over than 200 and it is estimated that the frequency would be higher when subcooling is larger than 45. The frequency in internal chugging increases with subcooling almost linearly.

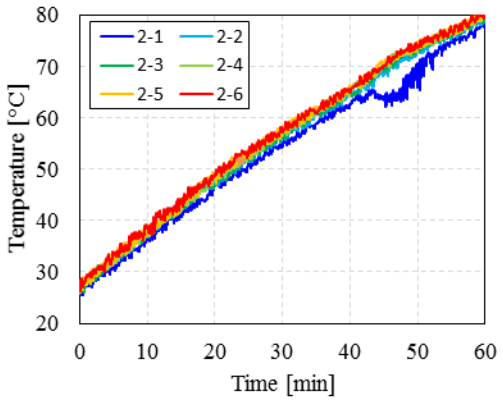

(a) Temperature profile

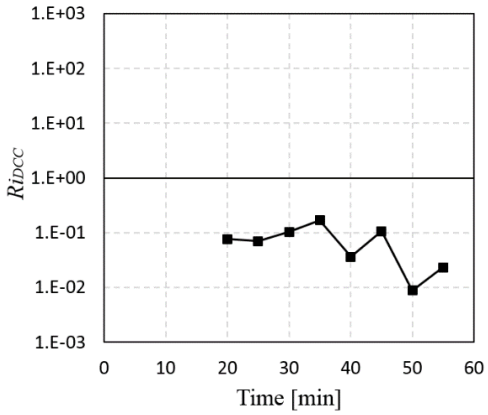

(b) Time – Ri_{DCC}

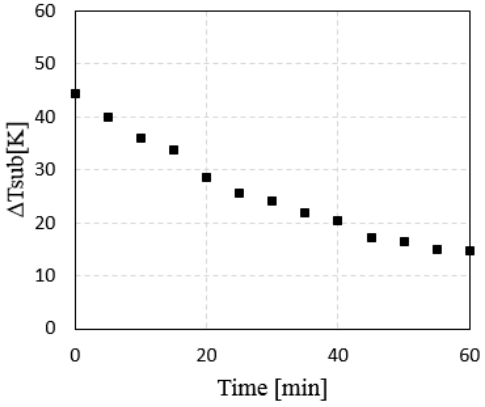

(c) Time – Subcooling

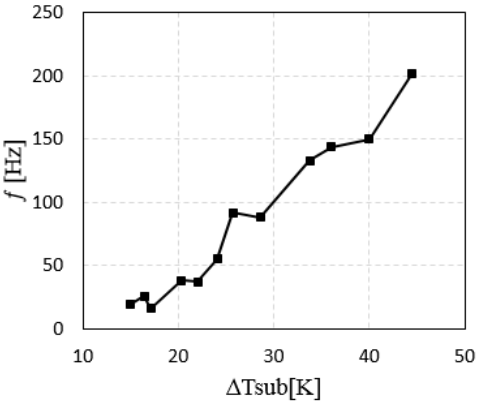

(d) Subcooling – f

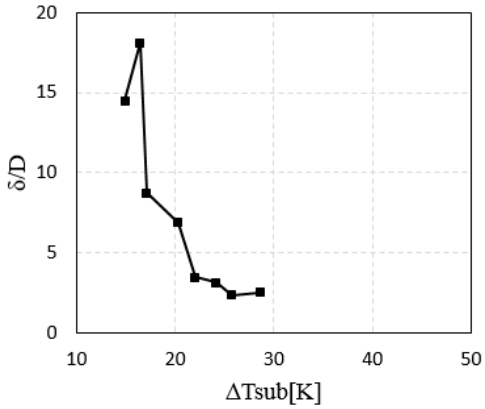

(e) Subcooling – δ/D

Fig.6.8 Case9

6.4 Discussion and Summary

If the inertial force in the direction of gravity from heat source is not stronger than buoyancy force induced by the water density difference, only the water over the position of the heat source is heated by natural convection. Especially, the top area of the liquid has much higher temperature than other area. In case of low frequency and amplitude from condensation interface, thermal stratification may occur due to the weak momentum of condensate which cannot generate large advection in SP in certain conditions.

To study the criteria of thermal stratification by DCC, non-dimensional study was done using Richardson number for DCC (Ri_{DCC}). Considering the characteristics of the oscillating condensation interface, the corresponding velocity at far-field was used as velocity term and the distance from pipe tip to pool bottom was used as characteristic length. Ri_{DCC} was investigated from the steam bubble visualization study and the criteria for thermal stratification by DCC was suggested. It is shown that although ECEB has larger momentum compared to oscillatory interface at low mass flux case, ECEB has relatively lower momentum compared to other regimes at high mass flux case. Fig.6.9 represents Ri_{DCC} and thermal stratification region. The clear boundaries are demonstrated by three regions.

At high mass flux case, as subcooling decreases, the bubble frequency decreases since the regimes changes from internal chugging to ECDB and ECEB. However, the bubble amplitude increases especially from ECEB because the condensation delays as condensation rate decreases. As the bubble amplitude increases more and more, the regime changes from ECEB to oscillatory bubble. In this process, the corresponding velocity is determined by the bubble frequency and amplitude, and the occurrence of thermal stratification is decided by a criteria.

To observe thermal stratification in SP, firstly Ri_{DCC} should be high. Definite thermal stratification takes place when it is over than 2. It can also take place when the momentum generated from condensation interface is low or L is large. When Ri_{DCC} is between 0.1 and 2.0, DCC should be in ECEB regime to get thermal stratification. ECDB regime has larger momentum than ECEB regime and thermal stratification happens when the regime changes from ECDB to ECEB. If Ri_{DCC} is lower than 0.1, SP would be fully mixed and it would be

difficult to get stratification. It is useful to estimate the occurrence of thermal stratification by Ri_{DCC}. Jet regime was not studied in this research but thermal stratification would be affected only by L since jet regime has much more momentum than other regimes.

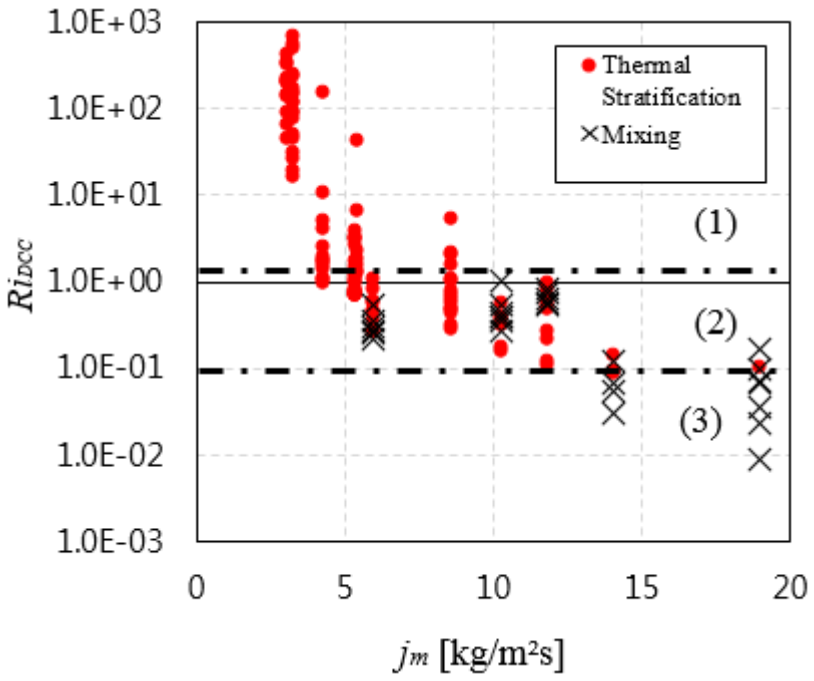

Fig.6.9 Ri_{DCC} and thermal stratification region

CHAPTER 7 CONCLUSION

To understand unexpected pressure increase of SP in Fukushima accident and give useful information to LWRs designers for nuclear safety, downsized 2D SP was designed and experiments were carried out. This research is carried out to understand thermal stratification in SP experimentally and analytically and to predict the thermal stratification by single phase CFD code. Because of complicated phenomena depending on DCC regimes and the difficulties of accurate momentum calculation from two phase simulation, single phase model is selected and additional heat and momentum models are investigated.

At oscillatory interface regime, temperature distribution and velocity field around steam injection pipe were obtained. To measure momentum from condensation interface, the oscillating frequency and the amplitude were investigated and the regime between oscillatory interface and external chugging was found. To simulate thermal stratification, volumetric heat and momentum source model was chosen and C_{DCC} was obtained from validation of the code with experiments. This code was validated with downsized torus experiment.

To investigate thermal stratification criteria by non-dimensional parameter, Richardson number for DCC was calculated with steam bubble visualization data. There are three regions regarding to thermal stratification; (1) unconditional thermal stratification region, (2) conditional thermal stratification region and (3) no thermal stratification region. In conditional thermal stratification region, DCC regime is important to predict the feasibility of thermal stratification and the regime depends on steam mass flux, subcooling and steam injection pipe inner diameter.

REFERENCE

[1] US.NRC, www.nrc.gov/reactors/generic-bwr.pdf

[2] TEPCO, Fukushima Nuclear Accident Analysis Report, (2012)

[3] C. K. Chan and C. K. B. Lee, A regime map for direct contact condensation, *Int. J. Multipahse Flow*, 8(1) (1982),11-20

[4] I. Aya and H. Nariai, Boundries between regimes of pressure oscillation induced by steam condensation in pressure suppression containment, *Nucl. Eng. Des.*, 131 (1991) 17-24

[5] K. S. Liang and P. Griffith, Experimental and analytical study of direct contact condensation of steam in water, *Nucl. Eng. Des.*, 147 (1994) 425-435

[6] A. Petrovic de With, R. K. Calay and G.de With, Three-dimensional condensation regime diagram for direct contact condensation of steam injected into water, *Int. J. Heat Mass Transfer*, 50 (2007), 1762-1770

[7] P. J. Kerney, G. M. Faeth and D. R. Orson, Penetration characteristics of a submerged steam jet, *AIChE J.*, 18(3) (1972) 548-553

[8] I. Aya, H. Nariai and M. Kobayashi, Pressure and fluid oscillations in vent system due to steam condensation, (I) Experimental results and analysis model for chugging, *J. Nucl. Sci. Technol.*, 17(7) (1980) 499-515

[9] I. Aya, M. Kobayashi and H. Nariai, Pressure and fluid oscillations in vent system due to steam condensation, (II) High-frequency component of pressure oscillations in vent tubes under at chugging and condensation oscillation, *J. Nucl. Sci. Technol.*, 20(3) (1983) 213-227

[10] H. Nariai and I. Aya, Fluid and pressure oscillations occurring at direct contact condensation of steam flow with cold water, *Nucl. Eng. Des,*. 95 (1986) 35-45

[11] B. L. Smith and A. Glezer, The formation and evolution of synthetic jets, *Phys. Fluids*, 10(9) (1998) 2281-2297

[12] M. H. Chun, Y. S. Kim and J. W. Park, An investigation of direct condensation of steam jet in subcooled water, *Int. Comm. Heat Mass Transfer*, 23(7) (1996) 947-958

[13] A. Petrovic, Analytical study of flow regimes for direct contact condensation based on parametrical investigation, *J. Pressure Vessel Technol*. 127(1) (2005) 20-25

[14] A. de With, Steam plume length diagram for direct contact condensation of steam injected into water, *Int. J. Heat Fluid Flow*, 30 (2009) 971-982

[15] N. Clerx and C. W. M. van der Geld, Experimental and analytical study of intermittency in direct contact condensation of steam in a cross-flow of water, *ECI International*

Conference on Boiling Heat Transfer, Brazil, 3-7 May (2009)

[16] G. Class, S. Raff and R. Meyder, The mechanism of violent condensation shocks, *Int. J. Multiphase Flow*, 13(1) (1987) 33-46

[17] S. S. Gulawani, S. K. Dahikar, C. S. Mathpati, J. B. Joshi, M .S. Shah, C. S. RamaPrasad, D. S. Shukla, Anaysis of flow pattern and heat transfer in direct contact condensation, *Chem. Eng. Sci.* 64 (2009) 1719-1738

[18] I. Aya and H. Nariai, Evaluatoin of heat-transfer coefficient at direct-contact condensation of cold water and steam, *Nucl. Eng. Des.* 131 (1991) 17-24

[19] A. Murata, E. Hihara and T. Saito, Prediction of heat transfer by direct contact condensation at a steam-subcooled water interface, Int. J. Heat Mass Transfer., 35(1) (1992) 101-109

[20] M. Murase, Y. Kataoka, T. Fujii, Evaporation and condensation heat transfer with a noncondensable gas present, *Nucl. Eng. Des.* 141 (1993) 135-143

[21] T. Fujii, Y. Kataoka and M. Murase, Evaporation and condensation heat transfer in a suppression chamber of the water wall type passive containment cooling system, *J. Nucl. Sci. Technol.*, 20(5) (1996) 374-380

[22] S. G. Bankoff, Some condensation studies pertinent to LWR safety, *Int. J. Multipahse Flow*, 6 (1980),51-67

[23] R. E. Gamble, T. T. Nguyen, B. S. Shiralkar, P. F. Peterson, R. Greif and H. Tabata, Pressure suppression pool mixing in passive advanced BWR plants, *Nucl. Eng. Des.,* 204 (2001), 321-336

[24] E. Krepper, E. F. Hicken and H. Jaegers, Investigation of natural convection in large pools, *Int. J. Heat Fluid Flow*, 23 (2002) 359-365

[25] L. Cheng, K. S.Woo, M. Ishii and J. Lim, Suppression pool mixing and condensation tests in PUMA facility, *The 14th International Conference on Nuclear Engineering*, USA, 17-20 Jul. (2006)

[26] Y. J. Choo and C. Song, PIV measurements of turbulent jet and pool mixing produced by a steam jet discharge in a subcooled water pool, *Nucl. Eng. Des.*, 240 (2010), 2215-2224

[27] T. L. Norman and S. T. Revankar, Jet-plume condensation of steam-air mixtures in subcooled water, Part 1: Experiements, *Nucl. Eng. Des.*, 240 (2010) 524-532

[28] T. L. Norman and S. T. Revankar, Jet-plume condensation of steam-air mixtures in

subcooled water, Part 2: Code model, *Nucl. Eng. Des.,* 240 (2010) 533-537
[29] H. S. Kang and C. H. Song, CFD analysis for thermal mixing in a subcooled water tank under a high steam mass flux discharge condition, Nucl. Eng. Des., 238 (2008) 492-501
[30] Y. Moon, H. Lee and G. Park, CFD simulation of steam jet-induced thermal mixing in subcooled water pool, Nucl. Eng. Des., 239 (2009) 2849-2863
[31] H. S. Kang and C. H. Song, CFD analysis of a turbulent jet behavior induced by a steam jet discharge through a single hole in a subcooled water tank, Nucl. Eng. Des., 2340 (2010) 2160-2168
[32] H. Purhonen, M. Puustinen, J. Laine, A. Rasanen, R. K. Rajamaki, J. Vihavainen, Steam blowdown experiments with the condensation pool test rig, Nuclear Energy for New Europe 2005, Slovenia, 5-8 Sep. (2005)
[33] V. Tanskanen, D. Lakehal and M. Puustinen, Validation of direct contact condensation CFD models against condensation pool experiment, XCFD4NRS OECD conf., Grenoble, 12-15 Sep. (2008)
[34] H. Li and P. Kudinov: Effective approaches to simulation of thermal stratification and mixing in a pressure suppression pool, CFD4NRS-3 Workshop, USA, 14-16 Sep. (2010)
[35] H. Zhao, L. Zou and H. Zhang, An effective modeling method for thermal stratification simulation in a BWR suppression pool, NUTHOS-9, Taiwan, 9-13 Sep. (2012)
[36] J. Laine and M. Puustinen, Thermal stratification experiments with the condensation pool test rig, NKS report, Jan. (2006)
[37] H. Li, P. Kudinov and W. Vilanueva, Development and validation of effective models for simulation of stratification and mixing phenomena in a pool of water, NKS report, Jun. (2011)
[38] H. Li, W. Villanueva and P. Kudinov, Effective momentum and heat flux models for simulation of stratification and mixing in a large pool of water, NKS report, Jun. (2012)
[39] H. Lee and M. Kim, The effect of non-condensable gas on direct contact condensation of steam/air mixture*, J. Korean Nucl. Soc,* 33(6), (2001) 585-595
[40] R. Quintana, Vent clearing analysis of a Mark III pressure suppression containment, *Nucl. Eng. Des.*, 55 (1979) 395-401
[41] ANSYS Inc., ANSYS CFX 14.0 - Solver Theory Guide, (2011)